Design and optimization of an innovative bio-sourced building envelop component : numerical and experimental studies

Yaping Zhou

Thesis National Number : 2022ENTP0006

A THESIS OF ENTPE
Member of the Université de Lyon

Doctoral school N° 162
MEGA (Mécanique, Energétique, Génie Civil, Acoustique)

To obtain the graduation of
PhD in Génie Civil

Defended on December 13 2022 by:
Yaping Zhou

Design and optimization of an innovative bio-sourced building envelop component: numerical and experimental studies

---

In front of the following examination committee:

WANG, LiangZhu (Leon)/Professor/Université Concordia	Commitee chair
ZHAI, Zhiqiang (John)/Professor/Université du Colorado à Boulder	Reviewer
BENHAMOU, Brahim/Professor/Université Qadi Ayyad Marrakech	Reviewer
GUERNOUTI, Sihem/Chargée de Recherche/CEREMA	Examiner
TRABELSI, Abdelkrim / Maitre de conferences / Université Lyon 1	Co-supervisor
El MANKIBI, Mohamed / Directeur de Recherches / ENTPE-LTDS	Supervisor

N° d'ordre NNT : 2022ENTP0006

THÈSE DE DOCTORAT DE L'ENTPE
Membre de l'Université de Lyon

École Doctorale N°62
MEGA (Mécanique, Énergétique, Génie Civil, Acoustique)

Spécialité/ discipline de doctorat : **Génie Civil**

Soutenue publiquement le 13/12/2022, par :
Yaping Zhou

Conception et optimisation d'un composant innovant d'enveloppe de bâtiment biosourcé : études numériques et expérimentales

---

Devant le jury composé de :

WANG, LiangZhu (Leon)/Professeur/Université Concordia	Président
ZHAI, Zhiqiang (John)/Professeur/Université du Colorado à Boulder	Rapporteur
BENHAMOU, Brahim/Professeur/Université Qadi Ayyad Marrakech	Rapporteur
GUERNOUTI, Sihem/Chargée de Recherche/CEREMA	Examinatrice
TRABELSI, Abdelkrim/Maitre de conférences/Université Lyon 1	Co-directeur de thèse
El MANKIBI, Mohamed/Directeur de Recherches/ENTPE-LTDS	Directeur de thèse

Contents

Abstract

The treatment of rice straw is a largely disputed problem. Conversion rice straw waste to bio-sourced insulation products for buildings provide a cost-effective and eco-friendly approach. Rice straw insulation panels available in market have good hygrothermal properties. However, they use non-renewable and non-degradable binders, such as polyester fibres. This work focus on the develop fully bio-sourced insulation materials from rice straw waste.

First, the innovative rice straw insulation composites from rice straw and natural binders including sodium alginate and chitosan are developed and characterized at the material scale. A procedure is proposed by employing crosslinking method for prevent the water-soluble issue of using sodium alginate as the binder. The influence of fibre size, binder ratio and binder type on the thermal conductivity, moisture sorption capacity, water vapor permeability and water absorption are studied. The mould growth of the composites is also investigated. The results showed that the developed composites can be considered as insulators. Furthermore, the fibre size, binder ratio and binder ratio showed the varied impact on the properties of the composites.

In order to further evaluate the hygrothermal behaviour, a singer layer of rice straw alginate panel is studied at wall scale subjecting to isothermal, non-isothermal and dynamic boundary conditions. Based on the experimental data, a coupled heat and moisture (CHM) model is used to predict the hygrothermal behaviour in the wall. The CHM model is compared to a transient heat transfer (TH) model to demonstrate the coupling effect of heat transfer and moisture transfer. Furthermore, an inverse method is applied to estimate the liquid water permeability of the material. Results indicated that when the CHM model take the liquid water transfer into account based on the estimated property, the prediction accuracy can be improved.

Key words: building insulation; rice straw; sodium alginate; chitosan; hygric properties; coupled heat and moisture transfer model; inverse estimation

Résumé

Le traitement de la paille de riz est un problème largement contesté. La conversion des déchets de paille de riz en produits d'isolation biosourcés pour les bâtiments constitue une approche rentable et écologique. Les panneaux isolants en paille de riz disponibles sur le marché ont de bonnes propriétés hygrothermiques. Cependant, ils utilisent des liants non renouvelables et non dégradables, comme les fibres thermofusibles. Ce travail se concentre sur le développement de matériaux d'isolation entièrement bio-sourcés à partir de déchets de paille de riz.

Tout d'abord, les composites innovants d'isolation à base de paille de riz et de liants naturels, dont l'alginate de sodium et le chitosan, sont développés et caractérisés à l'échelle du matériau. Une procédure est proposée en utilisant la méthode de réticulation pour résoudre le problème de solubilité dans l'eau de l'utilisation de l'alginate de sodium comme liant. L'influence de la taille des fibres, du ratio de liant et du type de liant sur la conductivité thermique, la capacité de sorption de l'humidité, la perméabilité à la vapeur d'eau et l'absorption d'eau est étudiée. La croissance du moule des composites est également étudiée. Les résultats montrent que les composites développés peuvent être considérés comme des isolants. De plus, la taille des fibres, le taux de liant et le ratio de liant ont un impact variable sur les propriétés des composites.

Afin d'évaluer plus avant le comportement hygrothermique, une couche de singer d'un panneau d'alginate de paille de riz est étudiée à l'échelle du mur en la soumettant à des conditions limites isothermes, non isothermes et dynamiques. Sur la base des données expérimentales, un modèle couplé chaleur et humidité (CHM) est utilisé pour prédire le comportement hypothermique dans le mur. Le modèle CHM est comparé à un modèle de transfert thermique transitoire (TH) pour démontrer l'effet de couplage du transfert de chaleur et du transfert d'humidité. En outre, une méthode inverse est appliquée pour estimer la perméabilité à l'eau liquide du matériau. Les résultats indiquent que lorsque le modèle CHM prend en compte le transfert d'eau liquide sur la base de la propriété estimée, la prédiction peut être améliorée.

Mots clés : isolation des bâtiments; paille de riz; alginate de sodium; chitosan; propriétés hygiéniques; modèle couplé de transfert de chaleur et d'humidité; estimation inverse

Acknowledgements

I would like to express my deeply appreciate to my supervisors El Mankibi Mohamed and Trabelsi Abdelkrim for their support and encouragement to conduct scientific research. My supervisors give me the freedom to explore the research activities of interest. They are always very kind to me and concerned about my life.

I would like to thank the Région Auvergne-Rhône-Alpes and the Chinese Scholarship Council (CSC) to provide the financial support for the study and research in France.

I would like to express my gratitude to Francette PIGNARD, Paul Martin de BEAUCE and Luc Delattre for their help and assistance.

I am also grateful to Zhai Zhiqiang (John) and Benhamou Brahim for agreeing to review and evaluate my work. I also express my gratitude to Wang Liangzhu (Leon) and Tasca-Guernouti Shihem for taking part in my thesis jury.

I would like to express my gratitude to the FBT isolation to provide all the materials for manufacturing the rice straw insulators in my research. I would like to convey my thanks to Xavier Durand for manufacturing the rice straw insulation wall installed at the CETHIL-INSA LYON. I am also very grateful to Haehnlen Jonathan, Sallet Frederic and Cointet Stephane for their support on the sample cutting and the hygrothermal testing of the insulation materials.

I would like express my thanks to my friend Huang Yujian to accompany me from

graduate to PhD and experience almost everything together. I would like to thank Gong Xin and Ouyang Tianrui for their help to translate French for me. I would like to express my gratitude to my colleagues at the LTDS research group, Bahrar Myriam, Coillot Mike, Laaroussi Yousra for all your help in these years. I want to thank my family for their love. Finally, I want to express my thanks to all the people who helped, inspired and supported me in the past three years.

Yaping Zhou

Lyon, October 2022

Symbol and abbreviations

Symbols

A	Exposed surface area of the composite sample
b_m	Moisture effusivity
d	Thickness
d_a	Damping coefficient
D_w	Moisture diffusivity
e_a	Mass coefficient
f	Source term
G	Water vapor transmission flow
g_v	Water vapor transmission rate
g_l	Liquid water transmission rate
gm	Moisture flux
h	Heat transfer coefficient
K_l	Liquid water permeability
MBV	Moisture buffering value
MBV_{idea}	Theoretical moisture buffering value
Pc	Capillary pressure
Pv	Partial water vapor pressure
$Psat$	Saturated water vapor pressure
q	Heat flux at the boundaries of the wall
Rv	Water vapor gas constant
t	Time

T	Temperature
u	Moisture content by mass
w	Moisture content
W_d	Mass of the dried sample
W_i	Mass of the sample after immersion
W_p	Water absorption
α	Thermal diffusivity
β	Thermal effusivity
βi	Water vapor transfer coefficient at the interior surface
βe	Water vapor transfer coefficient at the Exterior surface
λ	Thermal conductivity
ρ	Density
ρ_d	Dry density
C_p	Mass specific heat capacity
Cp,l	Mass specific heat capacity of water
ξ	Moisture sorption capacity
w	Moisture content
δ_a	Water vapor permeability of air
δ_p	Water vapor permeability
μ	Water vapor diffusion resistance factor
Δm	Adsorbed or desorbed mass
Δp_v	Water vapor pressure difference
Δw	Change of moisture content
φ	Relative humidity
Γ	Conservative flux

Abbreviations

A	Alginate-based composites
C	Chitosan-based composites
CHM	Coupled heat and moisture transfer
CHMWL	CHM model considering liquid water transfer
CHMWL+Fmincon	CHMWL model with Kl searched by Fmincon
CHMWL+PSO	CHMWL model with Kl searched by Particle Swarm Optimizer
CHMWL+GA	CHMWL model with Kl searched by Genetic Algorithm
GA	Genetic Algorithm
MAE	Mean absolute error
PSO	Particle Swarm Optimizer
RS	Rice straw
RMSE	Root mean squared error
TH	Transient heat transfer

List of figures

List of tables

1. General introduction

1.1. Background

According to the BP Statistical Review of World Energy, France had an electricity production of 551-577 TWh/year from 2010 to 2021 [1]. Figure 1.1 shows the share of electricity production by source from 2010 to 2021 in which low carbon energies including nuclear and renewable technologies contribute to the majority of the electricity demand in France. In terms of energy consumption in France, the residential sector consumes almost one-third in total final energy consumption.

France legalized its Energy Transition for Green Growth in 2015, promoting the reduction of waste, energy consumption and greenhouse gases emissions (GHGs). Energy consumption is expected to be reduced by 50% between 2012 and 2050. GHGs is expected to be scaled-down by 75% in 2050 in comparison of 1990. In France, approximately 45% of the total energy consumption and almost 28% of GHGs are in

charge by buildings. Therefore, in order to reduce energy consumed in operation while guarantee the occupants' comfort, the thermal performance of building envelop should be improved. Applying insulation layer to building envelop is determined as an effective solution for energy saving in operation.

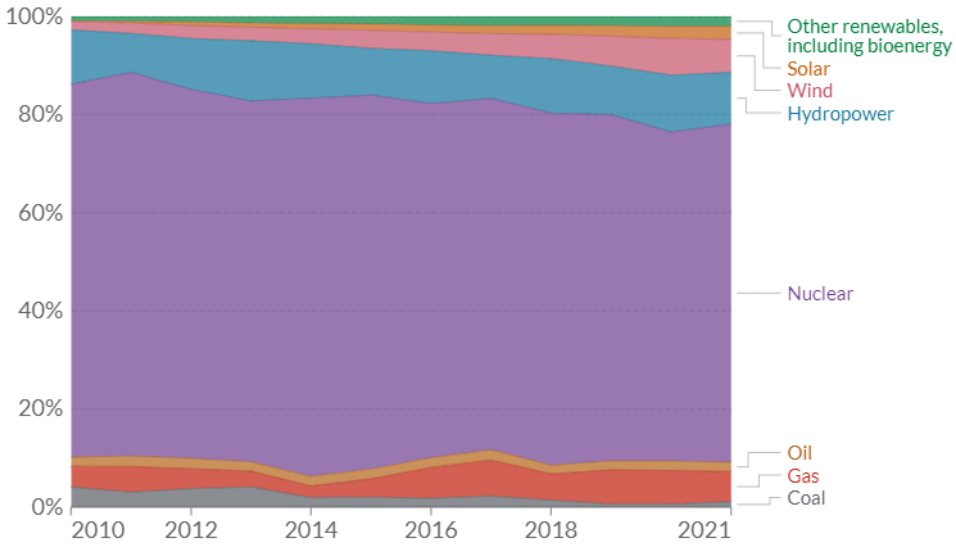

Figure 1.1 Electricity production by source in France from 2010 to 2021 (BP Statistical Review of World Energy, 2022) [1]

Thermal insulation materials aim to reduce the heat flow transfer by conduction. The most significant factor that characterizes the effectiveness of a thermal insulation material is its thermal conductivity. The lower thermal conductivity of a material, the increased effectiveness it is as a thermal insulation, and consequently a thinner layer is required to provide an equal interior temperature. The thermal insulation materials available in market can be classified into four categories as shown in Figure 1.2. Nowadays, the mainstream thermal insulation products are manufactured from conventional inorganic materials, such as glass wool and stone wool due to their predominate thermal properties [2]. However, their production consumes a large amount of non-renewable resource and causes greenhouse gas emission, which

ultimately lead to climate change and environment pollution. Also, they are generally not subjected to biological degradation. Therefore, a topic of major interest in building construction sector is to replace conventional insulation materials with natural insulation materials, which exert low environment impact during their entire life cycle. It has been estimated that utilizing cellulose fibre insulation to substitute the common insulation materials (i.e., rock wool and glass wool) in buildings allows to reduce 39% of fossil fuels and 6-8% of CO_2 emissions [3].

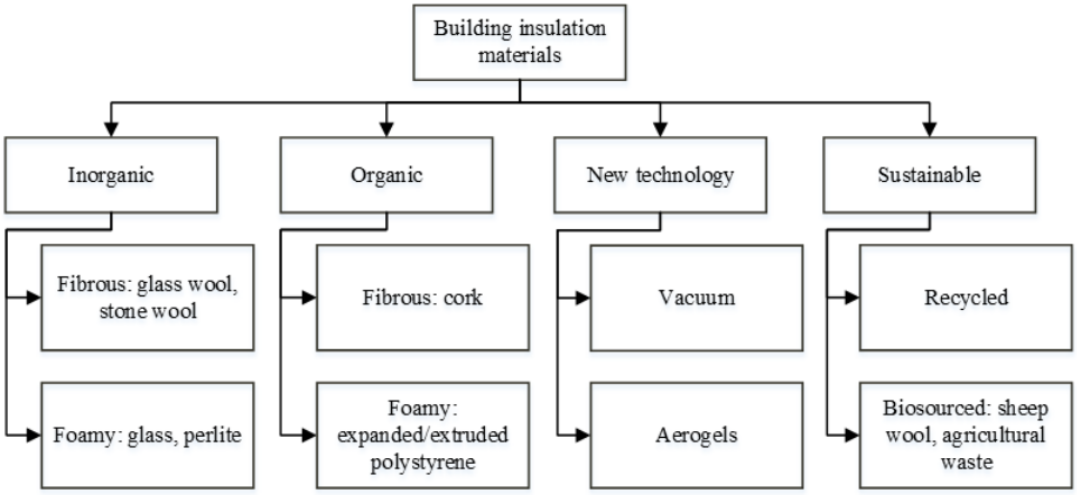

Figure 1.2. Categories of building insulation materials

Agricultural straw is a residue from harvesting crops, such as wheat, rice, barley, oat, corn, rye and rape. A large quantity of billion tons is produced every year around the world [4]. The treatment of straw is a largely disputed problem as a large fraction of straw is deposed by incineration and landfill except for the on-farm end uses such as animal bedding and feeding. Incineration of straw has negative effects, such as the toxicity, greenhouse gases emission and air pollution, and thus is banned in European Union countries. Mixing straw with soil generates methane during the straw's anaerobic decomposition, resulting in a higher global potential compared to the incineration [5]. Conversion straw waste to bio-sourced products for buildings provide a cost-effective

and eco-friendly approach to solve these issues. For a long time, straw has been used for insulation purposes with low density and low thermal conductivity due to its hollow internal structure. Zhao et al [6] reported that the insulation material derived from agricultural straw has a life cycle cost of 21 €/m^2 for 25 years span, which is lower than the insulation materials from municipal solid waste, industrial solid waste and traditional insulation materials including extruded polystyrene (XPS), expanded polystyrene (EPS), polyurethane (PU), phenol-foam (PF), perlite, rock wool and glass wool.

Rice straw is an important by-product of rice production, which is the third most important grain crop in the world behind wheat and corn [7]. According to Food and Agricultural Organization of the United Nations statistics (FAOSTAT) on the rice production [8], rice straw is estimated to be produced by about 40-112 thousand tonnes in France and 81-240 million tonnes in China when rice straw is assumed to be harvested about 2.7 to 8 tons for a hectare area [9]. Since rice straw has a high silica content, the voluntary intake by ruminant livestock is limited and the degradability in ruminal microorganisms is prevented. Also, the open burning of rice straw in the field produces threat to environment by producing larger amount of GHG emission. Nowadays, sustainable uses of rice straw are proposed in practice in order to make full use of the very viable by-product, such as the production of biofuels [10], biogas [11], enzymes [12] and composites [13]. Conversion the rice straw waste into the thermal insulation products for buildings can be a high-valued waste utilization approach.

Nowadays, straw composite materials available in market with competitive thermal insulating performance are mainly use the polyester bi-component fibres for thermic binding. The bi-component fibres are comprised of a core layer to resist high temperature and a coating layer for bonding straw fibres together at high temperature.

FBT insulation industries produce a rice straw insulation panel using polyester bi-component fibres as the binder. It is composed of 92% rice straw and 8% polyester bi-component. In practice, the panel production process follows four steps: (1) prepare fibres and pneumatic mixing rice straw fibres with bi-component fibres; (2) homogenize the mixture and formatting expected straw panel; (3) compress and cake the panels to the desired shape and size at high pressure and temperature; (4) cool and cut the panels into the required format. Figures 1.3 shows the industry line for the manufacture process. The rice straw panel has an average thermal conductivity value of 0.041 W/(m·K) with a density value of around 50 kg/m^3, which are comparable to common thermal insulation materials. Also, the rice straw panel is capable of regulating indoor air humidity due to its porous structure. However, the polyester binder used in the panel derives from non-renewable resources and more importantly it is indecomposable, and eventually cause negative impacts on environment.

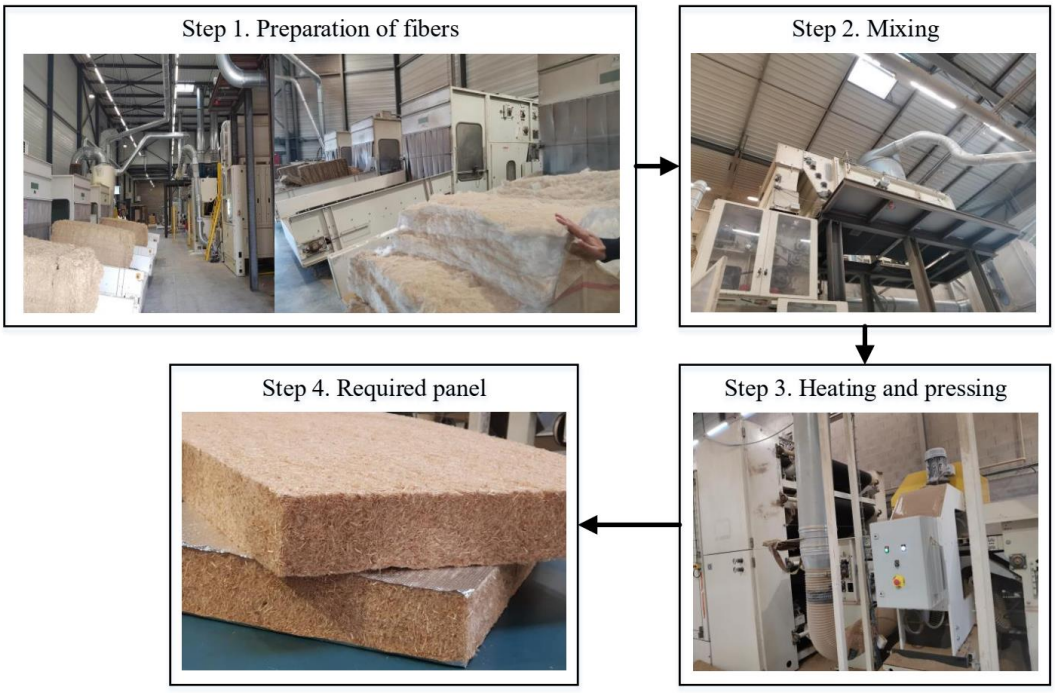

Figure 1.3.Production technology of rice straw panel from FBT isolation

1.2. Aim and objectives

This thesis aims to develop fully bio-sourced insulation materials from agricultural straw waste. The potentiality of utilizing rice straw and natural binders is explored for developing innovative insulating composite materials for building envelopes. The hygrothermal performance of the composite materials should be investigated in both the material scale and wall scale to evaluate their effectiveness. To achieve the targets, the specific objectives are as follows:

- Develop fully bio-sourced materials from rice straw fibres and natural binders with competitive hygrothermal performance. The water solubility issue of the composite materials should be investigated and solved. Various formulations can be designed and characterized to study the impacts of different factors (e.g., fibre size, binder type and binder ratio) on the hygrothermal properties.
- Experimentally study the hygrothermal behaviour of the developed material under various boundary conditions.
- Validate the effectiveness of a coupled heat and moisture transfer (CHM) model to simulate the hygrothermal behaviour of the proposed material.
- Improve the prediction accuracy of the CHM model by taking liquid water transport into account. The liquid water transfer coefficient is estimated by applying inverse identification technique.

1.3. Outline

The thesis is presented as follows:

Chapter 2 presents the state-of-art of the straw insulation materials for buildings. The characterization methods and standards of properties including thermal insulation,

moisture and durability are summarized. The general context on straw and the categories of straw insulation materials are presented. Thereafter, the properties are thoroughly reviewed and discussed with the consideration of different factors, such as density and fibre size. Next, the life cycle assessment of straw wall is presented by comparison with tradition wall. Finally, the findings, contributions and the open issues to be addressed are concluded.

Chapter 3 presents the development and characterization of innovative bio-sourced building insulation materials. Two nature binders, i.e., sodium alginate and chitosan are used. The manufacture process, characterization methods and experimental setup are described. By introducing the factors of binder type, fibre size and binder ratio, the proposed formulations are compared in terms of thermal insulation and moisture properties.

Chapter 4 presents the investigation of the hygrothermal behaviour of a rice straw alginate composite at wall scale under different boundary condition, including isothermal condition, non-isothermal condition and dynamic condition. Heat and moisture coupling effect in the wall panel is analysed and discussed.

Chapter 5 presents the validity of CHM model under isothermal condition, non-isothermal condition and dynamic condition. This model is implemented in a commercial COMSOL Multiphysics software, in which the finite element method is used. The CHM model is compared with a transient heat transfer model in their ability to simulate the thermal conditions within the wall.

Chapter 6 presents the study on the improvement of the CHM model by considering the liquid water transport. An inverse modelling technique is applied to estimate the liquid water permeability.

2. Literature review on the properties of straw insulation for buildings

2.1. Introduction

This chapter aims to provide a review of the available information on straw insulation for buildings. First, the characterization methods and standards of properties including thermal insulation, moisture and durability are summarized. Second, the general context on straw including microstructure and chemical composition is presented, which is followed as the introduction of two categories of straw insulation products, i.e., straw bale and straw composite. Third, the available studies on the properties including thermal insulation, moisture, and durability are thoroughly reviewed and discussed with the consideration of different factors, such as density and fibre size. In addition, the existing literature on the life cycle assessment of straw wall by comparison with tradition wall is presented. Finally, a summary of the findings and

contributions is presented and open issues to be addressed is outlined.

2.2. Characterization of thermal insulation

2.2.1. Thermal insulation properties

The main intrinsic properties of insulation materials regrading thermal insulation performance are thermal conductivity for steady state conditions, heat capacity, thermal diffusivity, thermal effusivity involved in transient conditions. The thermal conductivity of a material describes its ability of conduct heat, while the specific heat capacity measures the ability of store heat. A high specific heat capacity allows to delay the indoor temperature increase or decrease. Both the thermal diffusivity and thermal effusivity consider the ability to exchange and store heat. The thermal diffusivity measures the rate of heat transfer through a material, while the thermal effusivity measures the rate of heat absorption within a material under dynamic environment conditions. The thermal diffusivity can be expressed as the ratio of thermal conductivity to the product of density and specific heat capacity, and the thermal effusivity can be expressed as the square root of the product of density, thermal conductivity and heat capacity.

2.2.2. Moisture properties

Moisture inside a building material can affect heat flux, heat capacity, condensation, mould growth and structural integrity. Hygric properties are also indispensable parameters for modelling and analysis of the hygrothermal performance of the materials in building envelops. The key hygric properties includes sorption isotherms, water vapor permeability, moisture buffering value and water absorption coefficient. The sorption isotherms of a material measure its moisture storage ability,

which can be defined as the moisture content at equilibrium states when subjected to a series of relative humidity. The water vapor permeability of a material measures its ability of moisture transport for steady state conditions, which can be defined as the rate in which water vapor is transported. Water vapor resistance factor is a dimensionless parameter to represent the water vapor permeability of a material in comparison to an air layer with the same thickness. Moisture buffering value (MBV) of a material measures its ability to moderate variations in relative humidity when it is exposed to dynamic humidity conditions, which can be defined as the amount of water vapor uptake or release through unit exposed surface area when subjected to cyclic variations of relative humidity. Table 2.1 summarizes the established international or national standards for measuring the thermal insulation and moisture properties.

Table 2.1 Standard evaluation method for thermal insulation and moisture properties

Parameter	Symbol	Unit	Standard	Ref
Thermal conductivity	λ	W/(m·K)	EN 12664	[14]
			EN 12667	[15]
			EN 12939	[16]
			ASTM C518	[17]
Specific heat capacity	C_p	J/(kg·K)	ISO 11357	[18]
Thermal diffusivity	β	m^2/s	ISO 22007	[19]
Thermal effusivity	e	$W \cdot s^{1/2}/m^2/K$	ASTM D7984 - 16	[20]
Sorption isotherms	w	kg/m^3	EN 12571	[21]
Water vapor diffusion resistance factor	μ	-	EN 12086	[22]
			EN 12572	[23]
Moisture buffering value	MBV	$g/\triangle RH/m^2$	JIS A 1470-1	[24]
			NDRDTST protocol	[25]
			ISO 24353	[26]
Water absorption	W_p	kg/m^2	EN 1609	[27]
			EN 29767	[28]
	WA	%	EN 12087	[29]

2.2.3. Durability

The durability of an insulation material is crucial to guarantee potential energy saving in long term and service life of buildings. Accelerated ageing test, i.e., exposing materials to extreme environment conditions, is commonly conducted to evaluate the durability of a material as it can save much time. Due to the organic structure of straw insulation, the mold growth is one of the important parameters to characterize its durability as the mold plays a key role in straw degradation, making a compromise in materials' integrity and performance [30]. Different methods and standards are proposed to evaluate the resistance to mould growth, such as Johansson method [31], AWPA standard E24-06 [32], ASTM 2012 [33] and EN ISO 846 [34].

2.3. Straw context and thermal insulation products from straw

2.3.1. Composition and microstructure of straw

Straw is an agricultural by-product consisting of the dry stems or stalks of cereal plants, which is remained in the field after grain and chaff have been removed. The major structural components are cellulose, hemicelluloses and lignin [35]. Cellulose is a linear homopolymer with a partially crystalline structure that ensures strength and resistance to hydrolysis, while hemicellulose is an amorphous linear heteropolymer with little strength. Lignin has a complex three-dimensional structure that connects cellulose and hemicellulose, providing an impermeable cover in plant cell walls, enabling water resistance and strength to the cell wall. Other natural substances also exist in straw, such as water-soluble extractives, wax and ash. Thermal degradation behaviours of a material are strongly correlated to its components. Titiloye et al. [36] studied the thermal degradation characteristics of agricultural wastes including corn straw, corn cob, rice straw, rice husk etc. In their study, the TGA results showed that

most of the weight lost occurred at the temperature between 250 ºC and 450 ºC. Moreover, the corn straw had the highest weight loss of 70% and the rice straw had the lowest weight loss of 45%. This is due to the low ash content within corn straw and unusual high ash content within rice straw (see Table 2.2).

Straw is a porous material with multi-layer structure, which is generally referred as a hygroscopic material [37]. The porous nature enables the material to exchange water vapor with surrounding humid air, regulate fluctuations in relative humidity and thus improve indoor comfort [38]. The scanning electron microscopic (SEM) image of the cross section of wheat straw (see Figure 2.1) [39] shows a concentric ring with a lumen portion in the centre surrounded by porous structures. The epidermis in the outermost ring of stem is a dense layer with wax, ash and other inorganic substances that guarantees the mechanical strength and evaporation inhabitation, and beneath epidermis is a loose layer, which is composed of parenchyma and vascular bundles. The microstructure of straw can vary due to different species and plant growth environment. Figure 2.2 shows a comparison of the cross section between wheat straw and rice straw by using a scanning electronic microscopy [40], where the wheat straw has larger cells with larger variability in size and smother surface than that of rice straw.

Table 2.2 Composition of different types of straw (% dry matter) [41, 42]

Straw type	Cellulose	Hemicellulose	Lignin	Water-soluble	Wax	Ash
Wheat	38.6	32.6	14.1	4.7	1.7	5.9
Rice	36.5	27.7	12.3	6.1	3.8	13.3
Barley	34.8	27.9	14.6	6.8	1.9	5.7
Oat	38.5	31.7	16.8	4.6	2.2	6.1
Corn	38.5	28.7	15	5.6	3.6	4.2
Rye	37.9	32.8	17.6	4.1	2.0	3.0
Rape	37.6	31.4	21.3	-	3.8	6.0

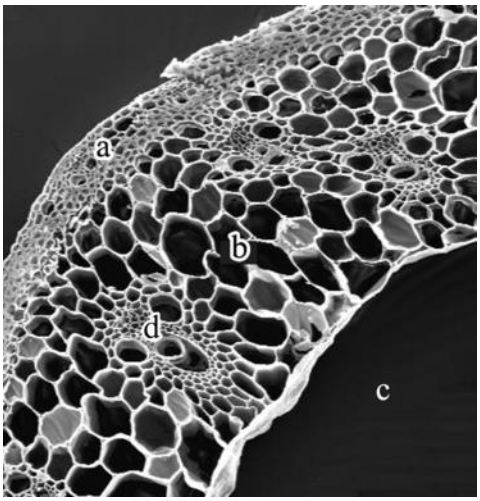

Figure 2.1. Cross section of wheat straw (a) epidermis, (b) parenchyma, (c) lumen, (d) vascular bundles [39]

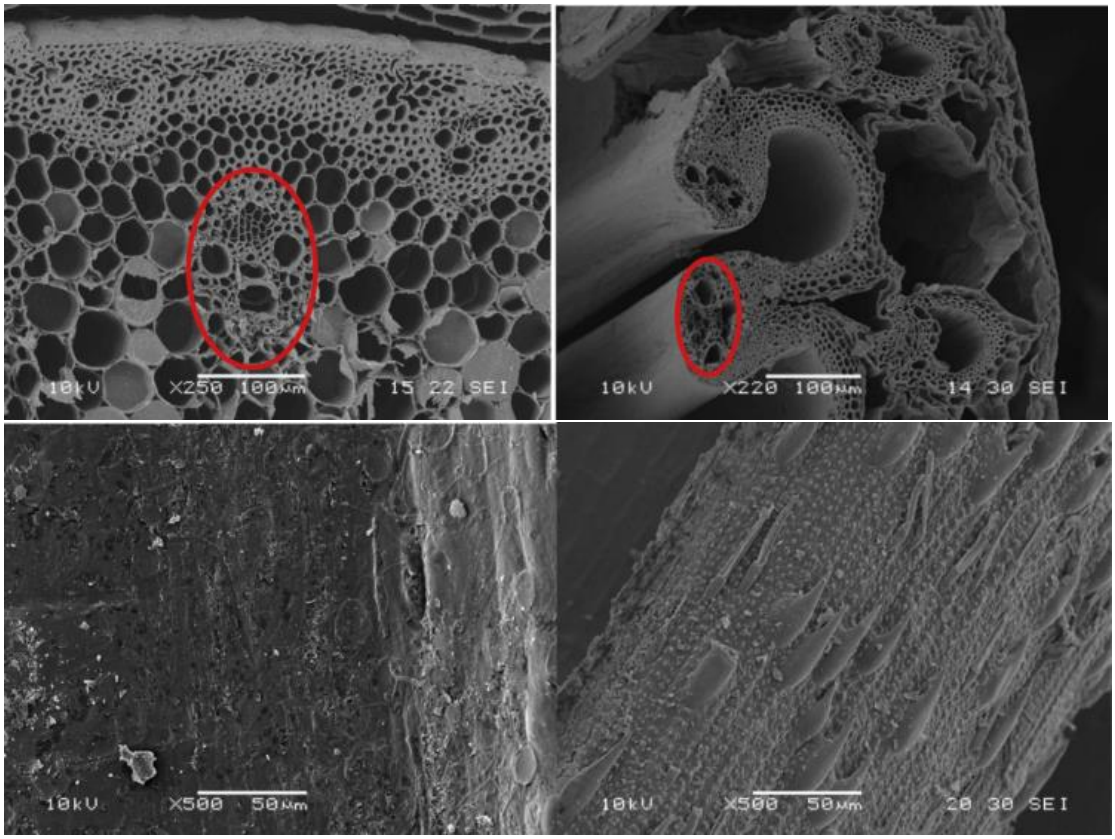

Figure 2.2. Cross section (above) and external surface (below) of wheat straw (left) and rice straw (right) [40]

2.3.2. Straw bale and straw composite

For the application in building construction, straw bale has been functionalized as load bearing or infilled insulation materials. It is produced directly from the deposited straw wastes in the field after harvesting crops. Baling machines are used to collect, compress and tie the straw wastes into compacted bales with steel or polypropylene twines. Through the baling process, a large range of density values can be produced and the orientation of the straw fibres within the bales can also be affected. For the application in construction and buildings, the straw bales are commonly laid flat with dimensions of 900 mm to 1000 mm length, 450 mm width and 350 mm to 375 mm high [43].

Another type of straw insulation attracting attention is straw composite, in which the straw fibres are usually moulded with alternative binders, including biocomponent fibres, inorganic materials, synthetic resins and natural adhesives. A typical technology of production of straw composite is as follows: (1) process the straw by methods such as cutting, smashing, crushing or milling to obtain short straw fibres in order to avoid the mixing difficulties in using their initial size [44]; (2) pneumatic, mechanically or manually mix straw fibres with binders and alternative functional materials; (3) formation of insulation panel/board, which is followed by a compressing step, such as pressing [45, 46], thermal pressing [47, 48] and high-frequency hot pressing [13, 49]) to achieve desired shape, stability and density; (4) dry or cure the panel/board in room condition or oven to accelerate the process.

2.4. Properties of straw bales

2.4.1. Thermal insulation properties

Various studies have reported a range of thermal conductivity values from 0.03 W/(m·K) to 0.1 W/(m·K) for straw bales, as shown in Table 2.3. The variability can be caused by, for example, the types of straw, the bale density, the orientation to heat flow, the ambient temperature and relative humidity. According to work of [50], a negligible variation was observed between wheat straw bales and barley straw bales. Figure 2.3 presents the thermal conductivity versus the density of straw bales as found in various studies. In the work of [51-54], a linear correlation was observed, where thermal conductivity generally increased with density, while in the work of [55-57], the thermal conductivity was relatively independent of density. Additionally, according to the work of [58], the lowest thermal conductivity values were obtained in bale densities ranging from 60 kg/m^3 to 80 kg/m^3, and densities not in that range exhibited higher thermal conductivity.

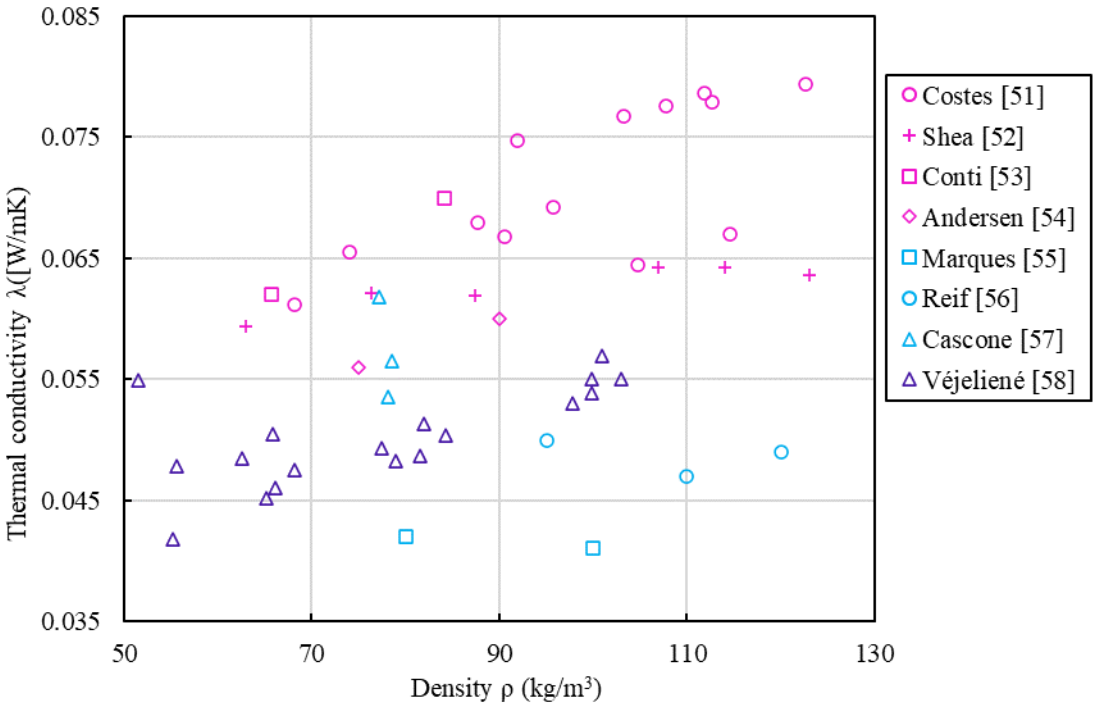

Figure 2.3. Thermal conductivity versus density based on the studies from Costes [51] , Shea [52], Conti [53], Andersen [54], Marques [55], Reif [56], Cascone [57], Véjeliené [58]

The thermal conductivity of straw bales was highly influenced by their orientation to heat flow, with the lowest thermal conductivity value of parallel and perpendicular oriented straw differing about 1.8 times reported by Véjeliené et. al [59]. Figure 2.4 gives the box plot of thermal conductivity values for the parallel, perpendicular and not specified orientations from various studies. It can be seen that the perpendicular orientation always showed the lowest thermal conductivity values from minimum, maximum, median, first quartile and third quartiles, indicating the perpendicular orientation is preferable to improve thermal performance in buildings. Platt et. al [43] developed a laboratory scale baler and baling process to orientate the straw preferentially, and found that changing the parallel orientation to perpendicular orientation decreased the thermal conductivity by 28% (from 0.078 to 0.056 W/(m·K)).

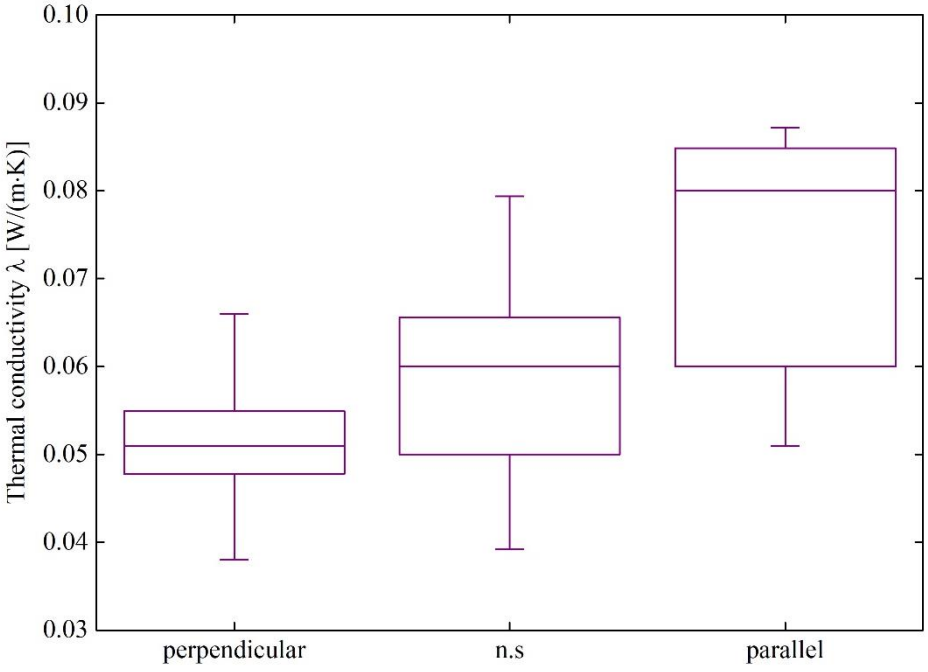

Figure 2.4. Box plot of thermal conductivity for different bale orientation based on studies from Table 2.3

Generally, the thermal conductivity of straw bales lineally increased with the

increase of ambient temperature and internal moisture content. Douzane et.al [60] investigated the effect of temperature on the thermal conductivity of both the parallel and perpendicular orientated straw bales by applying guarded hot plate. In their study, a linear correlation between the thermal conductivity and mean temperature ranging from 10 ºC to 40 ºC was obtained as:

$$\lambda = \lambda_0 (1+ aT) \tag{2.1}$$

Where T represents the mean temperature, λ_0 represents the thermal conductivity of straw bales at 0 ºC, and a represents the experiment coefficient, for parallel oriented straw bales: λ_0 equals to 0.067 with a equaling to 0.0078, and for perpendicular orientated straw bales: λ_0 equals to 0.046 with a equaling 0.009.

Cascone et.al [57] determined an exponential function to describe the correlation between the thermal conductivity and temperature of straw bales by using a heat flow apparatus. The mean temperature ranged from 25 ºC to 35 ºC, and the function after curve fitting was expressed as:

$$\lambda = 0.0534e^{(0.0026T)} \tag{2.2}$$

According to the work of [61], the thermal conductivity of straw bales at dry state was increased by 20% when they were conditioned at 80% RH and 23 ºC and reached moisture content equilibrium. The only research that simultaneously consider the influence of multiple variables on the thermal conductivity and thermal diffusivity of straw bales was done by Sabapath et.al [62]. In their study, the effect of bale density, bale orientation, ambient temperature and relative humidity were taken into account. Specifically, samples were prepared in different densities ranging from 50 to 95 kg/m^3 and three orientations, i.e., perpendicular, random and parallel. The thermal conductivity and thermal diffusivity values of these samples were measured by a

transient plane method at temperature of 25-45 ºC and at relative humidity of 0-80% RH. The orientation was found to have the largest impact on both the thermal conductivity and thermal diffusivity among all the variables. Additionally, the random and perpendicular oriented samples exhibited similar thermal insulation properties and followed similar trends with variable variations to some extent, while the parallel samples exhibited obvious difference. For example, an increase of 1.5 times in thermal conductivity values was found for random and perpendicular orientation, whereas that of 2.5 times for parallel orientation when they were conditioned at high humid case of 80% RH compared to the dry state. Moreover, two polynomial functions were determined for parallel and random/perpendicular oriented respectively:

$$\lambda_{parallel} = -0.0103\rho^2 + 2.196\rho + 1.573(\%RH) + 0.478\,T - 46.072\ [mW/mK] \quad (2.3)$$

$$\lambda_{random/perpenticular} = -0.00002\rho^2 + 0.317\rho + 0.375(\%RH) - 0.042T + 30.794[mW/Mk] \quad (2.4)$$

Table 2.3 Thermal conductivity of straw bales as found in literature published by various authors

Year	Authors	Straw type	ρ (kg/m^3)	Mean temperature (ºC)	MC/ RH (%)	Fibre orientation	Measuring instruments	λ (W/m·K)	Ref
2021	Mehravar et al.	Wheat	61	10	-	-	Heat flow meter	0.047	[63]
2020	Cornaro et al.	-	106	-	-	Perpendicular	-	0.066	[64]
2019	Marques et al.	Rice	80-100	10	0	-		0.039	[55]
					RH 50%			0.041-0.042	
					RH 80%			0.045-0.048	
2019	Sabapathy et al.	Rice	68	30	0	Parallel	Transient plane source	0.08	[62]
						Perpendicular		0.057	
						Random		0.049	
					RH 40%	Parallel		0.134	
						Perpendicular		0.059	
						Random		0.06	
					RH 60%	Parallel		0.165	
						Perpendicular		0.078	
						Random		0.075	
					RH 80%	Parallel		0.182	
						Perpendicular		0.084	
						Random		0.07	
2019	Cascone et al.	Wheat	78	20-35	MC 8%	Random	Heat flow meter	0.056-0.058	[57]
2017	Costes et al.	-	68-123	10	RH 50%	-	Hot plate	0.061-0.079	[51]
2017	D'Alessandro et al.	-	80	22	RH 45%	Parallel	Hot plate	0.051	[65]
	Munch-Andersen et al.	-	62-150	-	-	Parallel		0.057-0.082	

		-	75-150	-	-	Perpendicular		0.038-0.057	
2016	Douzane et al.	-	80	10-40	-	Parallel	Hot plate	0.072-0.088	[60]
		-	-	-	-	Perpendicular		0.05-0.063	
2016	Conti et al.	Triticosecale	66-84	19	MC 12%	-	Hot box	0.062-0.07	[53]
2016	Reif et al.	Wheat	95-120	-	0	-	-	0.045-0.046	[56]
					RH 50%			0.047-0.05	
					RH 80%			0.057-0.059	
2015	Volf et al.	-	98	-	-	-		0.065	[66]
2012	Shea et al.	Wheat	63-123	10	RH 50%	Random	Hot box	0.059-0.064	[52]
2011	Vėjelienė et al.	Barley	63-121	-	-	Parallel	Hot plate	0.085-0.087	[58]
			50-103			Perpendicular		0.042-0.057	
2005	Goodhew and Griffiths	-	60	-	-	-	Thermal probe	0.067	[67]
2003	Ashour et al.	Barley	69-98	10-32	-	-	-	0.03-0.094	[68]
		Wheat	82-138	10-34	-	-	-	0.03-0.099	
2001	Andersen et al.		76	10	0	Parallel	-	0.057	[54]
						Perpendicular	-	0.052	
1998	Christian et al.	-	62	-		Parallel	Hot box	0.082	[69]
		-	81			Perpendicular		0.057	
1993	McCabe et al.	Wheat	133	20	MC 8.4%	Parallel	-	0.061	[70]
		-	-	-	-	Perpendicular	-	0.048	

2.4.2. Moisture properties

The equilibrium moisture content in straw bales is dependent on the surrounding environment, i.e., relative humidity and temperature [50]. Several studies developed equations to predict the equilibrium moisture content by measuring the relative humidity and temperature within straw bales. Hedlin et al [71] described the correlation between the moisture content within straw and ambient relative humidity at 21.1 ºC for five different types of straw. Perry and Green [72] concluded that the sorption isotherm was independent of temperature in the range of 15-50 ºC. Lawrence et al. [73] developed an empirical model to predict the moisture content ignoring the temperature effect as the temperature in UK (where the study carried out) was within the range of 15-50 ºC. This model, however, is inapplicable to countries with different climate conditions, such as Canada and northern China.

The different types of straw was reported to have negligible impact on the sorption isotherms of straw bales according to the work of [40, 74], while the straw bale from barley was reported to exhibit higher adsorption rate than that from wheat by Ashour et.al [68], which was explained by the porous structure differences observed between barley straw and wheat straw. Yin et.al [40] found that the cut straw with open end reached the equilibrate state more rapidly with the environment by 25% compared to the folded straw with close end. This phenomenon was explained by the larger aspect ratio of the open-ended straw, resulting in more accessed pores for entering moisture content compared with that of closed ended straw. Thus, it was indicated that straw bales trimmed to size can equilibrate more rapidly than straw bales consisting of straws folded at the edge of the bale [32]. A hysteresis pattern between sorption isotherms of straw bales was observed in the work of [74, 75]. Rice straw had a smaller hysteresis than wheat straw and oat straw according to the work of [55, 74]. This indicated that rice straw bales appeared to rapidly recover after wetting, contributing to its hygrothermal performance and durability.

Water vapor resistance factor of straw bales was found highly correlated to their density and a lower density resulted in a lower water vapor resistance factor due to more open spaces between straw fibres [55, 76]. Marques et. al [55] characterized the water resistance factor of rice straw bales at two densities (i.e., 80 and 100 kg/m^3) by dry cup and found that the higher density led to an increase of the water vapor resistance factor by 52% (from 3.25 to 5.47). Lebed and Augaitis [76] determined a polynomial function to describe the correlation between the water vapor resistance factor and density (ranging from 60 to 180 kg/m^3) by using wet cup method:

$$\mu = 2.335\text{-}0.0127\rho + 0.0000892\rho^2 \quad (2.5)$$

The water absorption of straw bales is highly correlated to their porosity and hygroscopicity. Marques et.al [55] measured the water absorption of rice straw bales at two different densities, i.e., 80 kg/m^3 and 100 kg/m^3 following the standard EN 1609. An increase mass of close to 100% was found at the higher density due to more straw available to absorb water and less space to drain water after immersion. Lebed and Augaitis [76] reported that 60-80% by weight of straw was absorbed during the first 10 hours and then slightly increased, which may be related to the elimination of remaining air from the structure of straw.

2.4.3. Durability

The mainstream adoption of straw bales as building insulations remains restricted in consideration of the long-term durability. Due to the chemical composition of straw including cellulose, hemicellulose and lignin, straw decomposition can be occurred when ambient hygrothermal condition supports micro-organisms, thus leading to performance degradation and even security issues of buildings. The optimum range of temperature for mould growth is 20-70 ºC, and many micro-organisms are restricted at temperatures below 10 ºC [73]. According to the studies of [77, 78], no mould growth was observed in wheat straw samples when they

were subjected to climate conditions below 80% RH at 10 ºC and 70% RH at 25 ºC for a 100-day period. Various studies reported that the moisture content within straw bales exceeding the thresholds values ranging from 14% to 27% can cause straw degradation [79, 80]. Generally, the initial moisture content within straw bales at construction not exceeding 14-15% and the moisture content at operation not exceeding 25% are recommended [30]. Robinson et.al [81] found that when the ambient temperature was below 10 ºC, straw degradation were not occurred despite of the moisture content within straw bales exceeding to 25% for a prolonged period. Above guidelines give a clear limit on moisture content affecting the durability of straw bales, however, the consequences of exposure duration and subsequent degradation severity are not fully understood.

Thomson and Walker [30] studied and evaluated whether the repeated mould growth was limited for wheat straw bales after an initial mould colonization by conducting two experiments. The first experiment compared the mould growth between fresh wheat straw samples and a wheat straw sample from a three-year-old wall by exposing them to a favourable condition for mould growth at 87% RH and 21.5 ºC for 20 days. The old straw sample was found to have not mould growth, while a rapid mould growth was found for the fresh straw samples. The second experiment cyclically exposing the six fresh wheat straw to different elevated levels of relative humidity (from 78% to 91%), including a 28-day period of high relative humidity, 7-day period of drying and 14-day period of re-exposing to the same high relative humidity. The mould growth was not detected a second time for all the samples following drying and re-exposure. Above results revealed that successive mould growth is not likely to occur if only transient increases in humidity are detected in straw bales.

2.5. Properties of straw composites

2.5.1. Thermal insulation properties

The thermal conductivity of different agricultural waste, i.e., wheat straw and barley straw, mixed with soil and sand were studied in the work of [82]. Among composite materials containing 25 wt%, 50 wt% and 75 wt% of straw fibre content, the composites with 75 wt% fibre content exhibited the lowest thermal conductivity, 0.195 W/(m·K) for wheat straw and 0.154 W/(m·K) for barley straw, respectively. This can be attributed to a higher porosity of the composite material with a higher fibre content, leading to the decrease of its thermal conductivity as air has a lower thermal conductivity than solid material [83]. Binici et.al [84] examined the influence of both fibre content and compaction pressure on the thermal conductivity of corn straw-epoxy composites. Two different fibre content, i.e., 57 wt% and 66 wt%, and five compression pressures, i.e., 0.07, 0.12, 0.17, 0.27 kgf/m^3, were used in sample forming. The lowest thermal conductivity 0.075 W/(m·K) was obtained with 66 wt% of fibre content and 0.07 kgf/m^3 of compaction pressure.

Labat et.al [85] studied the thermal conductivity of straw-clay composites at different densities, which were controlled by adding different percentage of straw fibre content. Their study found that the thermal conductivity values linearly increased from 0.071 to 0.12 W/(m·K) against density values ranging from 241 to 531 kg/m^3. However, a polynomial rather than linear function between density and thermal conductivity was found for rape straw-clay composites with density ranging from 235 to 714 kg/m^3 according to the work of [86].

Belayachi et. al [44] found that the straw-gypsum composites with density values ranging from 255 to 456 kg/m^3 achieved low thermal conductivity from 0.064 and 0.086 W/(m·K) with acceptable self-bearing ability following the standard NF EN 1992-1-1. Ismail et.al [87] have developed the composite materials from straw fibre, lime and gypsum plaster with three natural additives (hemoglobin, casein and gelatin) to reduce their thermal conductivity and guarantee their self-bearing ability. The thermal conductivity values were found to be decreased after integrating all the additives except for the combination of 5 wt% hemoglobin and 5wt% casein

resulting a denser composite than that of without additive. But it should be noted that use of hemoglobin significantly decreased the mechanical properties in the same time due to the porous structure created. In contrast, the mechanical strength was improved when gelatin was added to partially substitute the plaster because gelatin causes a change in the plaster microstructure with the irregular shape and small size of crystals compared to the original large rod-like crystals from the SEM image analysis. The lowest thermal conductivity is 0.057 W/(m·K) when the self-bearing mechanical properties was ensured.

Many studies attempt to use natural binders, such as starch, alginate and casein, to obtain light and completely biodegradable insulation materials for buildings. Palumbo et.al [88, 89] prepared insulation panels from different agricultural wastes, i.e., barley straw, corn pith and rice husk, mixed with starch or alginate solution. The thermal conductivity of the insulation panels was obtained from 0.052 to 0.098 W/(m·K) for the density values ranging from 89 to 223 kg/m^3. Tůmová et.al [90] used casein as the binder and obtained straw composites with low thermal conductivity values between 0.045 and 0.056 W/(m·K) for the density values from 72 to 92 kg/m^3. Also, it was found that the cut straw with smaller fibre length could decrease thermal conductivity compared with the uncut straw. Wei et.al [13] analysed the influence of fibre size on thermal conductivity of rice straw fibre based insulation boards. In their study, five different size distributions of fibre were obtained by sieving, and the thermal conductivity values of the boards was found to be decreased with the increase of mass fraction of large fibres. Rojas et al. [91] found that the fibre length exerted the greatest impact in determining the thermal conductivity of wheat straw or corn husks based insulation materials compared to the other three parameters including boiling time, NaOH concentration and blending time.

2.5.2. Moisture properties

Figure 2.5 shows the measured hygroscopic adsorption isotherm of straw composites from different studies [83, 92, 93]. No significant correlation between adsorption isotherm and

density was found, while a higher moisture adsorption rate was observed for a higher porosity based on these studies. Rahim et.al [93] compared the sorption isotherms between hemp lime concrete and rape straw lime concrete with similar density and porosity. The adsorption rate of rape straw lime concrete was higher after the relative humidity reached 75%, and this may be due to the a finer and more homogenous porosity observed in rape straw lime concrete which accelerate the adsorption rate. However, different types of straw in the reinforced concrete has been proposed of having negligible impact on their equilibrium moisture content according to the work of [94].

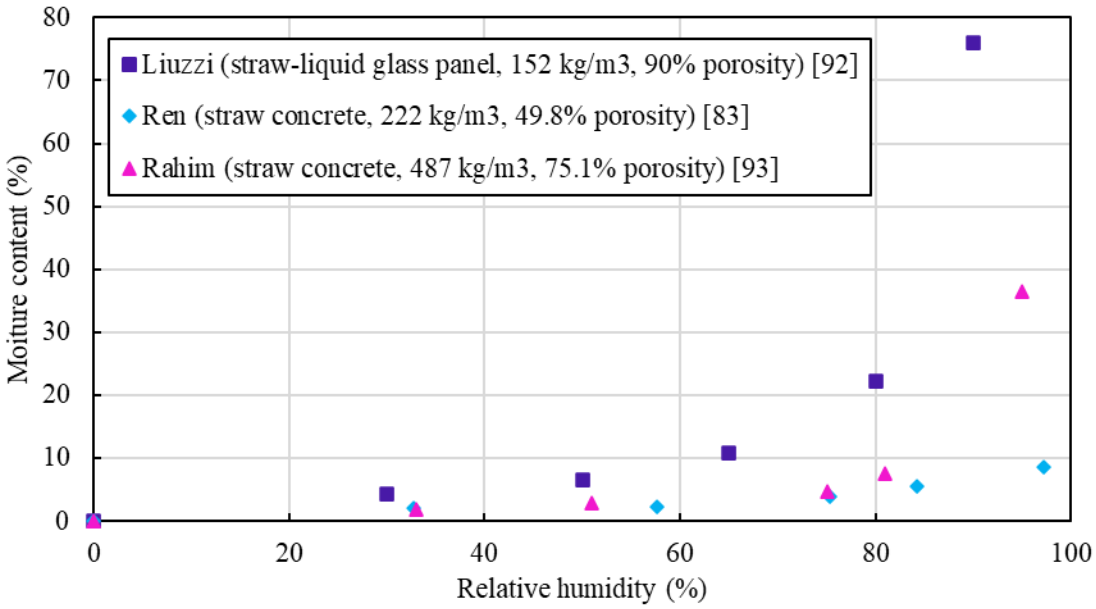

Figure 2.5. Equilibrate moisture content based on studies from Liuzzi [92], Ren [83]and Rahim [93]

Figure 2.6 summarized the water vapor resistance factor measurements by both the dry cup (denoted by solid point) and wet cup (denoted by hollow point) of straw composites against density from different studies [85, 92, 93, 95-97]. The water resistance factor by wet cup was systematically lower than that determined by dry cup, and this is attributed to the fact that additional liquid transfer driving by capillary forces occurs at high ambient relative humidity. Also, the water vapor resistance factor was shown to be correlated with density based on these

studies, except for the lavender straw composite. The observed low water vapor resistance factor for lavender straw composite can be attributed to the presence of highly hydrophilic components in the lavender plant, such as phenolic compounds, flavonoids, anthocyanins or tannins.

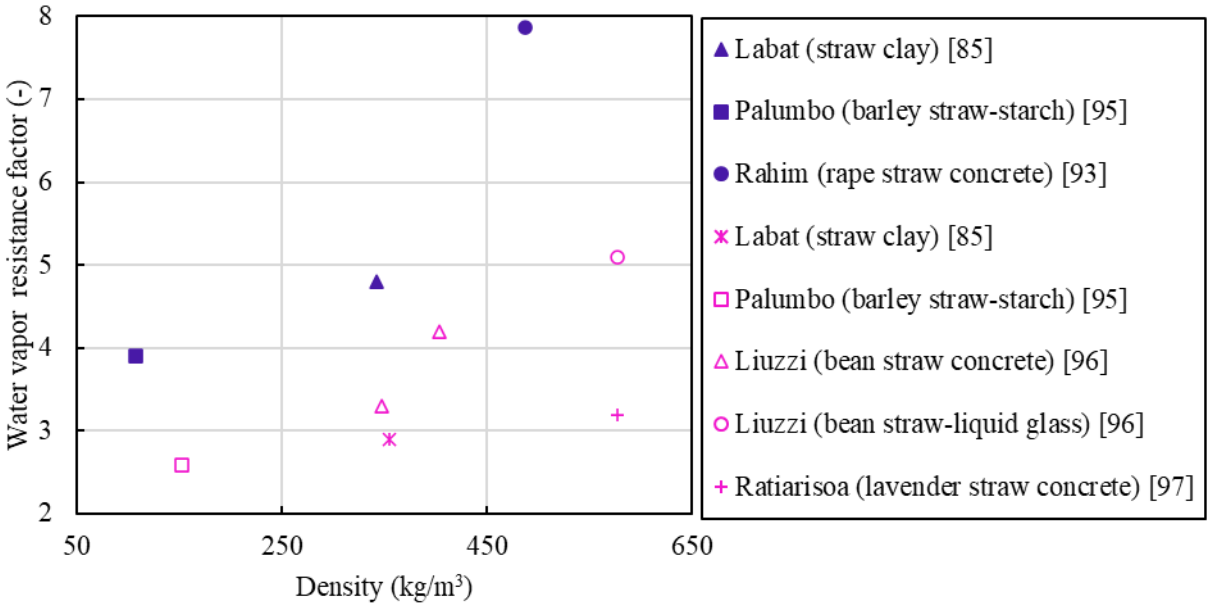

Figure 2.6. Water vapor resistance factor (purple and pink represent wet cup and dry cup respectively) versus density based on studies from Labat [85], Rahim [93], Palumbo [95], Liuzzi [96], Ratiarisoa [97]

The moisture buffering value (MBV) of straw composites obtained was found from 2.59 to 3.85 for the density values between 108 kg/m^3 and 577 kg/m^3 from various studies [93, 95, 97, 98]. Therefore, straw composites can be classified as “excellent” following the grading established by Rode et.al [99]. Ahmad et.al [98] studied the moisture buffering capacity of corn straw reinforced concrete. Three different weight percentages of corn straw to binder, i.e., 33 wt%, 55 wt% and 100 wt% were used, and the results revealed that the MBV increased with an increasing straw content. Rahim et.al [93] measured the MBV of rape straw concrete samples in different thickness according to the NORDTEST protocol [100], and it was found that the MBV increased by 13.1% (from 2.29 to 2.59) when the thickness increased from 3 cm to 7 cm.

Few studies have studied the water absorption of straw composite materials. In one of them, corn straw reinforced concrete samples were immersed in water for 15 days, and it was found that the samples with the averaged 14 mm fibre size had a larger amount of water absorbed in than that of samples with 9 mm fibre size at any given fibre content (between 5 wt% and 30% wt) [101]. Also, the water absorption rate was found the maximum during the first 60 minutes and decreased gradually for all the formulations. The highest total water absorption rate of 77.9%, was obtained for the formulation with a fibre content of 30 wt% and a size of 14 mm. This can be attributed to the hydrophilic nature of the corn straw fibre and the higher porous structure created by the larger fibre size. Zuo et.al [102] examined the influence of silicone-acrylic emulsion addition on water absorption of rice straw magnesium cement composites by immersing the composite samples in water for 24 hours according to GB/T 24312. A decrease of water absorption by 32% was observed as the silicon-acrylic emulsion increased by 10%. Table 2.4 shows the thermal and moisture properties of straw composites.

Table 2.4 Thermal and moisture properties of straw composites as found in literature published by various authors

Straw type	Fibre length (mm)	Binder type	Fibre/binder mass ratio	ρ (kg/m^3)	Porosity	λ (kg/m·K)	μ (-)		MBV (g/m^2%RH)	Ref
							Wet	Dry		
Rye, barley, wheat, oats, rice	20-40, <80	Liquid glass	1/1.4	200-220	-	0.056-0.063	-	-		[46]
Rice	10-30	Methylene diphenyl diisocyanate (MDI) resin	1/0.08	200-350	-	0.051-0.053	-	-		[13]
Corn	0.5-4	Epoxy	60/30, 60/45	260-410	-	0.075-0.159	-	-	-	[84]
Rape	-	Clay	-	241-531	-	0.071-0.12	4.8	2.9	-	[85]
Rape	-	Clay	1/2.4	438	-	0.07	-	-	-	[86]
Wheat	<50	Tradical PF70, Tradical Thermo, plaster	0.2-0.4	-	-	0.054-0.069	-	-	-	[87]
Rye	-	Casein	1/0.6, 1/0.5, 1/0.4, 1/0.3	72-93	-	0.045-0.056	-	-		[90]
Barley	-	Sodium silicate solution	70/30	152	0.9	0.058	-	2.59		[92]
Rape	-	Lime	14/36	487	0.75	-	7.87	-	2.9	[93]
Barley	-	Starch	81/19	108	0.92	0.042	3.9	3.4	3.2	[95]
Bean	-	Clay and cement, liquid glass	0.49	348-580	-	0.075-0.096	-	3.3-5.1	-	[96]
Lavender	-	Pozzolanic	0.46, 1.51	557, 661	-	0.142, 0.146	-	3.2, 2	3.85, 3.5	[97]

Rape	0-120	Bone glue with sodium lignosulfonate	1/0.35	500-700	-	-	33-36	23-26	-	[103]
Flax	-	Liquid glass	1/2.4, 1/2	312, 336	-	0.084, 0.085	-	-		[104]

2.5.3. Durability

Belayachi et.al [44] studied the changes of thermal insulation and mechanical performance as well as the degradation of both wheat straw-plaster and barley straw-plaster composites when they are exposed to dry-wet and freeze-thaw cycling. The composites were cyclically immersed for 1 hour in water prior to natural drying for 71 hours during dry-wet tests, and they were exposed to a cycle between -10 ºC and 40 ºC during the freeze-thaw tests. The results demonstrated that both the composites were more sensitive to the dry-wet aging than the freeze-thaw aging. Also, although the barley-based material showed the lower thermal conductivity and better mechanical properties in non-aged state, the barley-based material was more likely to lose its performances under the aging conditions due to its more porous structure resulting in higher moisture absorption rate compared with the wheat-based material. Significant mass loss was observed at the 35th cycle for the barley straw composite, while the wheat straw composite remained relatively complete at the 40th cycle, as shown in Figure 2.7.

There is high possibility of mould growth in straw-based materials when they are subjected to excessive moisture environment. In the work of [105], mould growth was found on barley straw after two weeks exposing to 93% RH, whereas no mould growth was observed when exposing to 84% RH. A study carried out by Giroudon et.al [106] found that the mould growth of straw composites was dependent on the different types of straw, i.e., barley straw and lavender straw. In their study, the earth composites containing 3% of barley straw or lavender straw were exposed to a favourable environment for mould growth, i.e., 93% RH and 30 ºC. The lavender reinforced composite was found to be more resistant to mould growth than barley reinforced composite, and this result was explained by the special chemical composition of lavender containing polyphenols and aroma with antibacterial, antifungal and insecticidal qualities. A comprehensive study that have been done by Viel et.al [107] revealed that the pH of a given material is a significant indicator of mould growth as the use of alkali treated rape

straw to prepare composites does not show decay after exposing them to a unfavourable condition, i.e., 90% RH and 30 ºC for three months. Also, the water absorption of material was found to be an influencing factor as the addition of paraffin decreased water content within composite, leading to lower kinetics of mould growth on its exposed surface.

Figure 2.7. State of barley and wheat straw composites after 35 and 40 drying-wetting cycles respectively

2.6. Life cycle assessment

Life cycle assessment (LCA) is commonly used to assess the environmental footprint of a insulation product. Generally, the LCA is performed using cradle-to-grave approach (where the evaluation performed from the material extraction to the disposal) or cradle-to-gate (where the evaluation does not include the use and the disposal phases) approaches [108]. D'Alessandro et al. [109] compared the cradle-to-grave assessment of a straw bale and other insulation materials (see Table 2.5) based on two impact categories. In this case the functional unit is 1 kg of materials. The straw bale was shown to have low values of primary energy and global warming potential compared with the traditional mineral insulation materials. González et al. [110] studied the energy and carbon footprints of straw bales and straw-clay blocks for local conditions by comparison with traditional fired bricks and concrete blocks in Andean Patagonia. It was found that the carbon emission and embodied energy of straw bales and straw-clay blocks

to cover 1 m^2 of wall was smaller compared to the fired bricks and concrete block, as shown in Table 2.6. Considering that different materials could vary in density and thermal conductivity values, a more appropriate unit such as the mass of materials to provide a equal thermal resistance, could be used for a fair comparison. Bories et al. [111] conducted the LCA on the entire manufacturing process of clay bricks with and without the incorporation of biobased additives, i.e., 1 wt% wheat straw, 2 wt% olive stone flour, 2 wt% glycerol carbonate and 2 wt% dimethyl carbonate. The functional unit was 1 m^2 clay tablets with an equivalent thermal resistance of 0.035 m^2W/K. It was found that the additives reduced the environmental impact compared to the pure clay brick.

Table 2.5 Comparative life cycle analysis of straw bale with other insulation materials [109]

Insulation	Primary energy inputs (MJ-eq.kg)	GHG impact ($kgCO_2$-eq/kg)	Processes included
Straw bale	0.89	0.18[b]	E+M+T
Expanded polystyrene	114	107	E+M+D+T
Extruded polystyrene	107	13.67	E+M+D+T
Mineral wool	44	2.31	E+M+T
Kenaf	39	2.09	E+M+T
Hemp	n.a.[c]	0.15[b]	E+M+T

[a] E = raw materials extraction; M = manufacturing; T= transports; D = disposal.

[b] Without carbon sequestration.

[c] n.a. = not available.

Table 2.6 Embodied energy and global warming potential of straw bales, fired bricks and concrete blocks for 1 m^2 of wall [110]

Number required per m^2 of wall	Thermal conductivity (W/m·K)	Thermal transmittance (W/m·K)	Embodied energy (MJ/m^2)	Global warming potential ($kgCO_2$-eq/m^2)
85 Fired bricks	0.90	3.9	488[a]	30
11 concrete blocks	0.64	3.2	169[b]	9.6
7 straw-clay blocks	0.18	0.86	40	3.4
3 straw bales	0.07	0.16	28	2.5
3 half straw bales	0.07	0.32	14	1.3

[a] Includes 700 km transport; [b] Includes 700 km transport in 10% of weight due to cement

Quintana-Gallardo et al. [112] compared the cradle-to-gate assessment of a rice straw wall and a traditional double brick wall. The straw wall was more insulating with thermal resistance doubled that of the traditional wall. It was found that the environmental impact of the straw wall was lower in every category except for the land use and water use compared to the traditional double brick wall. Moreover, by substituting the two different waste management, i.e., burning straw or mix straw with soil, 1 m^2 rice straw wall can prevent the emission of 18.85 $kgCO_2$-eq and 52.64 $kgCO_2$-eq, respectively. Cornaro et al. [64] conducted the LCA of an innovative wall (which was composed of straw bale and natural plasters) and a traditional clay brick wall. In this case the straw wall and the traditional wall had the same thermal resistance of 6.5 m^2W/K and the functional unit was the area of the wall package installed in a reference building. The obtained results demonstrated that the CO_2 equivalent emission and the embodied energy of the straw wall was 50% lower than the traditional wall regarding the phases of production and construction. Cascone et al. [113] compared the embodied energy of a platform system made of pressed straw and a cross laminated timber (XLAM) system with the same thermal performance. The platform system led to a reduction of embodied energy of 60% compared with the XLAM system.

A dynamic LCA and a static LCA were done by Zieger et al. [114], who compared the cradle-to-gate assessment of a wheat straw wall and a traditional concrete wall with an insulation layer of mineral wool. Both the walls had the same thermal resistance value of 7.3 m^2W/K and the functional unit was 1 m^2 of wall. It was found that the tradition wall had minor changes in equivalent carbon emission regardless of the LCA method, while the straw wall had larger difference by using different LCA method. Specifically, the equivalent carbon emission calculated by dynamic LCA was lower than the static LCA calculated at 100 years and the dynamic equivalent carbon emission converged toward the static one after a long-time horizon, as shown in Table 2.7. This is because the traditional wall contributes to the climate change from the first year, whereas the straw wall has a cooling effect for several years, which are

ignored when using the static method.

Table 2.7 Relative global warming potential of straw wall and concrete wall calculated by static and dynamic life cycle analysis [114]

Insulation	Conventional ($kgCO_2$-eq/FU)	Straw-based ($kgCO_2$-eq/FU)
Static GWP100	79.8	26.3
	GHG	GHG (min/max)
Dynamic DLCA 20	60.0	-56.5
Dynamic DLCA 100	70.8	-22.2/-9.8
Dynamic DLCA 500	71.8	9.8/14.3
Dynamic DLCA 1000	71.2	11.1/13.7

*Straw's end of life is regarded as 50% composted and 50% incinerated

2.7. Conclusions

The appropriate utilization of straw waste in building insulation materials is a promising approach for energy efficiency and decarbonization. In this chapter, straw insulation was categories as straw bale and straw composite. Straw bales are produced by using bale machines to collect and compress the deposited straw after harvesting crops. Straw composites are prepared by moulding straw fibres with alternative binders. This chapter presented the available studies on the thermal insulation, moisture and durability of straw insulation with the consideration of different factors. Also, the environmental impact of straw wall was also proposed by comparison with the traditional wall. The main findings are drawn as follows:

- Thermal conductivity is the most significant property that characterizes the effectiveness of a thermal insulation material. Thermal conductivity values of straw bales are reported to have high variability in the range of 0.03 to 0.08 W/(m·K), which can be caused by various factors, including the types of straw, the bale density, the orientation to heat flow, the ambient temperature and relative humidity. Meanwhile, increasing fibre content and fraction of large fibres within straw composites effectively decreased their thermal conductivity.

- The moisture properties of straw bales and straw composites have been observed to be influenced by various factors. Straw bales with open-ended straw could reach the equilibrate humidity more rapidly with environment than bales with close-ended straw. The water vapor permeability of both straw bales and straw composites have been observed to be dependent on their density. However, the types of straw and the density have no significant impact on the moisture absorption of straw composites. Furthermore, factors such as the fibre content, the hydrophilic nature of the fibre, the fibre size, the porosity and the thickness affected the moisture buffering capacity and water absorption.

- The durability of a material are crucial aspects to ensure the long service-life of the building. A favourable hygrothermal conditions for micro-organism results in mould growth, thus leading to straw degradation. The moisture content at operation not exceeding 25% is generally recommended to prevent degradation of straw bales.

In general, straw is a promising raw material for obtaining cost-effective and eco-friendly thermal insulation products with good physical and hygrothermal properties. The currently research work on straw composite thermal insulators commonly use the polyester fibres, synthetic resins and inorganic cementing materials as binders. Few studies work on the fully bio-sourced straw composite thermal insulation materials, in which the straw fibres are bonded by natural adhesives. Moreover, the water solubility and water absorption are seldom reported. The water solubility is an important property need to be investigated as the material can be contacted with water especially in outdoor operation condition. Also, the effect of different factors on the hygrothermal properties of these materials is not comprehensively investigated. Furthermore, the hygrothermal performance of the straw composite thermal insulation is not unknown at wall scale. Therefore, this thesis aims to develop fully bio-sourced straw composite thermal insulation materials for buildings, which are derived from rice straw fibres and natural binders. The hygrothermal properties of the developed composite materials in consideration of

different factors are characterized and evaluated under various experimental tests in both material scale and wall scale.

3. Development and characterization of insulation materials from rice straw and natural binders

3.1. Introduction

The available information of the state of the art has shown the benefits and downsides in the use of agricultural straw for manufacturing new insulation materials in buildings. The compressed straw insulation panels are mainly produced by bonding straws with polyester fibres, synthetic resins and inorganic cementing materials. These binders, however, leads to an increase in embodied energy use and an issue of waste disposal as they are indecomposable.

This chapter aims to develop building insulation materials from rice straw fibres and natural binders with competitive hygrothermal properties. Two natural polysaccharides, i.e., sodium alginate and chitosan can be selected as binders because

they have favourable properties such as being nontoxic, adhesive, biocompatible, biodegradable with low cost. However, insulating composites using sodium alginate as the binder might suffer from water solubility issue considering that sodium alginate is water soluble at ambient condition. Also, there is no scientific data on the durability of insulating composites from natural binders, particularly concerning their water resistance. In the field of food industry, many studied reported that water insoluble films can be obtained by immersing sodium alginate-based films into the calcium ion solution due to the cross-linking reaction to form a water insoluble egg box [115]. Therefore, this chapter attempts to propose a modified method to prepare water insoluble insulators from rice straw and sodium alginate. The modified method is compared to the traditional methods by conducting water solubility test. Moreover, the thermal insulation and moisture properties including the sorption isotherm, water vapor permeability and water absorption of the composite materials are assessed and compared by investigating the influence of fibre size, binder type and binder ratio. Additionally, the mould growth of the composite materials from different binders (i.e., alginate and chitosan) are analysed and compared after exposure to high relative humidity.

3.2. Rice straw

3.2.1. Origin of rice straw

Two types of rice straw fibres (denoted as RS1 and RS2) with different fibre size (Figure 3.1) were provided by FBT isolation (Dagnex, France). The straw fibres are obtained by defibrating the raw materials using an industrial device.

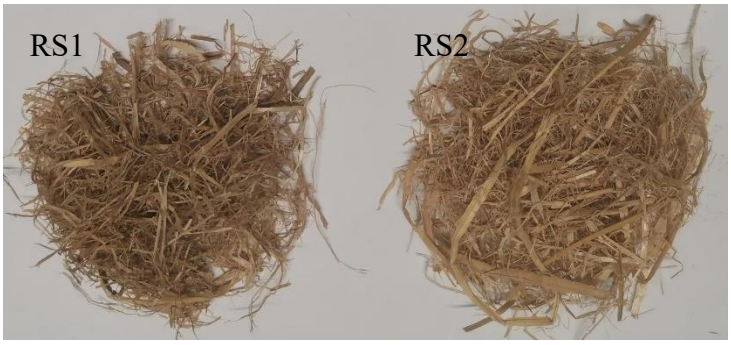

Figure 3.1. Rice straw fibres

3.2.2. Fibre size distribution

Some methods can be used to characterize the fibre size distribution of the rice straw, such as sieving and image analysis [116]. The sieving method separates the fibres into several grades by a series of standard screens with different mesh sizes. After weighing the different screens, the mass fraction of various fibre size can be obtained. This method is simple and easy to operation. However, since the grade division is limited by the number of screens, the accuracy could be affected. The image analysis depends on a software to process the image obtained by a digital camera and further extract the geometric features of the fibres. This method provides more morphological information except for the mass fraction and high calculation efficiency due to the development of software technology. However, in order to have the accurate result, fibres are required not to be touched and overlapped when using the image analysis.

Considering that the fibres investigated in this study have the elongated shape and the fibres are twined, it is very difficult to separate the fibres without touch. Therefore, in this study, the fibre size distribution of the RS1 and the RS2 is determined by the mechanical sieving according to the recommendation of the RILEM TC 236-BBM [117]. The measurements were performed on three 15g samples. The mechanical sieving was processed with normative square opening sieves with the sizes of 32, 16,

8, 4, 2, 1, 0.5 mm. Figure 3.2 shows the fibre size distribution of the RS1 and the RS2. It can be seen that the RS1 had more percentage of small fibres (< 2 mm) compared to the RS2.

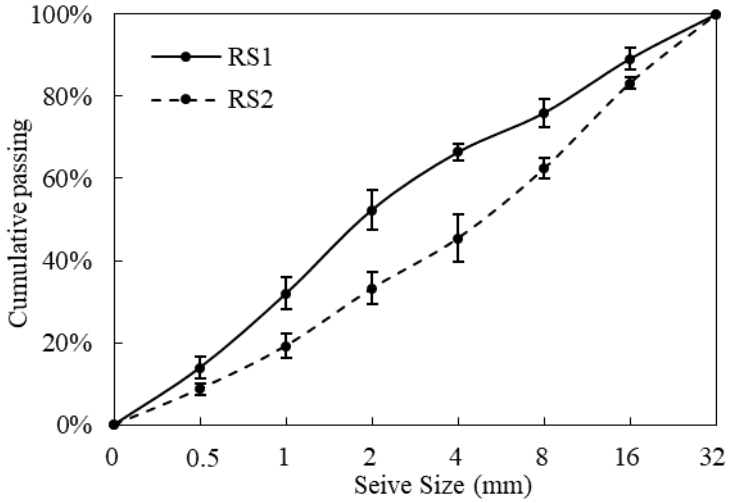

Figure 3.2. Fiber size distribution of RS1 and RS2 (average and standard deviation)

2.3. Binder materials

3.3.1. Sodium alginate

Alginates are unbranched polysaccharides, commonly extracted from brown seaweeds such as Laminaria hyperborean and Ascophyllum. They have been widely and extensively used in the fields of food, medical, paper and cosmetic industries because of their excellent characteristics, such as non-toxicity, biocompatibility and biodegradability as well as their low cost [118].

Alginates consist of two linear copolymeric units of L-guluronic acid (G) and D-mannuronic acid (M) that are linked by α-(1→4) and β-(1→4) glycosidic bonds, respectively (Figure 3.3). For commercial alginates, the relative ratio of each unit denoted as the M/G ratio is varied from 0.5 to 2 [118]. Generally, alginates include three segments, i.e., M-block, G-block and MG-block. M-block only contains the unit of D-

mannuronic acid, while G-block only contains the unit of L-guluronic acid. MG-block contains both the units in a mixed arrangement. The proportions of the different blocks are dependent on the species of seaweeds from which alginates are extracted. This characteristic has an important influence on the properties of alginates. Alginates with high G-block are more rigid, while alginates with MG-block are more flexible.

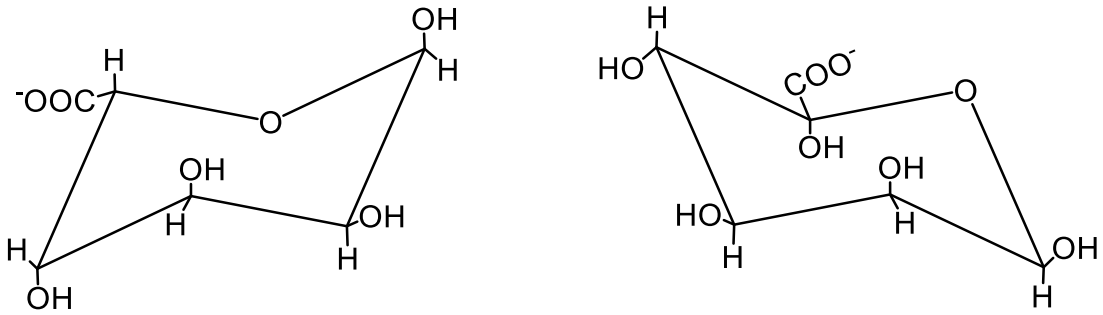

α-(1→4)-linked L-guluronic acid (G) β-(1→4)-linked D-mannuronic acid (M)

Figure 3.3. Chemical structure of alginate and its constituent

Sodium alginate is the most commonly available alginic acid salt. When it is dissolved in aqueous solution, the carboxyl groups are in their ionized state, resulting in a highly viscous aqueous solution. Therefore, it can be used as thickeners, emulsions, suspending agents and stabilizers.

In this study, a commercial sodium alginate with a viscosity of 207, a pH of 7 at 1% aqueous solution was purchased from Algaia^{TM} with the reference number of ALGOGEL 6021. It was solubilized at room temperature under stirring at concentrations ranging between 2% and 7% (w/v). Calcium sulphate ($CaSO_4$), calcium chloride ($CaCl_2$) and sodium citrate were purchased from Glentham Life Sciences (UK).

3.3.1.1. Gel formation

The gelation of sodium alginate happens when multivalent cations (e.g., Ca^{2+}, Zn^{2+}

and Al^{3+}) exist in its aqueous solution. The most widely used crosslinking ion is Ca^{2+} partly due to its mild characteristic and relatively easy to use. The gelation capacity mechanism is dependent on the proportion of G-block. G-block can form the strongest crosslinking points among the three different blocks. The gelling process can be described as the "egg box" model, where the Ca^{2+} are introduced to cavities created by the G-block, forming a structure similar to egg shell [118], as shown in Figure 3.4. The stability of the gel structure is dependent on the amount of the ions and the length of the G-block.

The methods to prepare the gel by Ca^{2+} crosslinking can be categories as the diffusion method and the internal gelation method [119]. The approach of introducing Ca^{2+} is different between these two methods. The diffusion method involves introduction of Ca^{2+} from an external source into the alginate solution, in which the gelation is practically instantaneous. The most commonly used approach is to drop alginate solution droplets into $CaCl_2$ bath. Conversely, the internal gelation method involves mixing the Ca^{2+} with the alginate solution. In this way, organic acids are normally added to control the release rate of the Ca^{2+} ions by lowering pH of solution, allowing to slow down the formation of gels. The most commonly used approach is to introduce the powder of $CaCO_3$ and $CaSO_4$, complexing agents such as gluconolactone and sodium citrate into sodium alginate solution

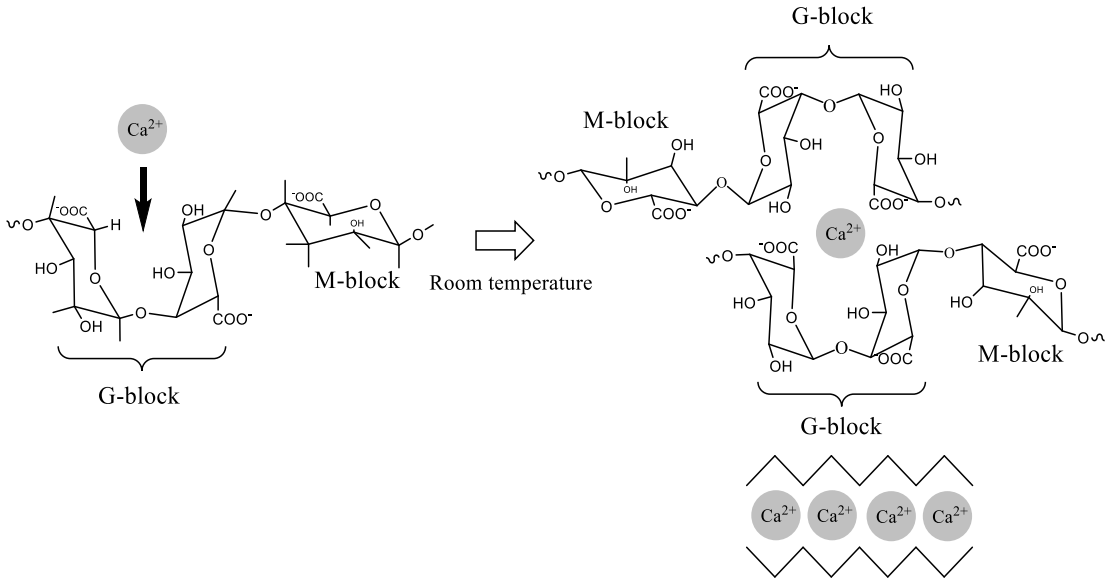

Figure 3.4. Egg box formation by Ca^{2+} crosslinking

3.3.2. Chitosan

Chitosan is a natural polysaccharide, which is acquired by deacetylation of chitin. Chitin is widely existed in the exoskeleton of crustaceans, (e.g., shrimps and insects). Crustacean shells, a waste in food industry, provides an economical origin for the production of chitosan. It has been widely and extensively used in the fields of food, water treatment, biochemical and biomedical industries because of their excellent characteristics, such as non-toxicity, biocompatibility and biodegradability.

Chitin is a copolymer of N-acetyl-D-glucosamine and D-glucosamine units linked by β-(1→4) glycosidic bonds [120]. In the polymeric chain, the N-acetyl-D-glucosamine unit are predominant. In the process of deacetylation, the acetyl group (CH_3CO-) presented in chitin is converted to the hydroxyl (-OH) and amino (-NH_2) groups in the chitosan (Figure 3.5). A unique property of chitosan is the polycationic nature when it is added into the acidic solution, resulting in a viscous solution.

In this chapter, the chitosan was purchased from Glentham Life Sciences (UK) with

the reference number of GP8523. It is produced from shrimp shell with a deacetylation degree of 92%, a viscosity of 65 cps and a pH of 7 at 1% aqueous solution. The chitosan was solubilized at room temperature under stirring at concentration ranging between 2% and 5% (w/v) in acetic acid 1% (v/v).

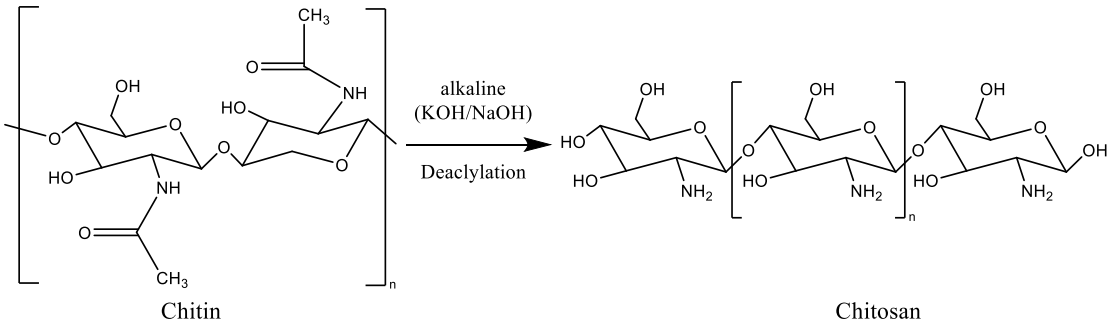

Figure 3.5. Chitin and chitosan after deacetylation

3.4. Manufacture process

3.4.1. Overall approach

The overall manufacture process for obtaining the composites from rice straw fibres and alginate/chitosan is shown in Figures 3.6 and 3.7. Firstly, the adhesive binder was obtained by dissolving alginate/chitosan powder in distilled water under continuous stirring at 250 rpm for 30 min. Then, the rice straw fibres were mixed with adhesive binder using a force-action paddle at 20 rpm for 2 min. Subsequently, the wet mixture was placed into an extruded polystyrene with dimensions of 30×30×4 cm^3 and the whole set was compacted using a weight of 40 kg for 4 h. Finally, the composites were oven-drying at 50 ºC for 65 h in order to accelerate the drying process. Note that for the alginate-based composites, a further process was applied to prevent water-solubility issues, which is introduced in Section 3.4.2.

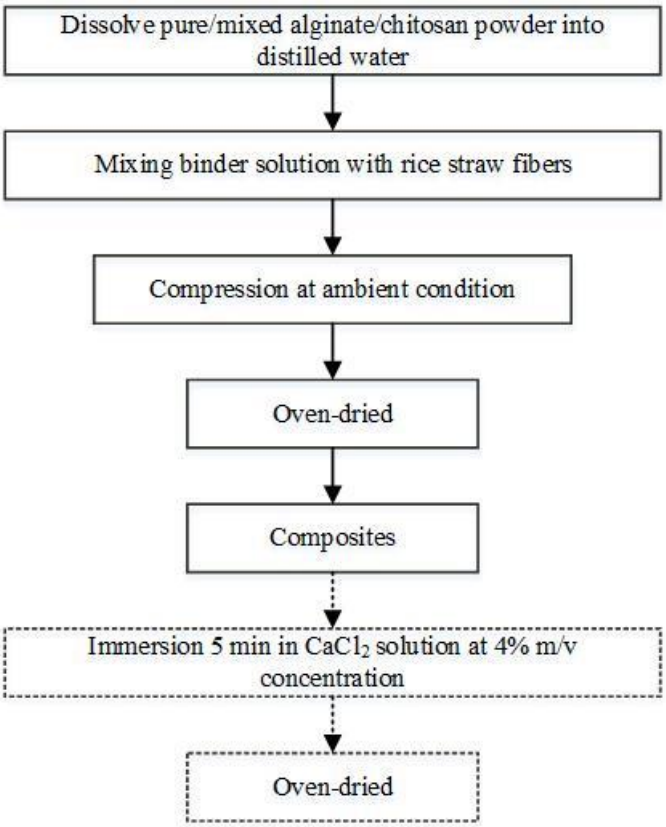

Figure 3.6. Manufacture process of the composites from rice straw fibres and alginate/chitosan

Figure 3.7. Binder solution (left), wet fibres (middle) and compression by weight (right)

3.4.2. Process adaptation to prevent water-solubility issues

Considering that the sodium alginate is water-soluble, insulation materials using the sodium alginate as binder might be destroyed when they are contacted with water

[47, 115]. In order to prevent this issue, a calcium ion crosslinking method was proposed in this study. Specifically, the composite material obtained from sodium alginate was further immersed in $CaCl_2$ solution at concentration of 4% (m/v) for 5 min (Figure 3.8), which is recommended in the work of [115]. The composite material after the immersion was drained for 10 min and then further oven-dried at 50 ºC for 48 h (Figure 3.6).

Figure 3.8. Immersion alginate-based composite in $CaCl_2$ solution

3.5. Board formulation

The influence of fibre size, binder ratio and binder type on the thermal insulation and moisture properties were also investigated. Two types of fibres, i.e., RS1 and RS2 were used. After some preliminary work, three binder ratios, 0.08, 0.16 and 0.24 for alginate-based composites and 0.08, 0.13 and 0.175 for chitosan-based composites were used, respectively. The ratios of the binders with respect to the rice straw fibres were adjusted to obtain composites with enough cohesive to maintain integrity and sufficient solubility of binder powder under the same volume of distilled water. Specifically, the binder ratio of 0.08 was selected as it is used in the rice straw panel available in market. Also, the binder ratio of 0.07 was tried but the obtained straw composite can be teared

by hand. The highest binder ratio of chitosan was 0.175 as the chitosan powder cannot completely dissolved in water if more than this value. The chosen formulations were those depicted in Table 3.1. In order to assess the effectiveness of the proposed crosslinking method for alginate-based composites, a pure sodium alginate (referred as A00) [121] and a mixture of 83 wt% sodium alginate, 15 wt% $CaSO_4$ and 2 wt% sodium citrates (referred as A01) [47] were also used as binders for comparison. Figure 3.9 shows the photos of the composites and the FBT panel.

Table 3.1 Formulation of the rice straw composites

	Binder	Straw type	Binder ratio ($W_{dry\ binder}/W_{straw\ fiber}$)
A00	Alginate	RS2	0.16
A01	Alginate	RS2	0.16
A1	Alginate	RS1	0.08
A2	Alginate	RS1	0.16
A3	Alginate	RS1	0.24
A4	Alginate	RS2	0.08
A5	Alginate	RS2	0.16
A6	Alginate	RS2	0.24
C1	Chitosan	RS1	0.08
C2	Chitosan	RS1	0.13
C3	Chitosan	RS1	0.175
C4	Chitosan	RS2	0.08
C5	Chitosan	RS2	0.13
C6	Chitosan	RS2	0.175

Figure 3.9. Photos of the composites in present study and a panel from FBT isolation

After being processed through compression by weight, the composites were left in an oven to accelerate the drying process. During the drying process, the mass loss revolution was recorded for the chitosan-based composite materials. Figure 3.10 shows that all the composites were completely dried after about 70 h. The composites with higher binder ratio had lower mass loss slope. This is attributed to the fact that the inter-pores in the composite materials can be decreased at the higher solid binder content.

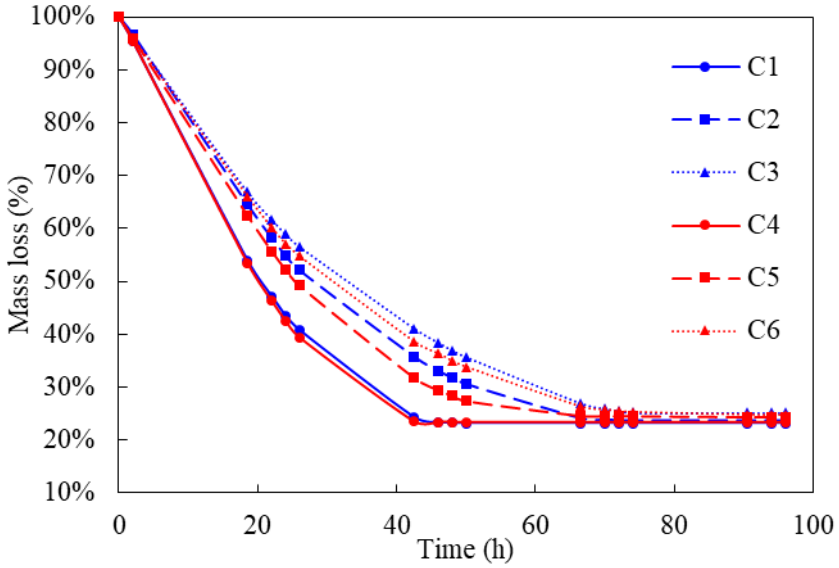

Figure 3.10. Mass loss of the chitosan-based composite materials as a function of time

3.6. Characterization methods

3.6.1. Water solubility

Water solubility test was performed for the formulations of A00, A01 and A5 to evaluate the effectiveness of the crosslinking method proposed in this study. These three composites were immersed in water for 24 h. A camera was used to continuously record the status of the composite samples.

3.6.2. Thermal insulation properties

For the different types of fibres and composites, the thermal conductivity (λ) and thermal effusivity (β) were measured using a FP2C NeoTIM device, equipped with a hot linear wire sensor (50 mm) and a hot plane sensor (50×50 mm^2), respectively, as shown in Figure 3.11. It should be noted that the moisture immigration is limited during the measurement due to the short measurement time (about 5 minute). The thermal conductivity measures the resistance to heat flow across the sample and the thermal effusivity measures the adsorption of the heat on the surface of the sample. Based on the thermal conductivity and the thermal effusivity, the thermal capacity (C_p) was calculated by:

$$C_p = \frac{\beta^2}{\lambda \cdot \rho} \tag{3.1}$$

Where λ (W/(m·K)) is the thermal conductivity; β (W·$s^{1/2}$/(m^2·K)) is the thermal effusivity; ρ is the density of the materials.

All the fibres and composites were measured on the dried state. They were firstly oven-dried at 50 ºC until constant mass was reached and then cooled in a desiccator containing silica gel. Three loose samples were taken from the RS1 and the RS2, and

three pairs of the samples (100 × 100 mm dimension) were taken from each formulation. All the measurements were conducted at room temperature (around 25 ºC).

Figure 3.11. Thermal conductivity and effusivity measurements for fibers and composites

3.6.3. Water vapor permeability

Water vapor permeability of the composites was measured by wet cup according to the standard ISO 12572 [23]. In order to investigate the effect of relative humidity on the permeability as well as the necessity of modelling, the dry cup test was also conducted for the formulations of A5 and C5. Prior to testing, the composite samples were placed in an ambient environment condition (23±5ºC and 50±5% RH) for a long time. They were then attached on Plexiglas cups (with dimensions of 100 × 100 × 60 mm) containing a saturated salt solution (i.e., Potassium sulphate K_2SO_4 providing 97% RH) for wet cup or a desiccant (i.e., silica gel providing 5%RH recorded by a T&RH sensor) for dry cup using silicone. Subsequently, the sides of the samples were sealed with the sides of the cup by using a vapor-tight aluminium tape, as shown in Figure 3.12. The thickness of the air layer (d_a) between the bottom of the samples and the top of the solution or the desiccant was set to 20 mm. The assemblies were finally put in a box containing a saturated salt solution (i.e., Magnesium nitrate hexahydrate

$Mg(NO_3)_2 \cdot 6H_2O$ providing 54% RH). The box was placed in a room with temperature air conditioned at 20 ºC, as shown in Figure 3.13.

During the experiment, the cups were removed once a day during the working week from the box to be weighed using a balance with a precision of 0.01 g. The measurements continued until a steady-state of water vapor transmission flow (five successive determinations of change in mass within 24 h intervals are less than 5% following ISO 12572).

The water vapor transmission flow across the sample G (kg/s) can be expressed as:

$$G = \frac{\Delta m}{\Delta t} \tag{3.2}$$

The water vapor permeability (δ_p) and the water vapor resistance factor (μ) were then determined by:

$$\delta_p = \frac{G \cdot d}{A \cdot \Delta P_v} \tag{3.3}$$

$$\mu = \frac{\delta_a}{\delta_p} \tag{3.4}$$

Where A (m^2) is the exposed surface area of the sample; d (m) is the thickness of the sample; ΔP_v (Pa) is the difference of water vapor pressure at the both sides of the sample; δ_a is the water vapor permeability of air.

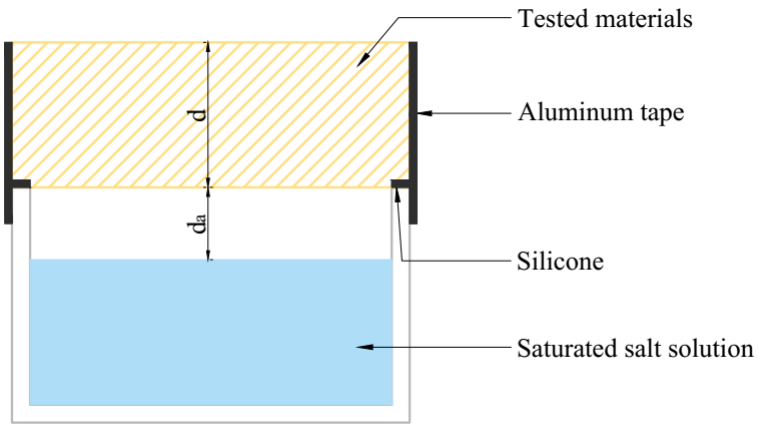

Figure 3.12. Wet cup configuration

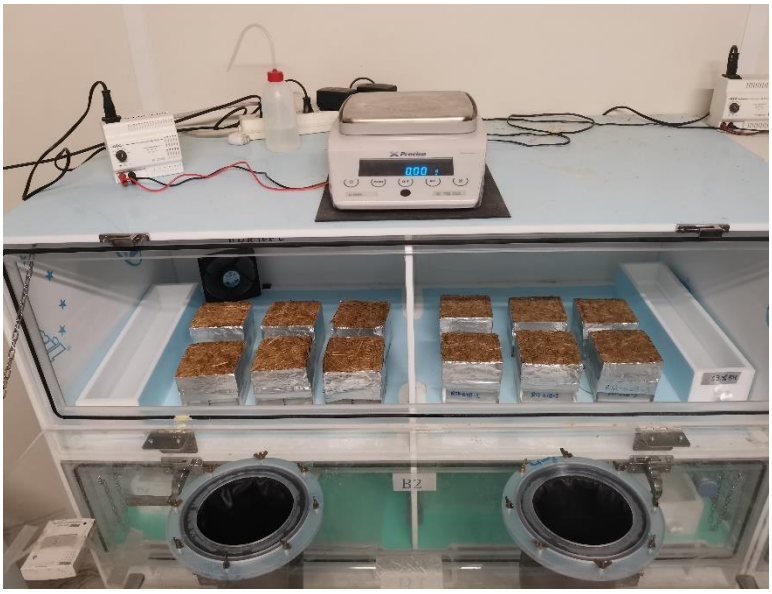

Figure 3.13. Experimetal setup of the water vapor permeability test

3.6.4. Adsorption and desorption isotherms

For a constant temperature, the moisture content of a material is correlated with the surrounding relative humidity. This correlation can be denoted as the adsorption-desorption isotherms, which is a property necessary for modelling the buffering effect of a material. It is also an important factor exerting effect on the resistance to the proliferation of microorganisms.

This study measures the adsorption-desorption isotherms of different types of fibres and composites according to standard EN ISO 12571 using the saturated salt solution method [21]. Measurements were realized on three loose samples for the different types of fibres and three samples (with the dimension of 50 × 50 mm) for the different formulations. Prior to testing, the samples were oven-dried at 50 ºC until constant mass was reached (i.e., the two weighing within 24 h intervals are less than 0.1%). The samples were then placed in sealed boxes containing different saturated salt solutions. The salts were selected according to their availability and the recommendations of EN ISO 12571 (using at least five salt solutions providing 9%-93% RH). Table 3.2 shows the six salt solutions and their theoretical values of relative humidity and uncertainty employed in this study. The actual values of relative humidity were measured using the HOBO HD35EDG sensor and HOBOU12-012 sensor (Figure 3.14) in order to test the tightness of the box. The vapor-tight boxes were placed in a room with the temperature air-conditioned at 20 ºC, as shown in Figure 3.15. The tested samples were regularly weekly weighed until constant mass was reached for each relative humidity levels from low to high. Subsequently, the samples were placed in the box providing 85% RH until mass stabilization. It is then decreased from 85% RH to lower relative humidity levels to trace the desorption curve.

The equilibrium moisture content of the samples was calculated by:

$$u = \frac{m - m_0}{m_0} \tag{3.5}$$

Where m (kg) is the mass of the samples at different relative humidity; and m_0 (kg) is the mass of the dried samples.

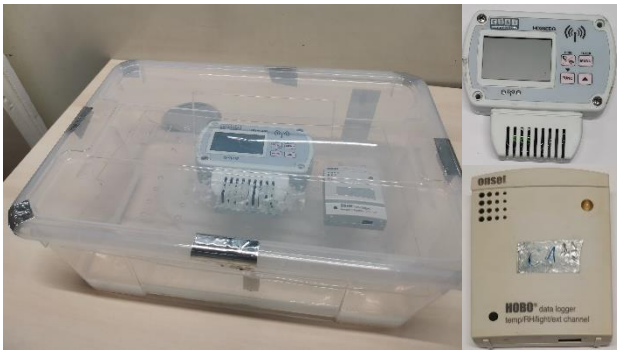

Figure 3.14. HOBO sensors for measuring the relative humidity in the salt box

Figure 3.15. Experimental setup for the saturated salt solution method

Table 3.2 The theoretical values of relative humidity provide by different salt solutions at 20 ºC

Relative humidity	Salt
11.31 ± 0.31	Lithium chloride (LiCl)
22.51 ± 0.32	Potassium acetate (CH_3COOK)
43.16 ± 0.33	Potassium carbonate (K_2CO_3)
58.20 ± 0.42	Sodium Borimide (NaBr)
75.47 ± 0.14	Sodium chloride (NaCl)
85.11 ± 0.29	Potassium chloride (KCl)

3.6.5. Ideal moisture buffer value

The moisture buffer value (MBV) is the amount of water vapor transported across a material under the changes of water vapor pressure in the surrounding air during a period of time. The theoretical moisture buffer value (MBV_{ideal}) of a material can be denoted as a function of water vapor permeability and moisture storage capacity. In the work of [93], the theoretical moisture buffer was found to be close to the experimental moisture buffer value. In this study, the theoretical moisture buffer value was calculated by the equations in the Nordtest report [100].

The moisture effusivity b_m ($kgm^{-2}Pa^{-1}s^{-1/2}$)) was determined by:

$$b_m = \sqrt{\frac{\delta \cdot \rho_d \xi}{P_{sat}}} \tag{3.6}$$

Where δ (kg/(m·s·Pa)) is water vapor permeability; ρ_d (kg/m^3) is the dry density of the material; P_{sat} (Pa) is the saturated water vapor pressure at T=20 ºC; and ξ is the moisture sorption capacity (kg/kg). The saturated water vapor pressure can be expressed as a function of temperature:

$$p_{sat} = 610.5 \cdot e^{\frac{17.269 \cdot \theta}{237.3+\theta}} \tag{3.7}$$

The moisture sorption capacity was acquired from the experiment results of sorption isotherm. According to the Nordtest report [100], it can be expressed as the slope of the sorption curve for the relative humidity between 33%RH and 75%R, as follows:

$$\xi = \frac{\partial u}{\partial rh} \tag{3.8}$$

Where u (kg/kg) is the moisture content and rh is the relative humidity (-).

Finally, the MBV_{ideal} can be calculated by:

$$MBV_{ideal} = 0.00568 \cdot p_{sat} b_m \sqrt{t_p} \quad (3.9)$$

Where t_p (s) is the time period (24 h).

3.6.6. Water absorption

Water absorption of the composites was determined by partially immersing the samples in water with their bottom face (10 mm) below the water level following the standard EN 1609 [122] for different intervals (i.e., 1 h, 2 h, 4 h, 6 h, 24 h, 48 h and 76 h). Measurements were realized on the three samples (with the dimensions of 100 × 100 mm) for each formulation. The samples were removed from the water at specified intervals and then drained for 2 min to remove the excess water before weighing the samples (Figure 3.16). The water absorption can be determined by

$$\text{Water absorption (\%)} = \frac{w_i - w_d}{w_i} \quad (3.10)$$

Where w_i is the mass of the samples after immersion in water at different time and w_d is the mass of the dried samples.

Figure 3.16. Water absorption test

3.6.7. Mould growth

Due to the organic structure of straw, mould can be grown on the straw-based materials under extreme environmental conditions, eventually leading to material decomposition and performance degradation. Mould growth require moisture for the growth on the material surface and thus materials with high moisture storage capacity supports mould growth. In this study, the mould growth of the composites from alginate and chitosan were investigated by exposing to high relative humidity levels at 20 ºC. Two relative humidity levels (including 93% RH and 97% RH) were applied and the mould growth on the surface of the composites were captured by visual inspection with a camera.

3.7. Results and discussion

3.7.1. Water solubility

The water solubility was measured for the composites A00, A01 and A5 to assess the effectiveness of the modification method proposed for the alginate-based composites. Figure 3.17 shows the status of the three composites after different immersion time (i.e., 1 min, 1 h and 24 h) as well as the composites' integrity after immersion in water for 24 h.

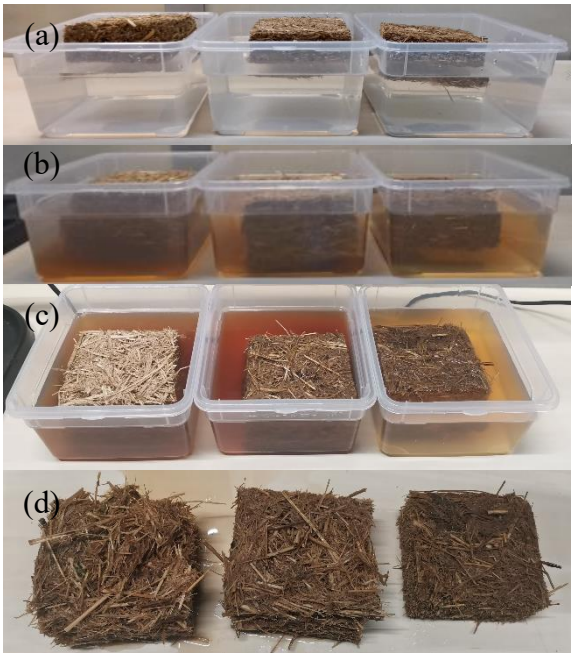

Figure 3.17. From left to right: A00, A01 and A5 immersed in water for (a) 1 min; (b) 1 h; (c) 24 h and (d) after 24h

As shown in Figure 3.18 (a) and (b), the thickness of the composites A00 and A01 increased significantly more than that of the composite A5 after 1 h. This result demonstrates that the composites A00 and A01 swelled more in water and became looser than the composite A5. It can also be observed from Figure 3.18 (b) and (c) that the water colour was light yellow for the composite A5, while the water colour became red for the composites A00 and A01. A possible explanation for this might be that the yellow pigments within rice straw diffused into water for the three composites and the alginate component was partly dissolved in water for the composites A00 and A01. When the three composites were taken out of water after 24 h, the composite A5 was complete, while the composites A00 and A01 were partly destroyed. Therefore, it can be concluded that the proposed crosslinking method is able to prevent the water solubility issue of the insulation materials using sodium alginate as a binder.

3.7.2. Thermal insulation properties

Table 3.3 shows the summary of the density, the thermal conductivity, the thermal effusivity and the deduced mass specific heat capacity of the two types of fibres and twelve composites with different fibre type, binder type and binder ratio. It should be noted that the thermal and moisture properties of A00 and A01 were not measured because they failed in the water solubility test.

Table 3.3 Density and thermal conductivity of the different types of fibres and different composites

Materials	Density ρ (kg/m^3)	Thermal conductivity λ (W/(m·K))	Thermal effusivity ($W.s^{1/2}/(m^2·K)$))	Heat capacity (J/(kg·K))
RS1	43 ± 2	0.035 ± 0.001	54 ± 2	1900
RS2	39 ± 1	0.034 ± 0.001	55 ± 2	2293
A1	132 ± 1	0.041 ± 0.001	85 ± 2	1352
A2	142 ± 3	0.045 ± 0.001	88 ± 1	1221
A3	162 ± 9	0.047 ± 0.003	93 ± 2	1140
A4	104 ± 3	0.038 ± 0.001	75 ± 2	1428
A5	124 ± 5	0.042 ± 0.001	84 ± 3	1353
A6	135 ± 5	0.043 ± 0.002	84 ± 4	1212
C1	115 ± 5	0.041 ± 0.002	79 ± 4	1311
C2	143 ± 2	0.044 ± 0.001	84 ± 2	1115
C3	144 ± 8	0.045 ± 0.001	83 ± 2	1072
C4	100 ± 3	0.038 ± 0.002	74 ± 1	1459
C5	121 ± 4	0.042 ± 0.001	83 ± 2	1375
C6	133 ± 8	0.043 ± 0.002	81 ± 1	1175

When the thermal conductivity of a material is lower than 0.1 W/(m·K), the material can be regarded as insulating [123]. Therefore, the composites obtained in this study can be considered as insulators with thermal conductivity values ranging between 0.038 and 0.047 W/(m·K). In comparison with other environmentally friendly

insulating materials such as wood fibres/textile waste insulation boards (0.078-0.089 W/(m·K)) [47], rape straw concrete (0.094 W/(m·K)) [124] and corn cob insulation boards (0.13-0.15 W/(m·K)) [125], the composites in this study have competitive insulation properties. They have thermal conductivity values close to commercially available bio-based insulation products such as hemp insulation (0.038-0.043 W/(m·K)) [126] and the non-bio-based insulation products such as rock wool (0.036 W/(m·K)) and expanded polystyrene (0.038 W/(m·K)) [127].

Figure 3.18 (a) and (b) show the influence of fibre type and binder ratio on the thermal conductivity of the alginate-based composites and the chitosan-based composites, respectively. It can be seen that the composites from RS1 had the higher thermal conductivity than the composites from RS2. This result indicates that the thermal conductivity of the composites can be increased when employing the smaller fibre size. For example, the average thermal conductivity values of the composites A1, A2 and A3 from RS1 were higher by 8%, 7% and 9% compared to the composites A3, A4 and A6 from RS2, respectively (Table 3.3). Also, increasing the binder ratio increased the thermal conductivity of the composites. For example, the average thermal conductivity values increased by approximately 13% (from 0.038 to 0.043 W/(m·K)) when the binder ratio increased from 8% to 17.5% for the composites from RS2 and chitosan (Table 3.3). These results can be explained by the smaller porosity values of the composites given the smaller fibre size and larger binder ratio.

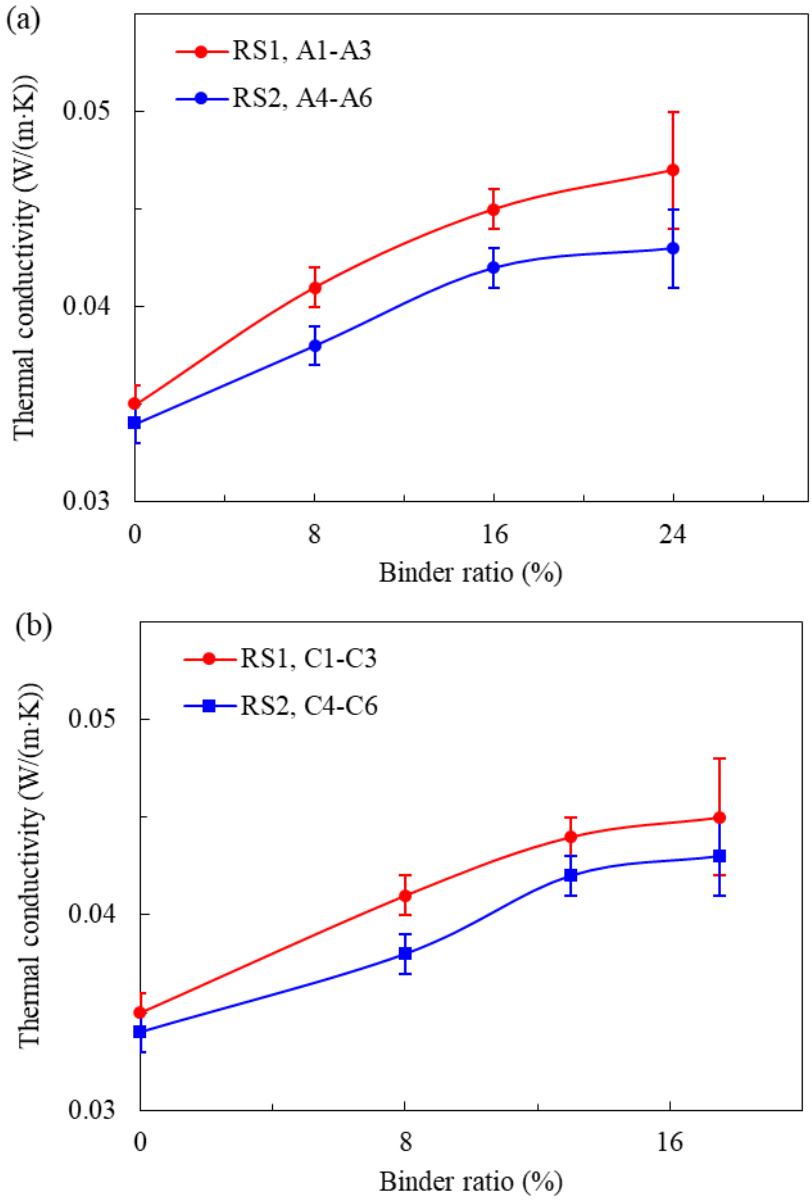

Figure 3.18. Thermal conductivity of the compsoites from (a) alginate and (b) chitosan

The thermal conductivity values of the straw composites in present study and in literature are plotted versus their dry densities in Figure 3.19. All the materials from literature are also straw-based. They are straw bale [55] and straw composites produced by bonding straws with starch [45, 95], liquid glass [46, 92] and lime [44].Overall, the thermal conductivity of the straw insulation materials seems to be lineally increased with their density. By comparing with the state-of-art straw composites with the same

density values ranging between 100 and 160 kg/m^3, the developed composites still have competitive insulation properties.

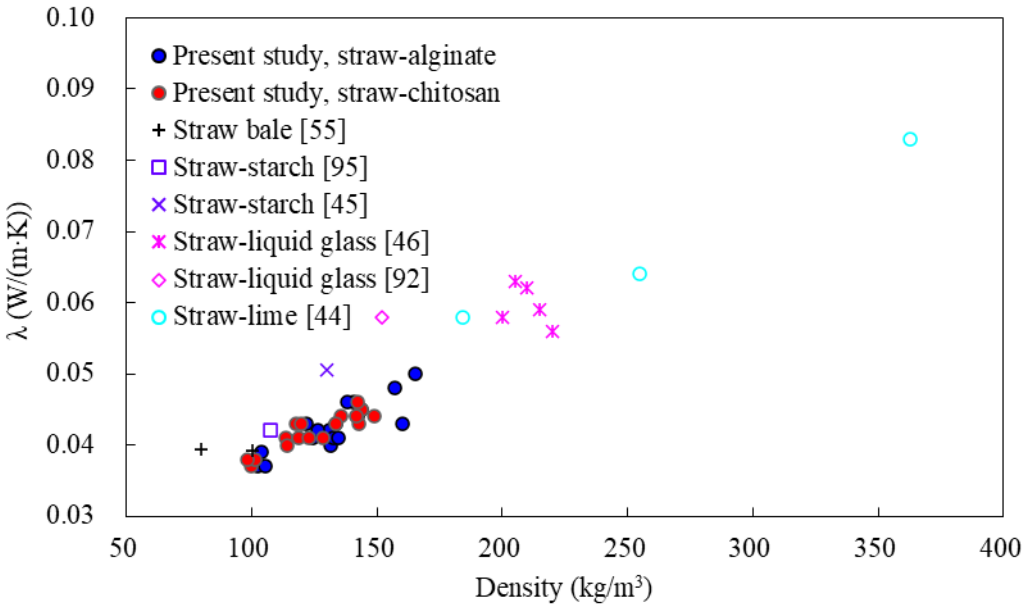

Figure 3.19. Thermal conductivity vs density in present study and in literature

3.7.3. Water vapor permeability

Table 3.4 Vapor permeability and vapor resistance factor of the composites

Materials	Wet (30% mean RH)		Dry (75% RH)	
	$\delta \times 10^{-11}$ (kg/(m·s·Ps))	μ (-)	$\delta \times 10^{-11}$ (kg//(m·s·Ps))	μ (-)
A1	6.4 ± 0.1	3.1 ± 0.1	-	-
A2	6.0 ± 0.2	3.3 ± 0.1	-	-
A3	5.1 ± 0.4	3.9 ± 0.3	-	-
A4	7.5 ± 0.5	2.7 ± 0.2	-	-
A5	6.5 ± 0.1	3.1 ± 0.1	3.4 ± 0.2	5.8 ± 0.3
A6	6.0 ± 0.5	3.3 ± 0.2	-	-
C1	5.2 ± 0.1	3.8 ± 0.1	-	-
C2	4.0 ± 0.1	5.0 ± 0.2	-	-
C3	3.7 ± 0.2	5.3 ± 0.2	-	-
C4	5.9 ± 0.2	3.4 ± 0.2	-	-
C5	5.4 ± 0.2	3.7 ± 0.1	3.3 ± 0.8	6.0 ± 0.2
C6	4.5 ± 0.1	4.4 ± 0.1	-	-

The water vapor permeability (δ) and the water vapor resistance factor (μ) are deduced for each formulation, as shown in Table 3.4. The water vapor permeability of air is assumed to be $1.98 \cdot 10^{-10}$ kg/(m·s·Pa). The μ values by wet cup is used for comparison. The μ values were in the range of 2.7-5.3. They are quite close to the values of straw insulation materials using starch and liquid glass as binder, which are 3.4 [46] and 2.6 [92] (also measured by wet cup) with the dry density of 108 kg/m^3 and 152 kg/m^3, respectively. Similar values can also be found in rock wool, glass wool and wood fibreboard [127].

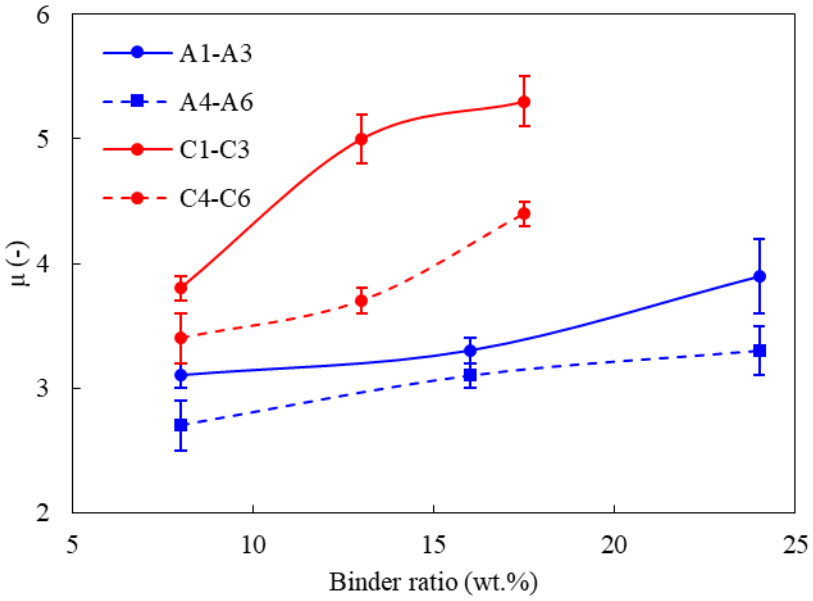

Figure 3.20. Vapor resistance factor of the composites

The μ values are shown in Figure 3.20. It can be seen that the chitosan-based composites had the higher μ values compared to the alginate-based composites. The μ values were ranging from 3.4 to 5.3 for the chitosan-based composites and ranging from 2.7 to 3.9 for the alginate-based composites, respectively (Table 3.4). An increase of μ value was observed after increasing the binder ratio. For example, the μ value was increased by approximately 29% (from 3.4 to 4.4) when increasing the binder ratio from 8% to 17.5% for the composites from chitosan and RS2 (Table 3.4). Moreover, the

composites from RS1 presented the higher μ values compared to the composites from RS2, indicating that a decrease in fibre size resulted in an increase in the μ values.

Table 3.5 Fitting coefficients of water vapor permeability

Materials	a_δ	b_δ
A5	1.33	6.89
C5	1.90	4.67

The results of the dry cup for the composites A5 and C5 are also shown in Table 3.4. As it can be seen, the μ values of both the A5 and C5 obtained by dry cup were higher than those obtained by wet cup. This can be attributed to the liquid water transfer across the composites happened in the wet cup test, leading to the higher moisture transportation compared to the dry cup test. Moreover, the δ values of the composites A5 and C5 are represented as a function of relative humidity. Considering that only two average relative humidity is applied in this study, the fitting equation was simplified to a linear fitting, i.e., $\delta = a_\delta + b_\delta rh$) The fitting parameters are presented in Table 3.5.

3.7.4. Sorption isotherm

The adsorption-desorption isotherm curves were measured and compared for the studied rice straw fibres, alginate-based composites and chitosan-based composites. The moisture content denoted in Figure 3.21 represents the ratio of water mass to dry mass. For convenience, the two types of fibres (i.e., RS1 and RS2) and the six formulated composites were investigated. The chosen six formulations A3, A5, A6, C3, C5, C6, are representative in order to study the influence of fibre type, binder type and binder ratio on the adsorption-desorption isotherm curves of the composites

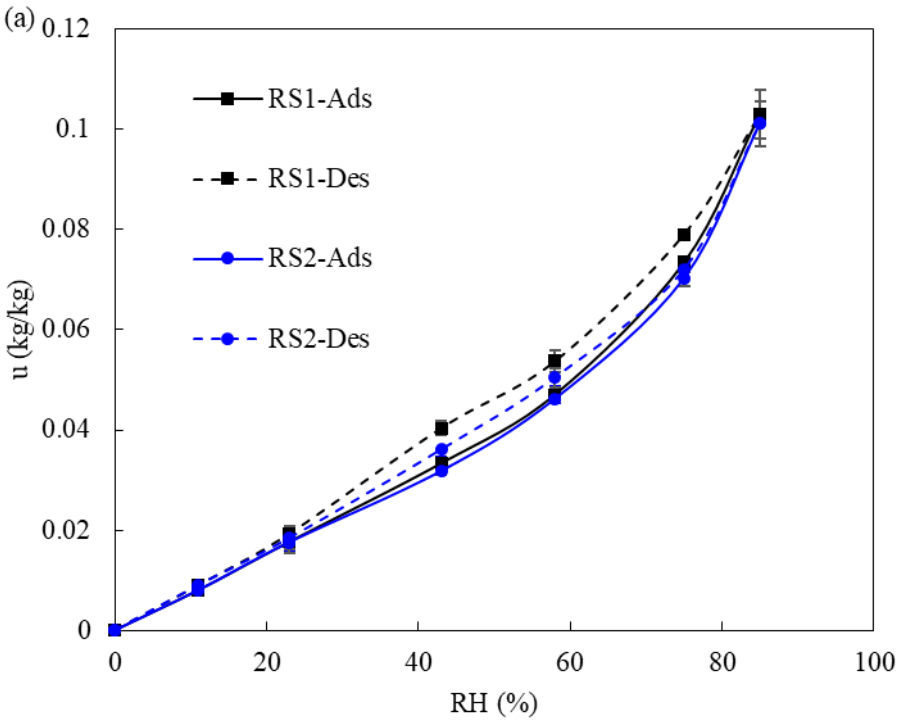
(a)
RS1-Ads
RS1-Des
RS2-Ads
RS2-Des
u (kg/kg)
RH (%)
0
0.02
0.04
0.06
0.08
0.1
0.12
0
20
40
60
80
100

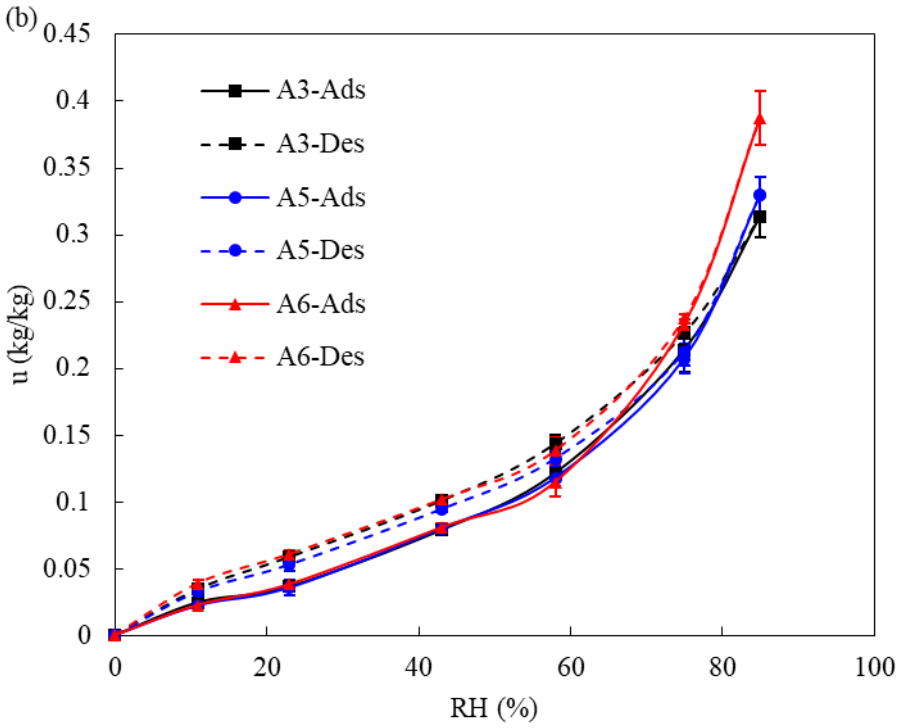
(b)
A3-Ads
A3-Des
A5-Ads
A5-Des
A6-Ads
A6-Des
u (kg/kg)
RH (%)
0
0.05
0.1
0.15
0.2
0.25
0.3
0.35
0.4
0.45
0
20
40
60
80
100

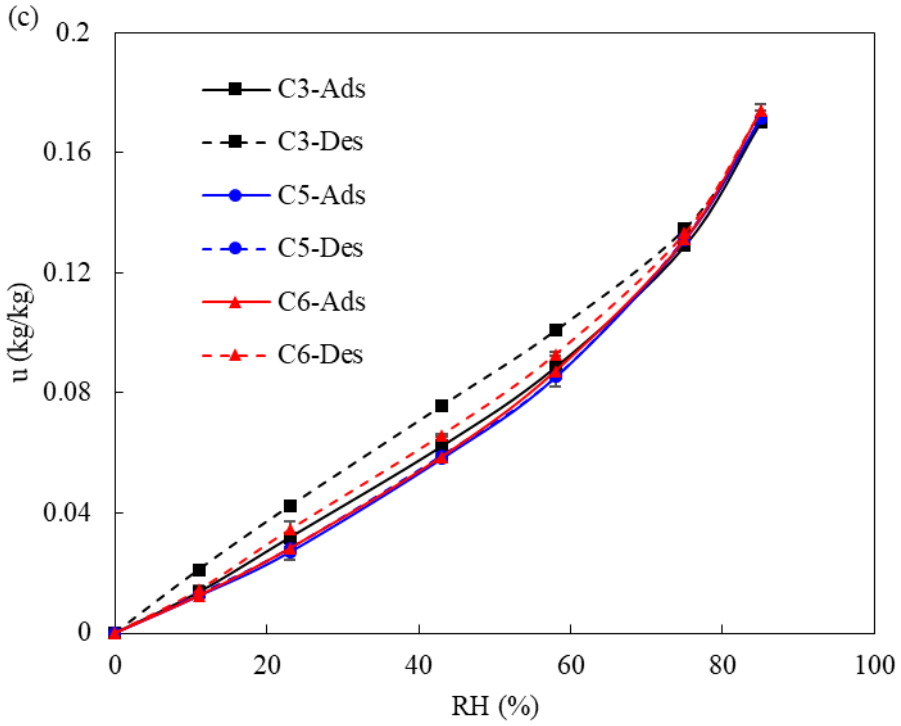

Figure 3.21. Adsorption-desorption isotherms of the studied (a) rice straw, (b) alginate-based composites, (c) chitosan-based composites

In accordance with the IUPAC classification [128], all the curves can be categories into type II. The moisture content was strongly increased at higher relative humidity as the capillary condensation probably occurred. Moreover, the hysteresis between the adsorption isotherm curve and the desorption isotherm curve can also be seen in Figure 3.21 for all the fibres and the composites. This is a common phenomenon for cellulosic materials, which can be explained by the ink bottle effect.

As shown in Figure 3.21, the moisture storage capacity of the composites can be largely influenced by the binder type. Specifically, for the same relative humidity, the alginate-based composites had the higher moisture content at equilibrium compared to the chitosan-based composites. For example, the alginate-based composites had the moisture content of over 30% at 85%RH, while the chitosan-based composites had the moisture content of below 20% at 85%RH. This result indicates that the water

sensitivity of the composites can be reduced by replacing the alginate binder by chitosan. However, the fibre type and binder ratio have negligible effect on the adsorption-desorption isotherm curve of the composites studied. Similar behaviour can also be seen between the RS1 and RS2.

In addition, Guggenheim-Anderson-de Boer (GAB) model was applied to fit the adsorption-desorption curve of the composites A5 and C5. The GAB model can be expressed as[129]:

$$u = \frac{M \cdot C \cdot K \varphi}{(1 - K \cdot \varphi)(1 - K \cdot \varphi + C \cdot K \cdot \varphi)} \tag{3.11}$$

Where u (kg/kg) is mass moisture content of the material at equilibrium state; φ is the relative humidity (-); M, C and K are the fitting parameters.

Figure 3.22 shows the experimental points and GAB fits for the A5 and C5. The experimental points of the sorption isotherms are the average values of the adsorption isotherm and desorption isotherm. It can be seen that the model precisely produced the sorption isotherms. The GAB parameters for the composites A5 and C5 are provided in Table 3.6. The composite A5 had the higher value of K, indicating the higher entropy and liquid state, while the composite C5 had the higher value of M, indicating the more active sites for monolayer moisture sorption.

Table 3.6 GAB parameters of the sorption isotherm curve for A5 and C5

Materials	GAB parameters		
	M	C	K
A5	0.0647	4.8146	0.9560
C5	0.0825	1.9228	0.7425

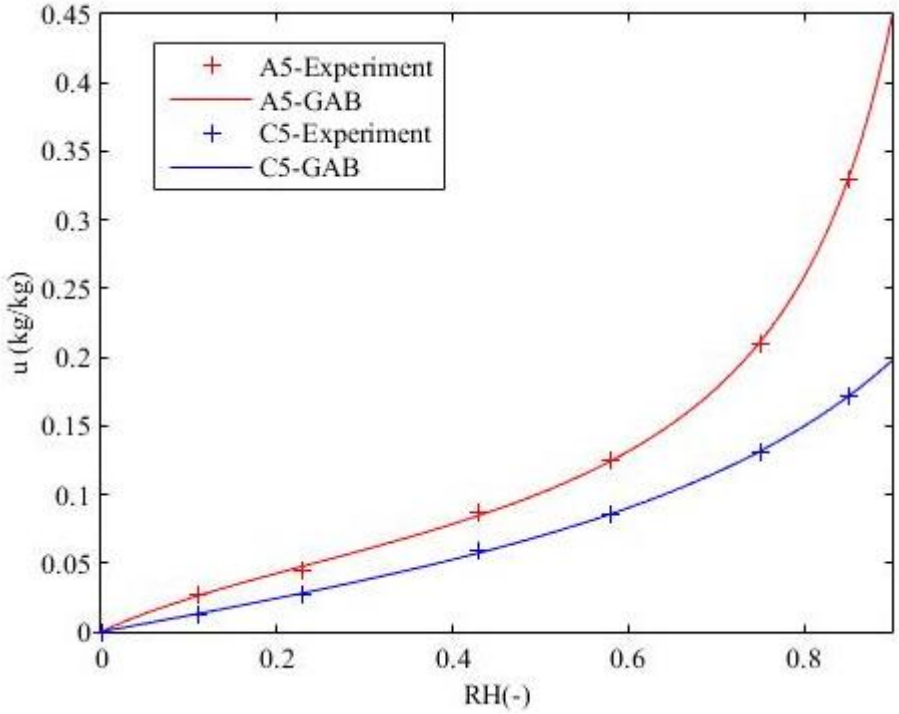

Figure 3.22. Sorption isotherms of A5 and C5 and GAB fits

3.7.5. Ideal moisture buffer value

Despite of the theoretical values, the MBV_{ideal} is useful to compared the buffer ability of the different composites in this study. The MBV_{ideal} of the different composite materials are presented in Table 3.7.

Table 3.7 Calculated dynamic properties

Composites	ξ (kg/kg)	b_{m_wet} (kg·(m²·Pa·s$^{1/2}$))	b_{m_dry}	MBV_{ideal_wet} (g·m^{-2}·%RH^{-1})	MBV_{ideal_dry} (g·m^{-2}·%RH^{-1})
A3	0.3603	1.13E-06	-	4.4	-
A5	0.3430	1.09E-06	7.89E-07	4.2	3.1
A6	0.3920	1.17E-06	-	4.6	-
C3	0.1879	6.57E-07	-	2.6	
C5	0.2032	7.48E-07	6.74E-07	2.9	2.3
C6	0.2101	7.33E-07	-	2.9	-

In accordance with the Nordtest project [100], all the composite materials showed an "excellent" buffering efficiency (Table 3.7). For comparison of the MBV_{ideal} of different formulations, the water vapor permeability measured with the wet cup was used although the relative humidity between 54% and 97% was much higher than the actual condition. The alginate-based composites had the higher MBV_{ideal} than the chitosan-based composites. The MBV_{ideal} of the composites from alginate and chitosan were from 4.2 to 4.6 and from 2.6 to 2.9. A very small difference of value (the maximum value is about 0.4 for alginate and 0.3 for chitosan) can be observed for different fibre size and binder ratio. This is consistent with the results of steady state hygric properties, i.e., water vapor permeability and adsorption-desorption isotherms. When the water vapor permeability by dry cup was used, the MBV_{ideal} of the composites A5 and C5 were 3.1 and 2.3, respectively. These values were much lower than the values calculated from the water vapor permeability by wet cup.

3.7.6. Water absorption

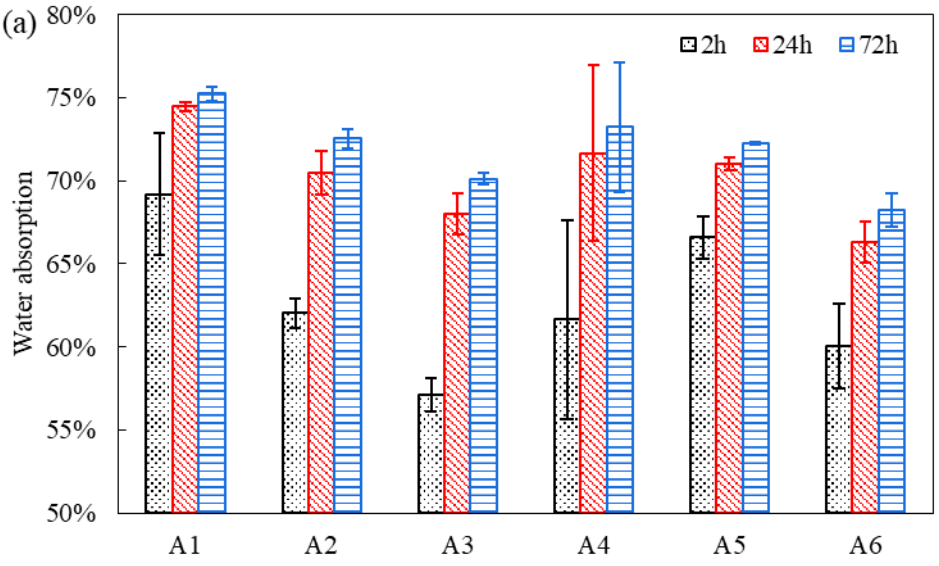

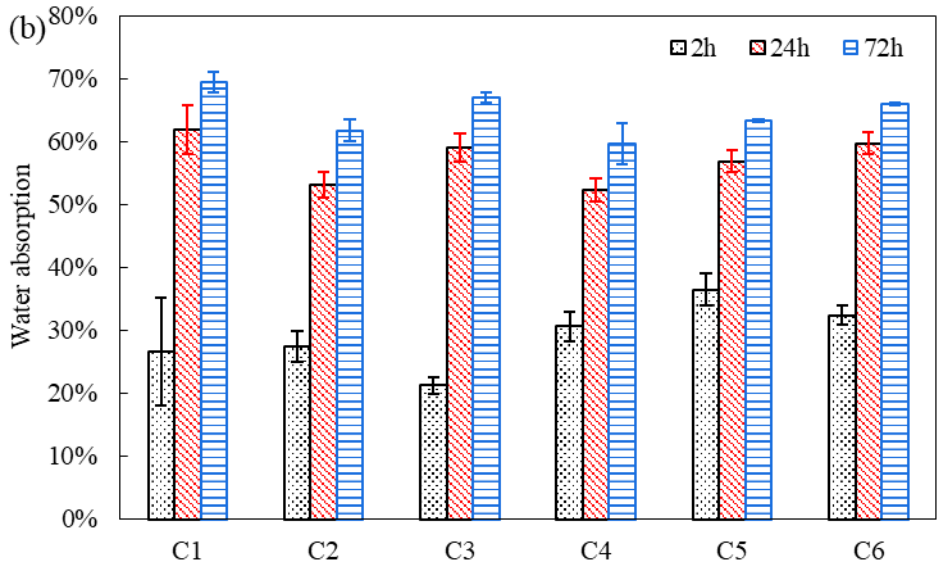

Figure 3.23. Water absorption of the composites from: (a) alginate, (b) chitosan at different immersion time (i.e., 1, 24 and 72 h)

Figure 3.23 presents the water absorption of the composites after different immersion time. The water absorption increased as immersion time increased for all the composites. However, the increasing rate varied between the alginate-based composites and chitosan-based composites. In particular, the alginate-based composites required less time to reach the saturation compared to the chitosan-based composites. For example, after 2 h of immersion, the alginate-based composites had the water absorption between 53% and 69%, while the chitosan-based composites had the water absorption between 21% and 36%. Moreover, the alginate-based composites showed the higher water absorption than the chitosan-based composites. After 24 h of immersion, the alginate-based composites had the water absorption between 66% and 74%, while the chitosan-based composites had the water absorption between 52% and 62%. However, the fibre type and binder ratio have negligible effect on the water absorption of the composites studied.

3.7.7. Mould growth

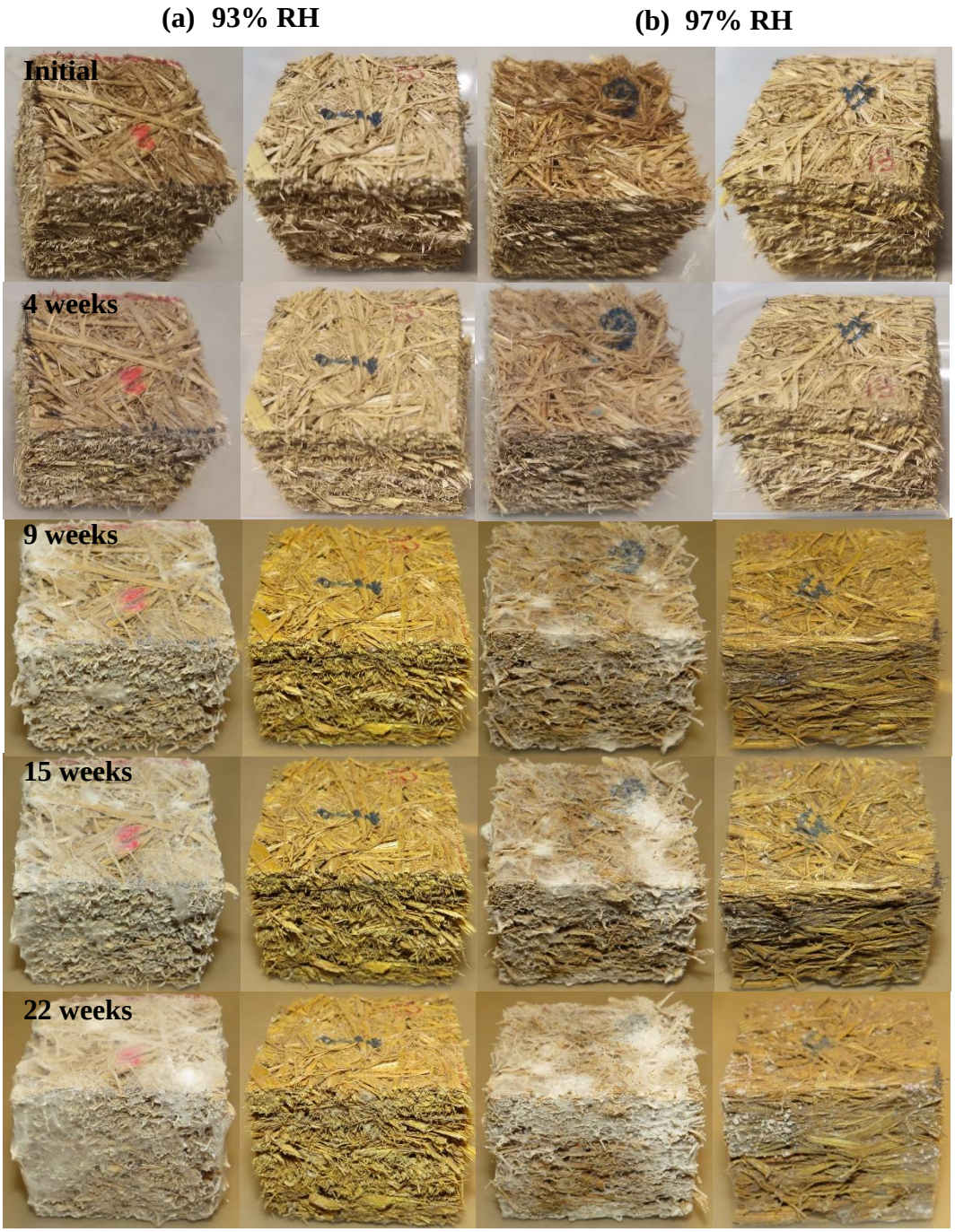

Figure 3.24. Mold appearance on the surface of composites at (a) 93%RH, (b) 97% RH and 20 ºC: C5 (left) and A5 (right) on the week 0, 4, 6 and 8

In this study, the mould growth of the composites A5 and C5 were studied to evaluate the effect of binder type on the durability of the composite material. Figure 3.24 presents the pictures of the composites A5 and C5 at several times during the test period. The visual inspection showed that during the test, the composite A5 had the more affected surface compared to the composite C5. First mould mainly appeared on the composite A5 between the third weeks and the fourth weeks, while it appeared on the composite C5 between the eighth weeks and the ninth weeks. The green, yellow and white colours of mould existed in the surface of the composite A5, while only green and yellow colours of mould existed in the surface of the composites C5. This result indicates that more kinds of mould are contaminated in the surface of the composite A5 than the composite C5. Moreover, more mould can be observed under the moist environment of 97%RH than 93%. This can be explained by the fact that more moisture content can be absorbed in the composites at higher relative humidity, and consequently mould grows more easily and quickly.

3.8. Conclusions

This study developed novel bio-sourced building insulating materials from rice straw fibre and natural binders, i.e., sodium alginate and chitosan. As we know, this is the first time to use the sodium alginate and chitosan as binder for rice straw fibres. A crosslinking method was proposed to prevent the water-soluble issue of the composite material using sodium alginate as the binder. The thermal insulation and moisture properties of the developed composites were investigated by considering the influence of fibre size, binder type and binder ratio. From the experimental results, the conclusions have been drawn as follows:

- The proposed crosslinking method was able to prevent the water solubility issue of

the insulation materials using sodium alginate as a binder.

- All the composites can be considered as insulators with thermal conductivity values ranging from 0.038 to 0.047 W/(m·K) at dry state. A decrease of fibre size and an increase of binder ratio resulted in an increase in the thermal conductivity of the composites. Moreover, the thermal conductivity of these composites showed a lower range of values when compared to existing straw insulating building materials.

- The water vapor resistance factor of the composites from chitosan showed the higher values than those of composites form alginate. Smaller fibre size and larger binder ratio also resulted in higher water vapor resistance factors.

- Binders, even though in small amount, had an influence on the sorption isotherm and water absorption. The alginate-based composites had the higher moisture sorption capacity than the chitosan-based composites. However, the fibre type and binder ratio seem to have negligible influence on the materials' adsorption capacity in this study.

- The binder type and the relative humidity had the impacts on the types, amount and speed of mould contaminated on the surface of the composites.

4. Experimental study hygrothermal performance of rice straw alginate insulation panel

4.1. Introduction

As shown in Chapter 3, the formulation of A5, i.e., rice straw alginate insulation material with type of RS2 and binder ratio of 0.16 had promising properties, such as low density, low thermal conductivity and high moisture storage capacity. Consequently, it was chosen to be investigated on hygrothermal behaviour at wall scale. The objective of this chapter is to study the hygrothermal behaviour of a singer layer wall panel subjecting to different boundary conditions including isothermal, non-isothermal and dynamic conditions. Heat and moisture coupling effect in the wall panel will be analysed and discussed.

4.2. Experimental setup

4.2.1. Facility

An experimental facility, which was designed in the work of [130, 131] at the CETHIL-INSA LYON, was used in this study to simulate different boundary conditions, as shown in Figures 4.1 and 4.2. The facility consists of two compartments between which the wall was clamped. The dimensions of each compartment are 1m of long, 1m of height and 0.5 m of thick. The temperature of compartment 1 is regulated by heat exchanges connected to a crythermostat, while the temperature of compartment 2 is regulated by a climate chamber in remote mode. The relative humidity of the two compartments is regulated using salt solution and desiccant. The exchange surface area of the salt solution and desiccant are approximately 0.46×0.3 m^2. Fans are installed at a height of 20 cm from the salt solution and the desiccant to homogenize the air conditions in each compartment.

Figure 4.1. Actual view of experimental set-up at CETHIL-INSA LYON laboratory

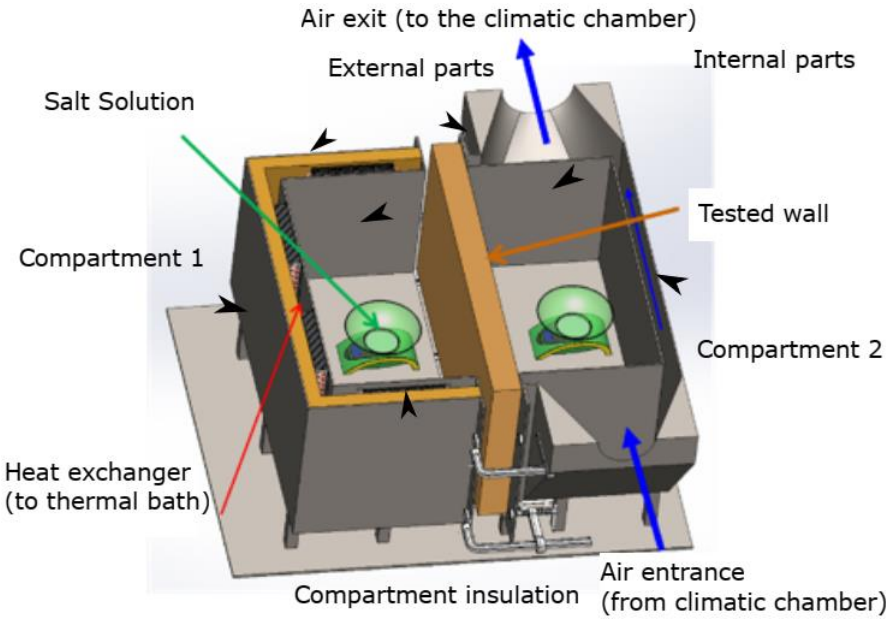

Figure 4.2. Schematic diagram of the bi-climatic configuration

The design and composition of the regulation systems for these two compartments are different. Compartment 1 is composed of an external stainless-steel compartment, a 60 mm layer of polystyrene insulation, four heat exchangers connected to the cryothermostat and an internal stainless-steel compartment with a volume of 0.5 m^3 offering a surface of exchange of 1 m^2 from external to internal. Compartment 2 is composed of a 240 mm multi-layer thin insulation, two 40 mm layers of hemp wool insulation, an external stain-less compartment linked to a climate chamber with glass wool insulated ducts and an internal stain-less compartment with a volume of 0.5 m^3 from external to internal.

The cryothemosat with the type Proline RP 1840 C from the manufacturer LAUDA, has a suction and pressure pump with 8 selectable flow rates and an interface RS-232 allowing remote control. This cryothermostat has a good stability at ±0.01 ºC at a range

between -40 ºC and +200 ºC. It has a heating power of 3.5 kW and a cryogenic capacity of 900 W. Moreover, the cryothermostat allows for internal and external regulations based on temperature measured by a PT100 sensor installed inside the cryothermostat and inside the compartment respectively. This study utilized the internal regulation to control temperature in the compartment 1. The climate chamber (CTS, Clima Temperature System) connected to the compartment 2, allows for generating desired temperature and relative humidity. It contains a capacitive probe for measuring relative humidity and a PT100 probe for temperature measurement. The CTS is also equipped with a control interface on the front panel and an Ethernet-type PC link, making it possible for implementation via software. In this experimental study, the relative humidity controller is not used in CTS and the desired relative humidity in both compartments is achieved by a salt solution and a desiccant.

4.2.2. Measurement techniques

In this study, SHT75 sensors from Sensirion, Switzerland, were used to measure both the temperature and relative humidity in the two compartments and in the wall. The Pt100 platinum probes with a DIN 1/3 tolerance class were utilized to monitor the air temperature in the two compartments. The Type T thermocouples from Chromel-Alumel were used to measure the temperature of internal surfaces of compartments.

The SHT75 consists of a band-gap sensor to measure temperature and a capacitive sensor to measure relative humidity together. The sensor has a small size of 3.1 mm×5.08 mm×19.5 mm, making it suitable to be placed in the wall to avoid disturbing the environment. The accuracy of temperature given by the manufacturer is ±0.5 ºC for the range from 5 ºC to 45 ºC. The accuracy of relative humidity given by the manufacturer is ±2% for the range from 10% to 90%. Also, numerous scientific studies demonstrated the good stability of SHT75 over time and their short response time [132,

133]. Two Pt100 probes were installed in the centre of the two compartments at the height of 0.5m. The measurement uncertainty of these probes is ±0.15 ºC from 5 ºC to 45 ºC. The Type T thermocouples allow temperature measurement with a good precision and stability over time even with high humidity or in the presence of hydrating salts. Moreover, by choosing fine wires with 0.2 mm of diameter of single-strand conductors, the thermocouples have a low disturbance on environment. Table 4.1 shows the metrological characteristics of the sensors provided by the manufacturer.

Table 4.1 Metrological characteristics of the sensors

Sensor	Parameter	Range	Accuracy
SHT75	Temperature	5-45 ºC	0.5 ºC
	Relative humidity	10-90 %	2%
Pt100	Temperature	5-45 ºC	0.15 ºC
Thermocouple	Temperature	5-45 ºC	0.16 ºC

The SHT75 sensors are connected to Arduino to transmit the temperature and relative humidity data over the serial interface (Figure 4.3). The acquisition and recording of the measurements from other sensors, e.g., Pt100 and thermal couples is achieved by an acquisition system, placed in an electrical cabinet. The acquisition system includes a NI cRIO-9074 controller connected to internet and different acquisition modules (Figure 4.3). The 2 Pt100 are connected to the module NI 9217 and 16 thermocouples are connected to the module NI 9214. All the data are transmitted to InfluDB, which is an open-source time series database. The acquisition and visualization of these data is achieved via Grafana, as shown in Figure 4.4.

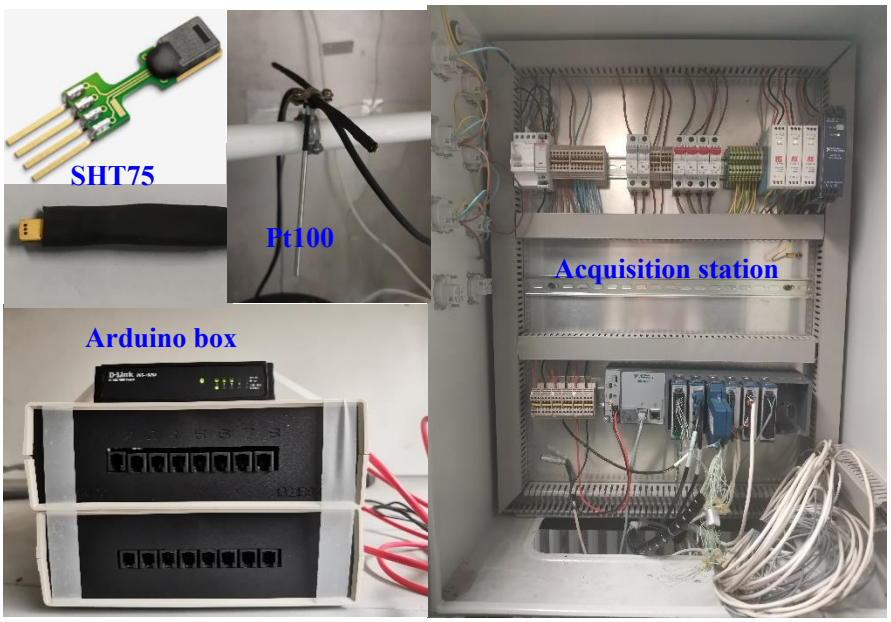

Figure 4.3. Photos of sensors, Arduino box and acquisition station

Figure 4.4. Visualization of data through Grafana: temperature and relative humidity profiles (top), SHT75 values (middle) and Pt100 values (bottom)

4.3. Experimental protocol

4.3.1. Test wall

The test wall is a single layer of the rice straw alginate insulation material with the formulation of A5 mentioned in Chapter 3. The manufacture process of the wall has already been introduced in Chapter 3. It consists in mixing the sodium alginate solution with rice straw fibres in mechanical mixer. The wet fibres were then placed into a polyester mould with the size of 500mm × 500mm × 80mm. The whole mould was placed in an oven to accelerate the drying process and the sample was removed from the mould after mass stabilization. The sample was then immersed in Calcium Chloride solution for 5min for crosslinking and then oven-dried again.

In order to guarantee one dimensional heat and moisture transfer through the direction of thickness, the wall was surrounded by a wood fibre insulation and vapor resistant silicon and PVC films. Specifically, the wall was placed into the core of a wood fibre insulation with the dimension of 1000mm × 1000mm × 80mm (Figure 4.5). Silicone was used to attach the wall on the inter edge of the wood fibre insulation. Vapor-resistant PVC film and aluminium film were used to seal the wood fibre insulation to avoid water vapor transfer around the tested wall.

Figure 4.5. Whole assembly of the tested wall

4.3.2. Sensor location

The wall was arranged with five SHT75 sensors to monitor the temperature and relative changes, as shown in Figure 4.6. Also, a Pt100 and three SHT75 sensors were homogenously placed in each compartment to monitor the air temperature and relative humidity. A special process was carried out to place the sensors inside the wall panel. Boreholes in the desired position were carefully prepared and then the sensors with wires were put into the positions, as shown in Figure 4.7. Finally, silicon was used to seal the bore. Note that the sensors are 45º inclined to the vertical plane to reduce the disturbance of measurements. Considering the uncertainty of boreholes, the exact positions of the SHT75 sensors through the thickness of the wall were finally measured by destroying the wall after finishing all the experiment tests. In this study,

compartment 1 refers to internal environment and compartment 2 refers to external environment. The obtained positions were 28 mm, 36 mm and 64 mm from the interior to the exterior of the wall.

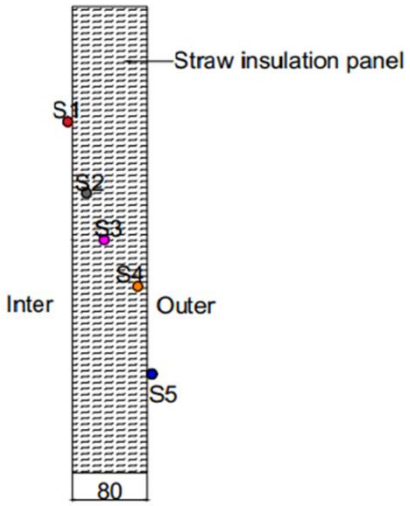

Figure 4.6. The sensor locations in the tested wall

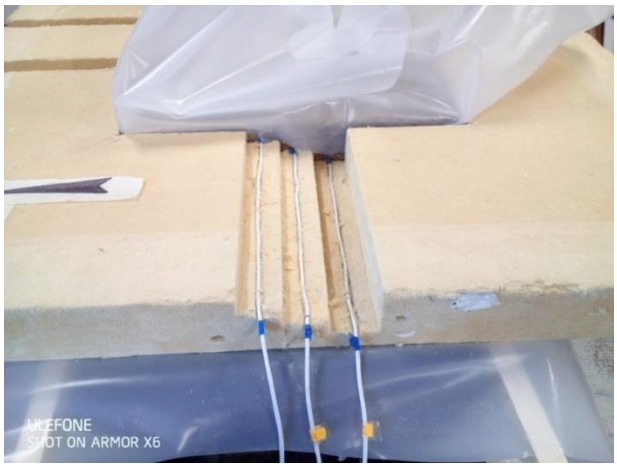

Figure 4.7. Sensor installation within the tested wall

4.3.3. Boundary conditions

According to our knowledge, there are no standard or specifications on scenarios to study the hygrothermal behaviour of bio-sourced materials at wall scale. In this experiment, three types of boundary conditions were applied, i.e., isothermal, non-

isothermal and dynamic conditions. For each test, constant relative humidity in both the compartments was achieved by a saturated salt solution and a desiccant. Specifically, the internal relative humidity was maintained by a saturated salt solution. i.e., Potassium Chloride (KCl). The external relative humidity was controlled by a desiccant, i.e., Calcium Chloride ($CaCl_2$). Before each test, the wall was preconditioned in room conditions until stabilization.

In the isothermal scenario, the temperature in both the compartments were set to 25 ºC for 4 days. Since the temperature gradient is eliminated, this experiment allows to analyse the influence of moisture transport and moisture sorption on the thermal behaviour of the wall. In the non-isothermal scenario, the internal temperature was set to 25 ºC and the external temperature was set to 5 ºC and the test lasted for 2 days. It should be noted that the direction of temperature, vapor pressure and moisture content gradient are from internal to side to external side. This experiment allows to analyse the impact of temperature gradient on moisture transport of the wall. In the dynamic scenario, the internal temperature was set to 25 ºC, while the external temperature was fluctuated from 5 ºC to 15 ºC with amplitude of 10 ºC for a cycle of 24 h. The test lasted for 4 days. The experimental results allow to analyse the hygrothermal behaviour of the insulation material subjected to dynamic condition. Figure 4.8 gives a view of the experiment.

Figure 4.8. Experiment view

4.4. Results and discussion

4.4.1. Isothermal condition

Figure 4.9 shows the measured 4-day internal and external air conditions under isothermal conditions. The experimental results showed a good stability in both the temperature and relative humidity. For the last 24 h, the internal temperature was 25.2±0.1 ºC and the external temperature was 24.9±0.1 ºC. The internal relative humidity stabilized at 81±0.1%. The external relative humidity was controlled by a desiccant ($CaCl_2$), which was less stable compared to the usage of salt solution. In particular, the external relative humidity firstly decreased rapidly and then increased to a nearly fixed value, i.e., 39% with a standard deviation of 0.3%. The average vapor

pressure difference calculated by temperature (ºC) and relative humidity (%) was 13.6 hPa (see Eq. 4.1) and the direction of vapor flow was from internal to external.

$$P_v = RH/100 \times Exp\left(\frac{17.26 \times T}{237.5+T}\right) \quad (4.1)$$

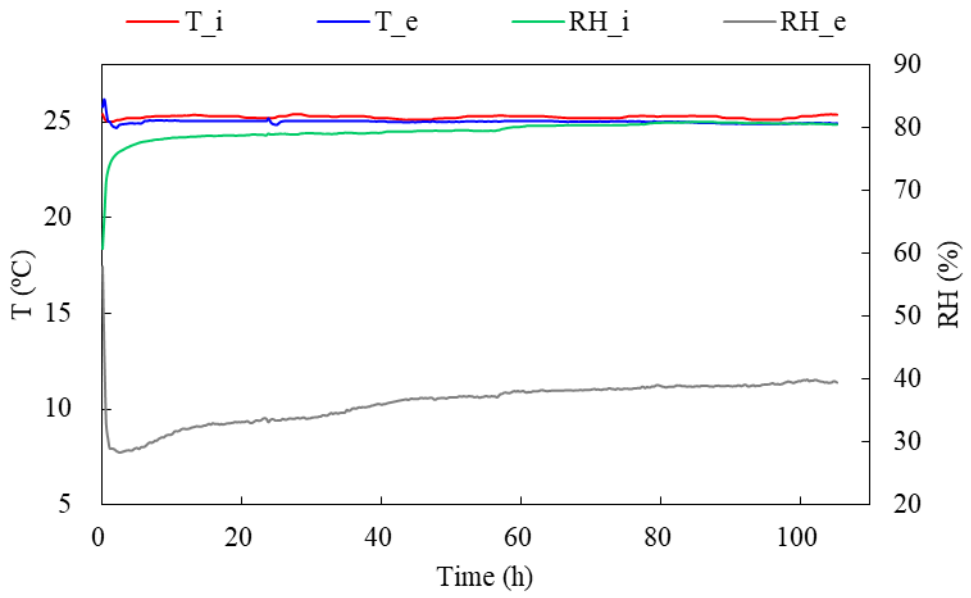

Figure 4.9. The internal and external air conditions under isothermal condition

The changes of relative humidity, vapor pressure and temperature at different depths of the wall were analysed under isothermal conditions, as shown in Figures 4.10-4.12. The initial mean temperature and relative humidity within the wall were 25.6 ºC and 58%. As shown in Figure 4.10 and 4.11, both the relative humidity and vapor pressure increased at the depths of 28 mm and 36 mm and decreased at the depth of 64 mm from internal to external. After 2 days, values of relative humidity were 71%, 65% and 43% at the depths of 28 mm, 36 mm and 64 mm, respectively.

Although the internal and external temperature remained constant at 25 ºC, an increase in temperature of almost 1.4 ºC and 0.7 ºC can be observed at the depths of 28 mm and 36mm respectively, while a sharp decrease in temperature of about 3.2 ºC can

be observed at the depth of 64 mm (Figure 4.12). The exothermic phenomenon occurred as internal air relative humidity was suddenly raised from 58% to 81%. More moisture was absorbed by the material, resulting in condensation and heat release. The larger amplitudes of temperature rose at the depths of 28 mm than 36 mm can be attributed to the more important moisture transport, as indicated in Figure 4.10. The endothermic phenomenon occurred as external air relative humidity was suddenly decreased. For the position near to the external condition, the liquid water evaporated accompanied by heat absorption and consequently the material was cooled down. Therefore, it can be concluded that moisture transport exerts an important effect on thermal behaviour of the wall.

After the stabilization, a small temperature gradient can still be observed. Nevertheless, its effect on moisture transport can be ignored because the temperature gradient was only 0.6 ºC. Moreover, the temperature was still fluctuated after stabilization. This can be explained by the local interaction between fibres and the inter-pores.

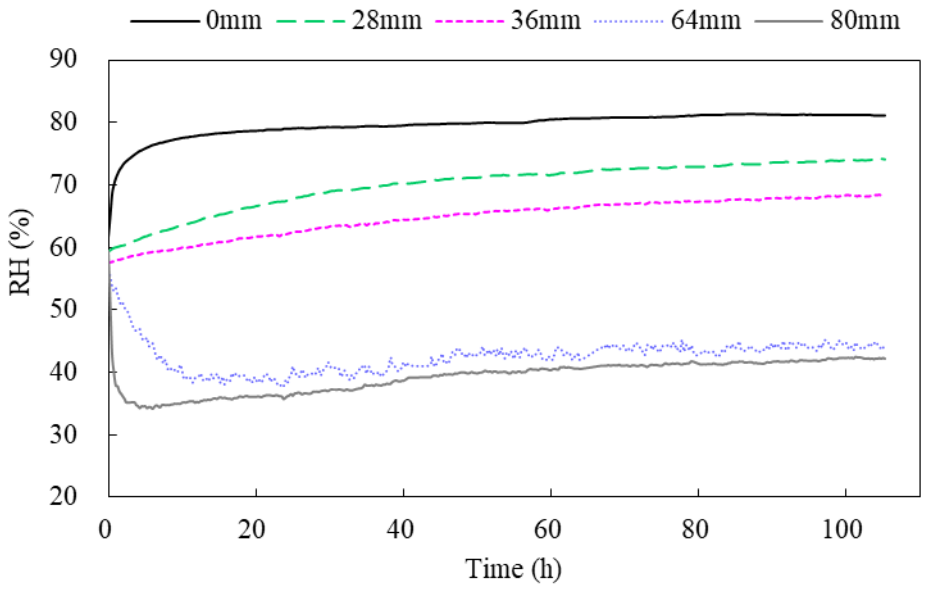

Figure 4.10. Relative humidity changes at different depths of the wall under isothermal condition

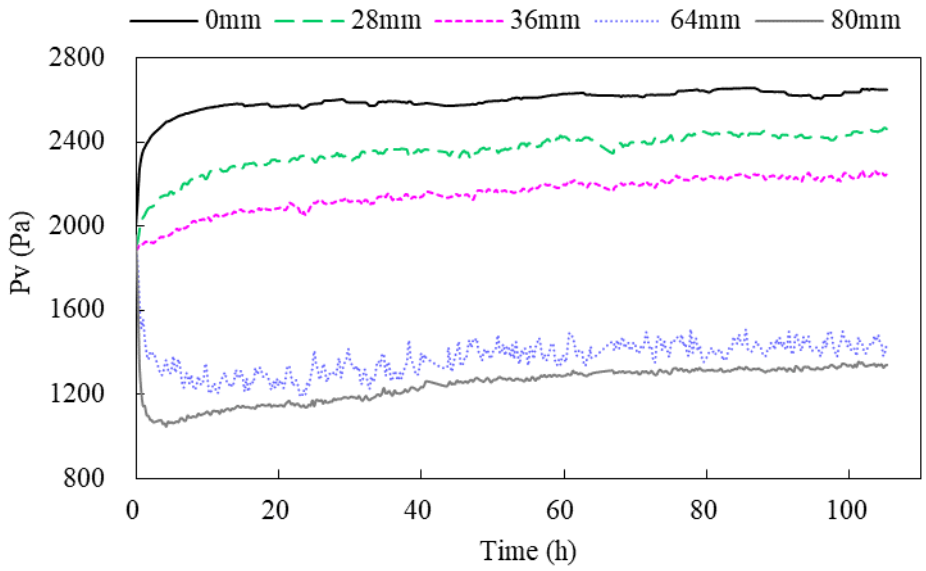

Figure 4.11. Vapor pressure changes at different depths of the wall under isothermal condition

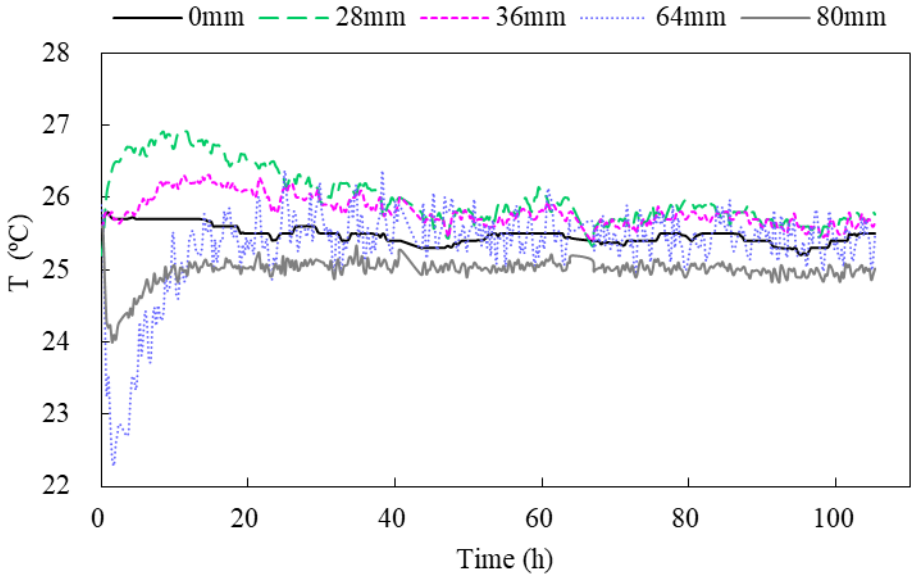

Figure 4.12. Temperature changes at different depths of the wall under isothermal condition

Assuming the local equilibrium in the material, the moisture content profiles over time can be tracked by the relative humidity profiles and the sorption isotherm obtained in Chapter 3, as shown in Figure 4.13. As it can be seen, the moisture flux direction was from the interior side to the exterior side. It can also be seen that the moisture was

absorbed at the depths of 28 mm and 36 mm leading to the heat release at these locations, while the moisture was desorbed at the depth of 65 mm leading to the heat adsorption at this position. The approximate linear curve after 96 h indicated that the moisture transport tended to approximate steady state.

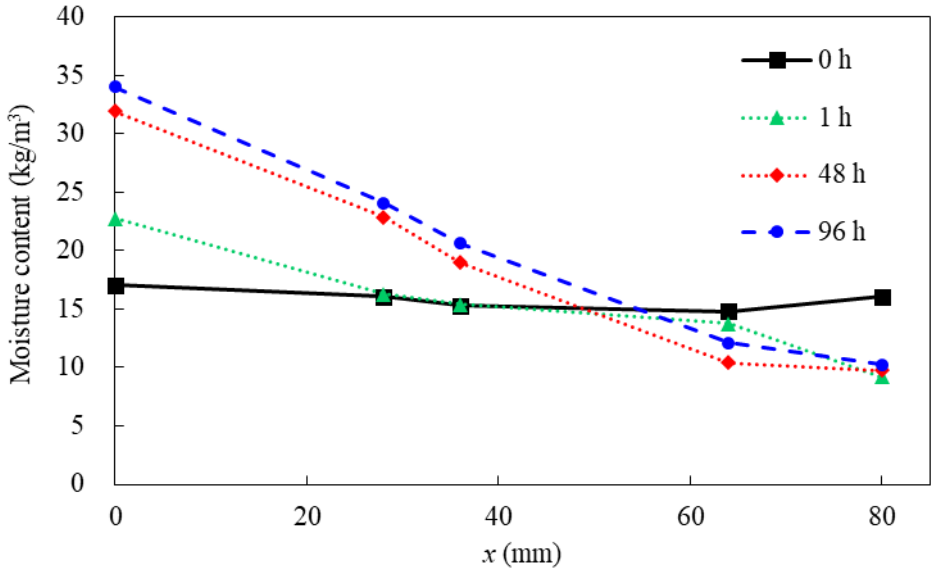

Figure 4.13. Moisture content profiles in the wall after 0 h, 1 h, 48 h and 96 h under the isothermal condition

For evaluating the status of moisture storage or moisture release, the change of moisture content in the wall was calculated as follows:

$$m_{abs/des}(t) = \int \Delta w \cdot A \cdot dx \tag{4.2}$$

Where Δw (kg/m^3) the moisture content changes, A (m^2) is the surface area of the wall panel, x (m) is the thickness.

Based on the Eq. (4.2), Figure 4.14 shows the estimated mass change of the wall. The amount of water stored in the wall is about 94g.

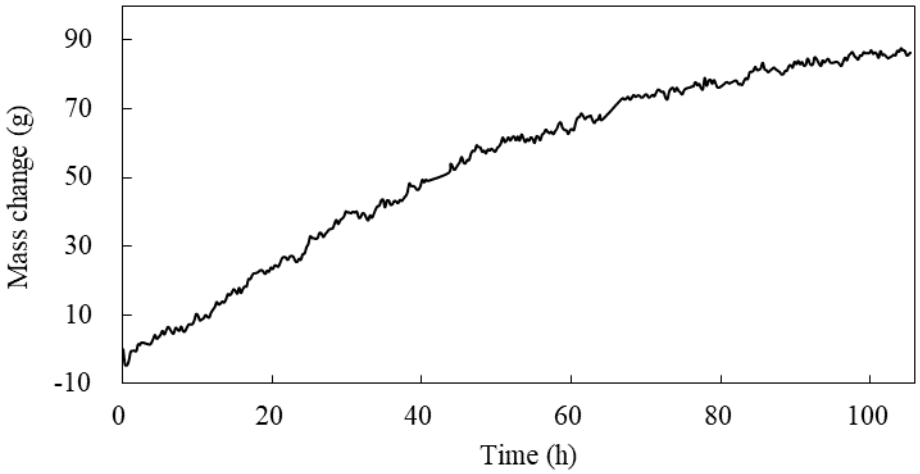

Figure 4.14. Moisture content stored in the wall under isothermal condition

4.4.2. Non-isothermal condition

Figure 4.15 shows the measured 2-day internal and external air conditions under non-isothermal conditions. For the last 24 h, the internal temperature was 24±0.1 ºC and the external temperature was 7±0.2 ºC. The internal relative humidity stabilized at 81±0.1% and external relative humidity stabilized at 53±0.5%.

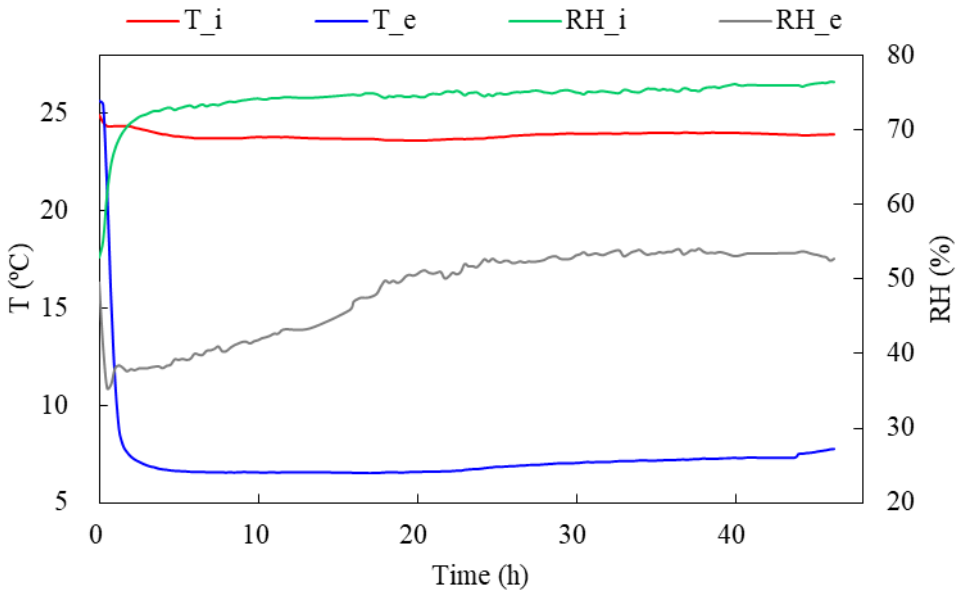

Figure 4.15. The internal and external air conditions under non-isothermal condition

The temperature, relative humidity and vapor pressure changes at various depths of the wall for the non-isothermal test are presented in Figures 4.16-4.18. Regarding to the thermal behaviour, it can be seen that there is a temperature gradient, leading to a heat flux from internal side to external side. When compared to the hygric response under isothermal condition, the thermal response under non-isothermal condition was much faster. Moreover, the temperature at the depth of 64 mm reached the steady state faster compared to the other 2 locations. The vapor gradient induced a vapor flux from interior to exterior surface of the wall. Compared to the isothermal test, the vapor gradient between the interior surface and the first position (i.e., 28 mm) is larger. This indicated that the moisture transport can be affected by temperature gradient.

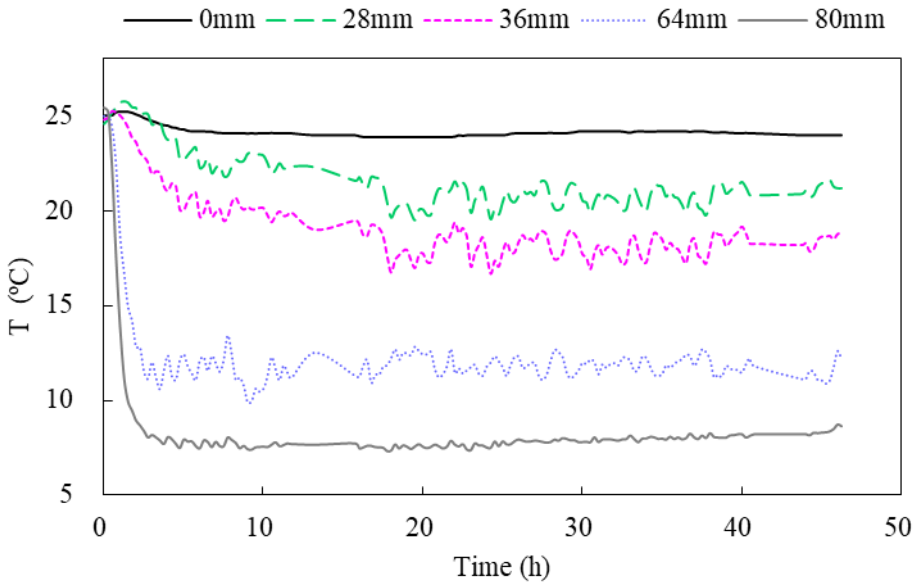

Figure 4.16. Temperature changes at different depths of the wall under non-isothermal condition

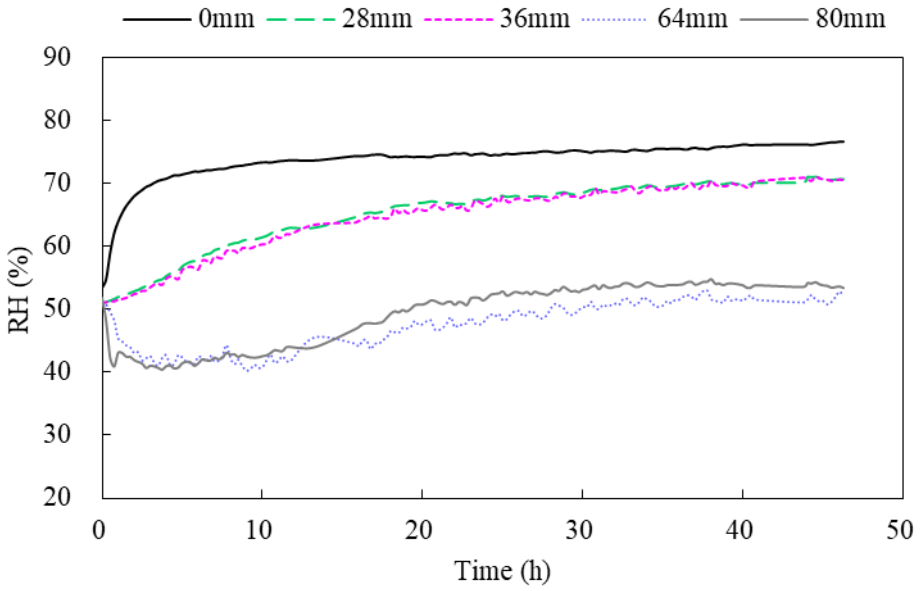

Figure 4.17. Relative humidity changes at different depths of the wall under non-isothermal condition

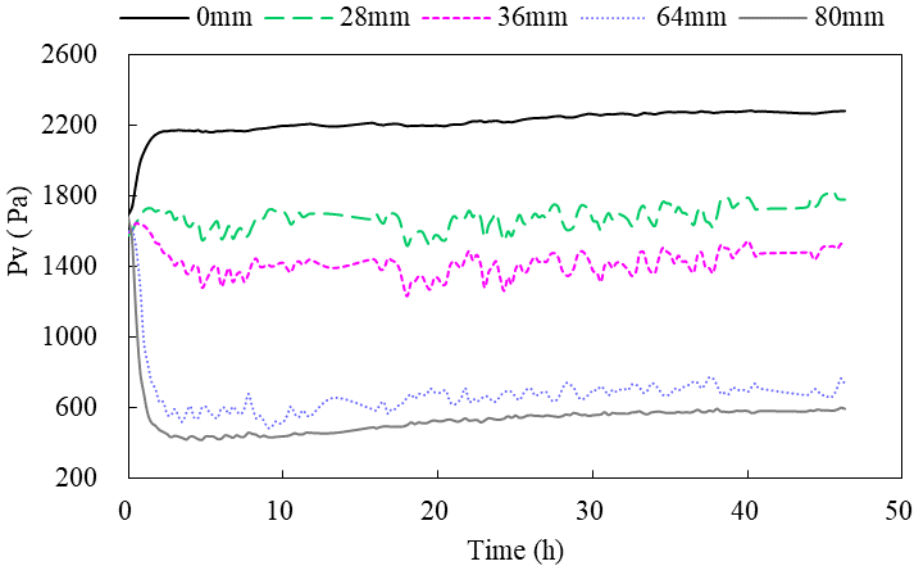

Figure 4.18. Vapor pressure changes at different depths of the wall under non-isothermal condition

Based on the Eq. (4.2), Figure 4.19 shows the estimated mass change of the wall. The amount of water stored in the wall was about 134g. Compared to the moisture

storage after 4 days under the isothermal condition, the amount of moisture storage after 2 days was higher under the non-isothermal condition. This indicated the temperature has a pronounced effect on the moisture content of the material

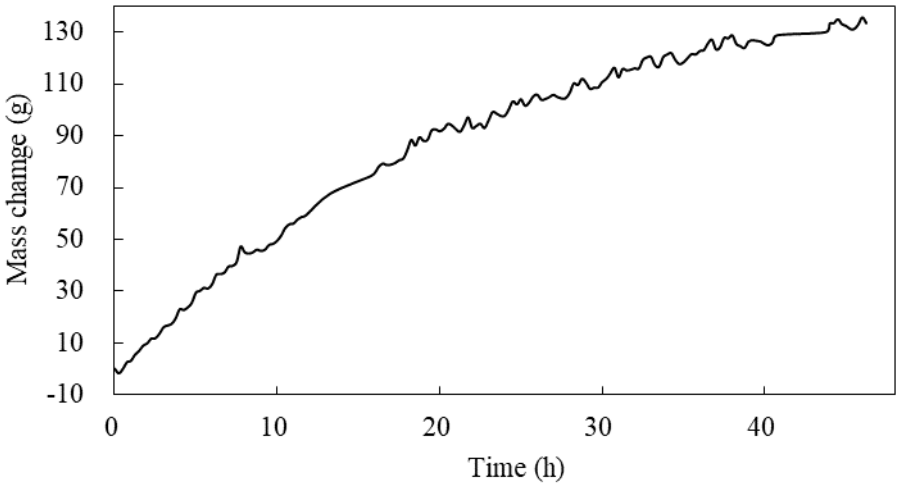

Figure 4.19. Moisture content stored in the wall under non-isothermal condition

4.4.3. Dynamic condition

Figure 4.20 shows the measured 4-day internal and external air conditions under dynamic condition. The internal temperature and relative humidity were kept almost constant at 24 ºC and 75%. For the external compartment, the increase/decrease of temperature resulted in the decrease/increase of relative humidity as the saturated vapor pressure is relevant to temperature. The external temperature fluctuated from 15.4 to 7.2, and accordingly the relative humidity varied from 48% to 57% at every 12 h.

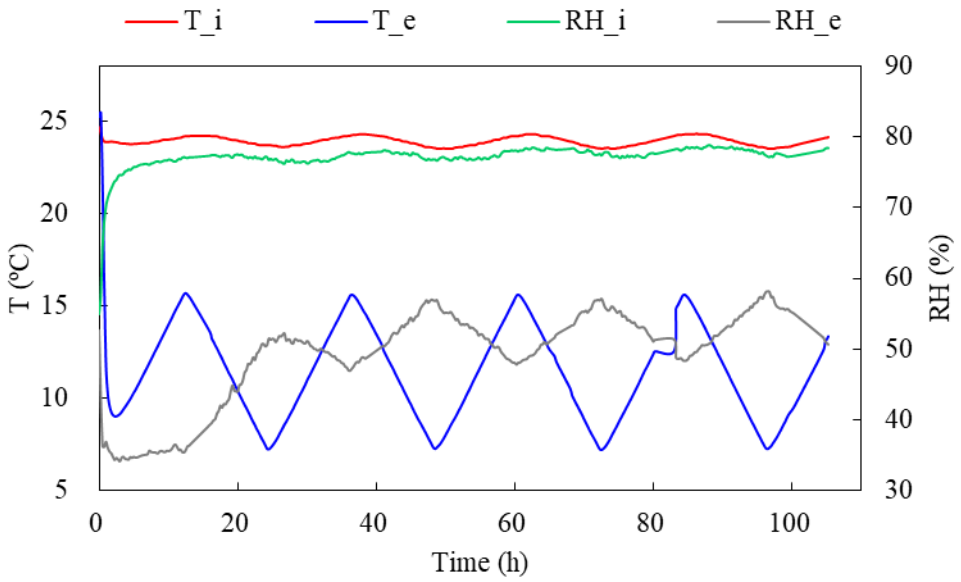

Figure 4.20. The internal and external air conditions under dynamic condition

The temperature, relative humidity and vapor pressure changes at various depths of the wall are presented in Figures 4.21-4.23. From Figure 4.21, a thermal phase shift from external side to internal side can be observed. The thermal phase shift is a commonly used parameter to evaluate the effectiveness of a material in thermal comfort. The thermal phase shift is defined as the required time to propagate the external temperature oscillations from exterior to interior surface of the material [134]. A material with a high thermal phase shift contributes to a comfortable indoor environment. The mean thermal phase shift provided by the 80 mm of rice straw alginate insulation material with the density of 124 kg/m^3 was about 2.5 h. This insulation material is comparable to Woodfibre insulation, with a thermal phase shift of 1.75 h for a density of 160 kg/m^3 and a thickness of 60 mm and with a thermal phase shift of 3 h for a density of 150 kg/m^3 and a thickness of 80 mm found in [135].

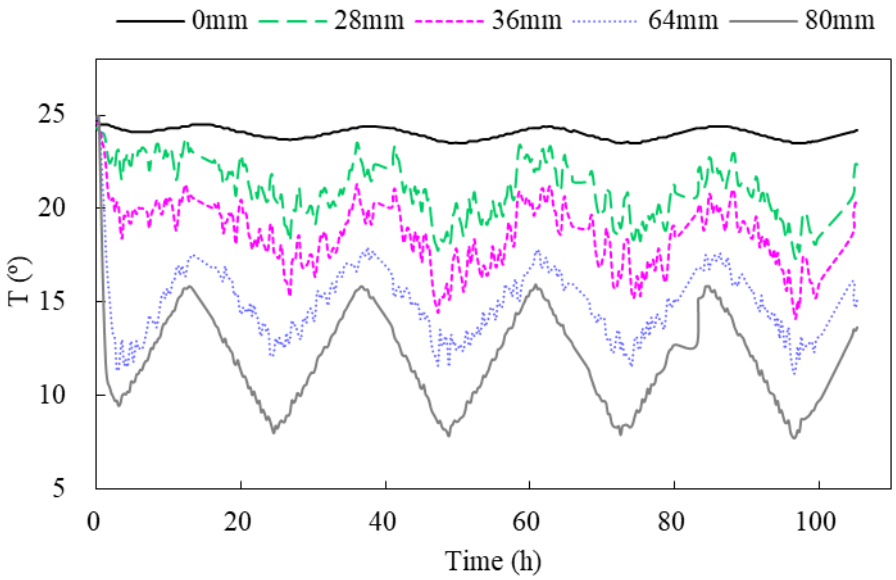

Figure 4.21. Temperature changes at different depths of the wall under dynamic condition

As it can be seen in Figures 4.22 and 4.23, the vapor pressure gradient always induced a vapor flux from the interior to the exterior surfaces. At the depths of 28 mm and 36 mm, the relative humidity was quite stable in higher level and the vapor pressure variation had the same trend with temperature. This result can be attributed to the combined effect of the dependency of saturated vapor pressure and moisture sorption capacity of the material on the temperature. In particular, the relative humidity decreased at a higher saturated vapor pressure caused by the increase of temperature. Conversely, the relative humidity increased when the temperature decreases. However, the moisture sorption capacity of porous materials decreased when temperature increased and thus liquid water evaporated leading to higher relative humidity. On the contrary, the moisture sorption capacity of porous materials increased when temperature decreased and thus water condensed leading to lower relative humidity. Therefore, the stability of relative humidity at the depths of 28 mm and 36 mm might be explained by a compromise between the variations of vapor pressure caused by moisture sorption and the variations of saturated vapor pressure caused by temperature

variations. At the depth of 64 mm, the vapor pressure variation had the same trend with the temperature. Nevertheless, the relative humidity cannot be only explained by the temperature effect.

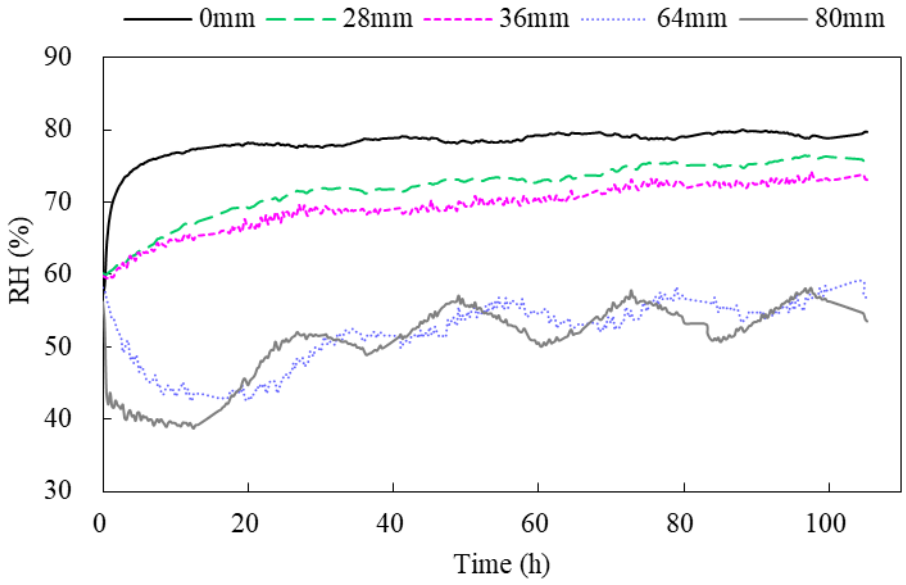

Figure 4.22. Relative humidity changes at different depths of the wall under dynamic condition

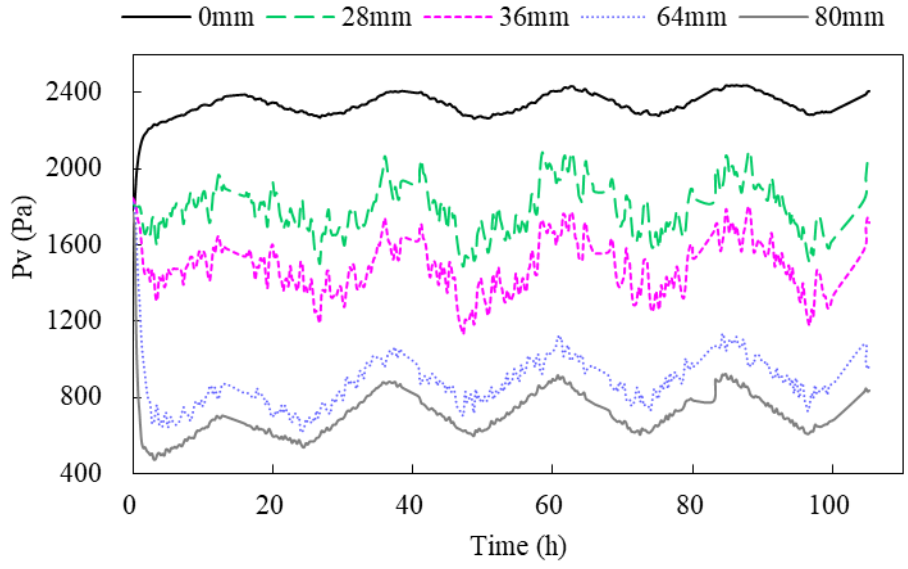

Figure 4.23. Vapor pressure changes at different depths of the wall under dynamic condition

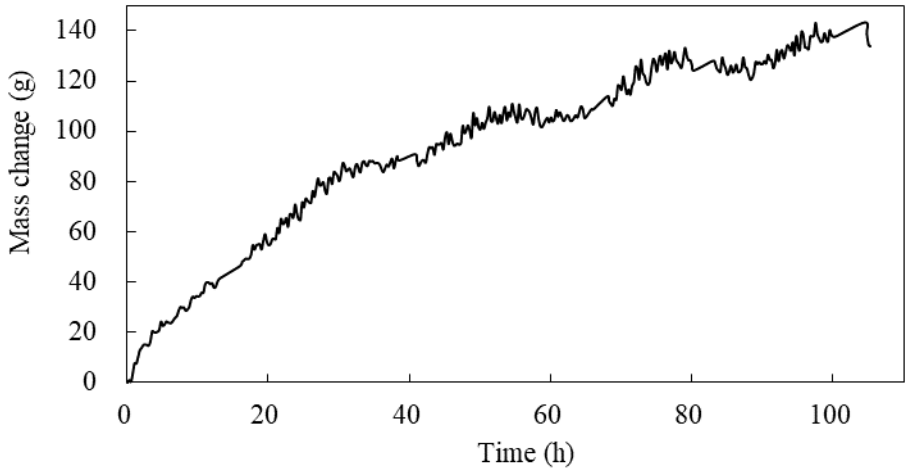

Figure 4.24. Moisture content stored in the wall under dynamic condition

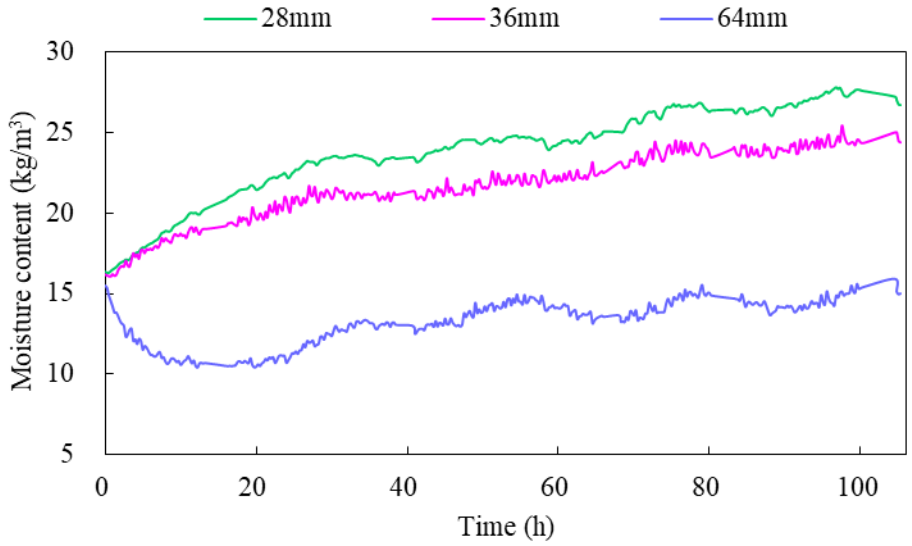

Figure 4.25. Moisture content changes at different depths of the wall under dynamic test

Based on the Eq. (4.2), Figure 4.24 shows the estimated mass change of the wall. The maximum water stored by the wall is about 143g. In the first 20h, the wall stored about 54g water and then the wall stored and released water periodically. But the water released was far less than the water absorbed. This can be further confirmed by the moisture content variations calculated by the relative humidity and sorption isotherm for the three positions within the wall, as shown in Figure 4.25. This indicated that the

moisture content of the material can be affected by the temperature.

4.5. Conclusions

The hygrothermal behaviour of the rice straw alginate insulation material in this thesis was investigated at wall scale. Different boundary conditions including isothermal condition, non-isothermal condition and dynamic condition were applied. Heat and moisture coupling effect in the wall panel was analysed and discussed. The results under the isothermal condition showed that moisture transport had the impact on temperature changes due to moisture sorption. The condensation/evaporation of water vapor related to the moisture storage and moisture diffusion induced the increase/decrease of temperature. The results under the non-isothermal condition indicated that the moisture transport can be affected by temperature gradient. From the dynamic test, the material presented a high thermal phase shift comparable to wood fibre insulation, contributing to a comfortable indoor environment. Besides, the obtained results indicated that the material is an interesting bio-sourced material for moisture uptake and release.

5. Numerical modelling heat and moisture transfer in rice straw alginate insulation panel

5.1. Introduction

Coupled heat and moisture transfer models are commonly used in predicting hygrothermal behaviour across thickness of a material and an envelope in buildings. They have been widely applicated in building fields, such as mould risk [136], durability [137]and energy consumption [138].

The mass and energy conservation equations are necessary to build heat and moisture transfer models. Regarding to the moisture transfer, different driving potentials can be used including relative humidity, partial vapor pressure, capillary pressure, moisture content and air moisture content. Some theoretical foundations for heat and moisture transfer models in porous materials are proposed by Philip and De

Vries [139], Luikov [140]and Whitaker [141]. In 1957, Philip and De Vries developed the first heat and moisture model with the assumption of moisture transfer as a function of temperature [139]. The volumetric moisture content and temperature are adopted as the driving potentials. In 1966, Luikov introduced the irreversible thermodynamics to predict heat and moisture transfer [140]. The driving potentials are relative moisture content and temperature. In 1997, Whitaker proposed a detailed theory to describe the transport for each phase based on the integration of mass, momentum and energy conservation equations [141]. The driving potentials are moisture content and temperature. However, these models are limited as they have many transport parameters and coefficients, which are difficult to obtain. Moreover, for multi-layer wall, the driving potential of moisture content is discontinuous between different layers. In 1995, Künzel attempted to use relative humidity as the driving potential and simplify the moisture transfer toa pure diffusive model [142]. This model ignored the thermal transfer in liquid phase. In 1999, Mendes proposed a heat and moisture transfer model based on the theory of Phillip and De Vries for multi-layer wall with the driving potentials of volumetric moisture content and temperature[143]. In the past years, various heat and moisture transfer models have been developed to simulate the hygrothermal behaviour in building envelopes [144, 145].

This chapter aims to validate a coupled heat and moisture transfer (CHM) model on a rice straw alginate insulation wall. Relative humidity and temperature are chosen as driving potentials. Additionally, this model is solved by the finite element method embedded in the COMSOL Multiphysics software. The experimental data from Chapter 4 under the three boundary conditions will be used for validation. Also, a transient heat transfer model are used for comparison to analyse the significant of coupling necessity of heat and moisture in the developed material.

5.2. Mathematical model

The CHM model used in this thesis follows the standard of EN ISO 15026 [146]. For simplicity, some assumptions are made for the CHM model as follows:

(1) The material is assumed as homogenous;

(2) Local thermal and moisture equilibrium exist within the material;

(3) The water vapor is regarded as an ideal gas;

(4) The moisture sorption capacity is independent of temperature;

(5) The heat transfer and moisture transfer are regarded as one dimensional.

5.2.1. Moisture conservation equation

In porous materials, the moisture transport is considered in two phases including water vapor and liquid water. According to the law of mass conservation, the moisture transport equation is given as:

$$\rho_m \frac{\partial u}{\partial t} = -\nabla(g_v + g_l) \tag{5.1}$$

Where ρ_m is the dry density; u (kg/kg) is the mass moisture content; g_v (kg/(m^2·s·Pa)) is water vapor transmission rate; g_l (kg/(m^2·s·Pa)) is liquid water transmission rate.

In this model, the water vapor transfer is described by Fick's law and the liquid water transfer is described by Darcy's law:

$$g_v = -\delta_p \frac{\partial P_v}{\partial x} \tag{5.2}$$

$$g_l = -K_l \frac{\partial P_c}{\partial x} \tag{5.3}$$

Where δ_p (kg/(m·s·Pa)) is the water vapor permeability; K_l (kg/(m·s·Pa)) is the liquid water permeability; P_v (Pa) is the partial vapor pressure; P_c (Pa) is the capillary pressure.

For convenience of calculations, this model adopts relative humidity as the driving factor for moisture transport. Therefore, the vapor pressure gradient can be deduced as:

$$\frac{\partial P_v}{\partial x} = \frac{\partial(\varphi P_{v,sat})}{\partial x} = \varphi \frac{dP_{v,sat}}{dT}\frac{\partial T}{\partial x} + P_{v,sat}\frac{\partial \varphi}{\partial x} \tag{5.4}$$

Where $P_{v,sat}$ is the saturated water vapor pressure under experimental temperature (Pa); φ (-) is the relative humidity.

The temperature dependent saturated water vapor pressure is described as:

$$P_{v,sat}(T) = 610.5\exp\left(\frac{17.269T}{237.3+T}\right) \tag{5.5}$$

Based on Kelvin equation, the capillary pressure gradient can be deduced as:

$$\frac{\partial P_c}{\partial x} = \rho_l R_v \left(In(\varphi)\frac{\partial T}{\partial x} + \frac{T}{\varphi}\frac{\partial \varphi}{\partial x}\right) \tag{5.6}$$

Where ρ_l (kg/m^3) is the liquid water density; R_v (J/(kg·K)) is the water vapor gas constant and T (K) is the thermodynamic temperature.

Therefore, substituting the Eqs. (5.4) and (5.6) into Eq. (5.1), the moisture transfer equation is as follows:

$$\rho_{\mathrm{m}}\xi\frac{\partial \varphi}{\partial x} = \frac{\partial}{\partial x}\left[\left(\delta_p\varphi\frac{dP_{v,sat}}{dT} + K_l R_v In(\varphi)\right)\frac{\partial T}{\partial x} + \left(\delta_p P_{v,sat} + K_l\rho_l R_v\frac{T}{\varphi}\right)\frac{\partial \varphi}{\partial x}\right] \tag{5.7}$$

Where $\xi = \partial u/\partial\varphi$ represents the slope of sorption isotherm, $u = f(\varphi)$

5.2.2. Heat transfer equation

Considering that the latent heat of vaporization is much higher compared with the sensible heat of water vapor and liquid water, they are neglected in this model. The heat conservation in the material can be expressed by:

$$\left(\rho_m C_{p,m} + wC_{p,l}\right)\frac{\partial T}{\partial t} = \frac{\partial}{\partial x}\left(\lambda\frac{\partial T}{\partial x}\right) + L_v\left(\delta_p\left(\varphi\frac{\partial P_{v,sat}}{\partial x}\frac{\partial T}{\partial x} + P_{v,s,sat}\frac{\partial \varphi}{\partial x}\right)\right) \quad (5.8)$$

Where λ (W/(m·K)) is the thermal conductivity of the material; w (kg/m^3) is the moisture content; $C_{p,m}$ (J/(kg·K)) is the mass specific heat capacity of the material; $C_{p,l}$ (J/(kg·K)) is the mass specific heat capacity of water; L_v (J/kg) is the latent heat of evaporation.

5.2.3. Boundary and initial conditions

Regarding to the HAMSTAD Benchmark case 2, the boundary conditions of the internal and external sides are given as:

$$g_i = \beta_i(\varphi_i P_{sat,i} - \varphi_{surfi} P_{sat,surfi}) \quad (5.9)$$

$$g_e = \beta_e(\varphi_e P_{sat,e} - \varphi_{surfe} P_{sat,surfe}) \quad (5.10)$$

$$q_i = h_i(T_i - T) + L_v g_i \quad (5.11)$$

$$q_e = h_e(T_e - T) + L_v g_e \quad (5.12)$$

Where g (kg/(m^2·s)) is the vapor flux at the boundaries; q (W/m^2) is the heat flux at the boundaries; β (kg/(m^2·s·Pa)) is the vapor transfer coefficient at the boundaries; h (W/(m^2·K)) is heat transfer coefficient at boundaries ignoring radiation.

The boundary conditions applied in the rice straw alginate insulation wall panel are the temperature and relative humidity in the surface of the wall, which are given as:

$$\varphi(x = 0, t) = \varphi_i(t) \quad (5.13)$$

$$\varphi(x = L, t) = \varphi_e(t) \tag{5.14}$$

$$T(x = 0, t) = T_i(t) \tag{5.15}$$

$$T(x = L, t) = T_e(t) \tag{5.16}$$

The initial conditions for moisture and heat transport are given by:

$$\varphi(x, 0) = \varphi_0 \tag{5.17}$$

$$T(x, 0) = T_0 \tag{5.18}$$

Where φ_e and φ_i are the relative humidity in the exterior and interior surfaces of the wall respectively; T_e (K) and T_i (K) is the thermodynamic temperature in the exterior and interior surfaces of the wall respectively.

5.2.4. Solving methods

This study uses COMSOL Multiphysics software to implement the CHM model. The software is a platform to implement partial differential equations (PDEs), which employs finite element method for solving the coupled equations. In the platform, the general form PDE interface provides a general form for solving PDEs, which is given by:

$$e_a \frac{\partial^2 u}{\partial t^2} + d_a \frac{\partial u}{\partial t} + \nabla \Gamma = f \tag{5.19}$$

Where e_a is the mass coefficient, equalling to zero in this study; d_a is a damping coefficient; Γ is the conservative flux; f is the source term, equalling to zero in this study.

In this study, the dependent variable u is the temperature and relative humidity. According to the previously definition, the CHM model can be given as a matrix form:

$$\begin{bmatrix} \rho_m C_{p,m} + wC_{p,l} & 0 \\ 0 & \rho_{\mathrm{m}}\xi \end{bmatrix} \begin{bmatrix} \frac{\partial T}{\partial t} \\ \frac{\partial \varphi}{\partial t} \end{bmatrix} =$$

$$\nabla \left\{ \begin{bmatrix} \lambda + L_v \delta_p \varphi \frac{dP_{v,sat}}{dT} & \delta_p \varphi \frac{dP_{v,sat}}{dT} \\ \delta_p \varphi \frac{dP_{v,sat}}{dT} + K_l R_v In(\varphi) & \delta_p P_{v,sat} + K_l \rho_l R_v \frac{T}{\varphi} \end{bmatrix} \nabla \begin{bmatrix} T \\ \varphi \end{bmatrix} \right\} \tag{5.20}$$

5.4. HAMSTAD Benchmark case 2

Before employing the CHM model for the developed rice straw alginate insulation wall panel, it was verified on the HAMSTAD Benchmark case 2. In this case, a 200 mm single insulation layer wall subjected to the isothermal condition is targeted. Temperature is always equalled to 20 ºC during the hypothetical case. After initialized at the high relative humidity of 95%, the wall is exposed to boundary conditions at lower relative humidity. The internal and external relative humidity values are 65% and 45%, respectively. Additionally, the heat and moisture transfer coefficients are assumed as 25 W/(m^2·K) and 1.0×10^{-3} s/m, respectively. Table 5.1 presents the material properties. Due to the zero gradient of temperature, the moisture content profiles in the wall can be obtained by an analytical solution. The simulation lasts 1000 h and the obtained results are the moisture profiles at 100, 300 and 1000h.

Table 5.1 Properties of the insulation material described in HAMSTAD Benchmark case 2

Material properties	Value/formula
Density ρ_m (kg/m^3)	525
Thermal conductivity λ (W/(m·K))	0.15
Specific heat capacity $C_{p,m}$ (J/(kg·K))	800
Sorption isothermal w (kg/m^3)	$\frac{116}{\left(1-\frac{1}{0.118}\ln\varphi\right)^{0.869}}$
Water vapor permeability δ_v (kg/(m·s·Pa))	1×10^{-15}
Moisture diffusivity D_w (m^2/s)	6×10^{-10}

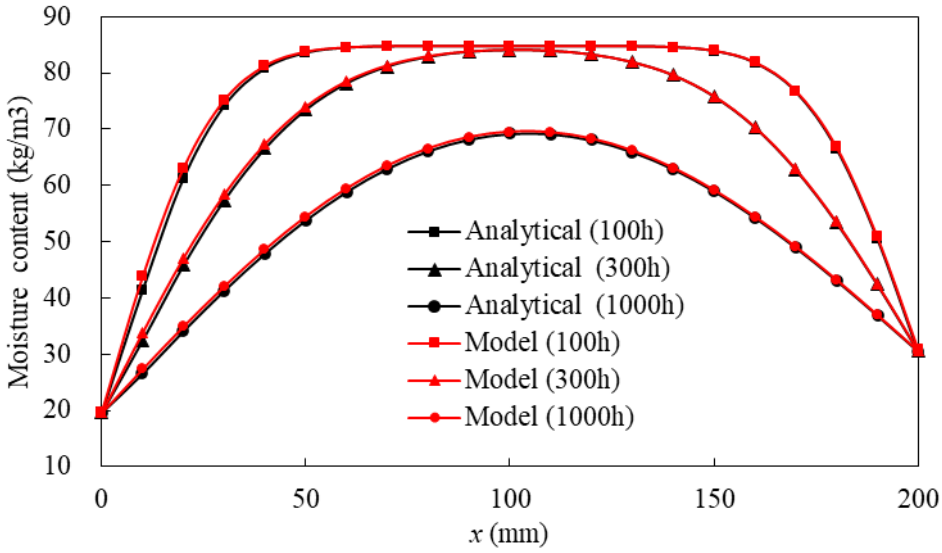

Figure 5.1. Moisture content profiles at 100, 300 and 1000h

Figure 5.1 compared the simulated results of the CHM model with the results from analytic method. It can be observed that the CHM model generated the moisture content profiles very close to the profiles from analytic method. The maximum relative errors between the CHM model and the analytic method were 5.4%, 4.3% and 2.9% at 100, 300 and 1000h, respectively.

5.5. Experimental validation

Considering that the liquid water transport coefficient is not available for the developed material, the CHM model employed in this Chapter only considers the moisture transport in vapor phase with the ignoration of liquid water transport. The rice straw alginate insulation wall panel experimentally studied under isothermal, non-isothermal and dynamic conditions are targeted. The boundary conditions in numerical calculations were the surface temperature and relative humidity imported from the experiment. The initial values of temperature and relative humidity were the mean measurements at the three locations (i.e., x = 28, 36, 64 mm). Consequently, the initial

temperature and relative humidity were 25.6ºC and 58% for the isothermal condition, 24.8º C and 50.9% for the non-isothermal condition, 24.6º C and 59% for the dynamic condition. A transient heat transfer (TH) model was used for comparison to demonstrate the coupling necessity of heat transfer and moisture transfer.

5.5.1. Material properties

The thermal and hygric properties obtained in Chapter 3 were used as input parameters, as shown in Table 5.2. The thermal conductivity of the material at dry state was measured using the hot wire method. Moreover, the thermal conductivity was dependent on the moisture content of the material, and the coefficient was set to 0.56. The sorption isotherm function was a GAB fit of the mean values of adsorption and desorption isotherms. The water vapor permeability was assumed to be linearly related to the relative humidity based on the results of dry cup and wet cup.

Table 5.2 Properties of the rice straw alginate insulation material

Variable	Search space	Unit
Dry density	ρ = 124	kg/m^3
Mass specific heat capacity	Cp = 1353	J/kg/K
Thermal conductivity	$\lambda = 0.042 + 0.56\frac{w}{1000}$	W/m/K
Sorption isotherm	$u = \frac{0.2978 \cdot \varphi}{(1 - 0.9560 \cdot k)(1 - 0.9560 \cdot \varphi + 4.6027 \cdot \varphi)}$	kg/kg
Water vapor permeability	$(6.69 \cdot \varphi + 1.44) \times 10^{-11}$	s

5.5.2. Isothermal condition

Figure 5.2 illustrates the temperature variations at different depths predicted by the CHM model, together with the experimental measurements and errors of the CHM model and the TH model. For both models, larger errors can be observed in the beginning transient state compared to the lately almost steady state. This is attributed to the moisture sorption during the transient time. It can be found that the CHM model had smaller errors compared to the TH model. Specifically, at the depths of 28, 36 and 64 mm, the CHM model had the maximum errors of 1.2 ºC, 0.7 ºC and 1.5 ºC, while the TH model had the maximum errors of 1.5ºC, 1.0 ºC and 2.2 ºC, respectively. Also, for the three locations, the CHM model had the smaller mean absolute error, i.e., 0.4 ºC, 0.3 ºC and 0.3 ºC compared to the 0.7 ºC, 0.5 ºC, 0.4 ºC generated by the TH model. This indicates that moisture transport can influence the thermal behaviour of the wall.

Figure 5.3 shows the relative humidity variations at different depths predicted by the CHM model, together with the experimental measurements and errors of the CHM model. The predicted curve showed the similar tends to the experimental curve. However, a gap can be observed between the experimental curves and predicted curves. In particular, the predicted curves were always located below the experimental curves at the depths with moisture uptake (see Figure 5.3 (a) and (b)) and above the experimental curve at the depth with moisture release (see Figure 5.3. (c)). Also, errors increased in the process of condensation/evaporation of water vapor, and then stabilized at an almost constant value without increasing over time. The maximum errors of relative humidity were 8%, 6% and 13% and the mean absolute error were 7%, 4% and 6% at the depths of 28 mm, 36 mm and 64 mm, respectively.

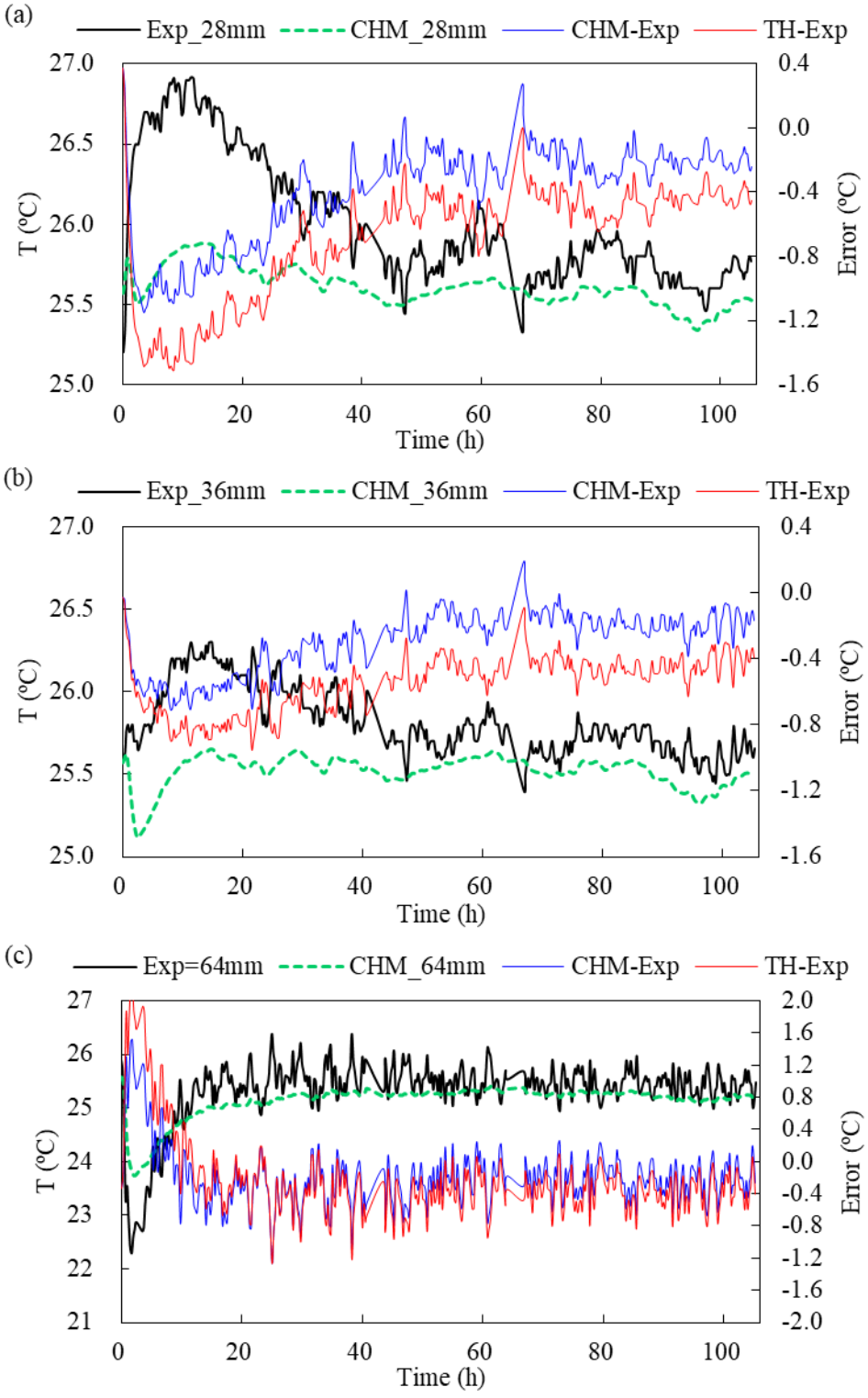

Figure 5.2. Temperature comparison of numerical results with experimental results

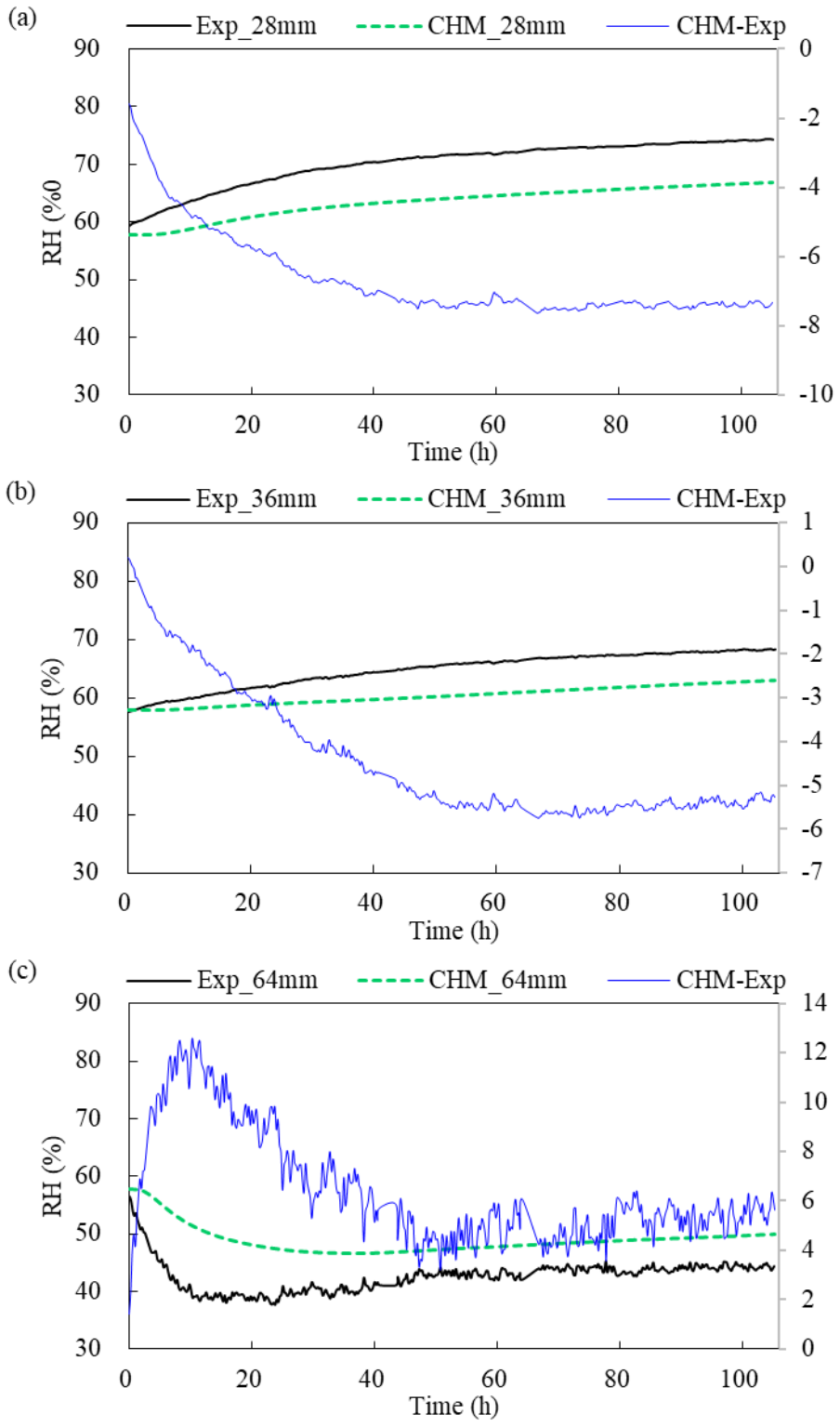

Figure 5.3. Relative humidity comparison of numerical results with experimental results

Figure 5.4 shows the changes of vapor pressure at different locations predicted by the CHM model, together with the experimental measurements and errors predicted by both the CHM and TH models. Regarding to the TH model, the vapor pressure values were calculated by temperature values and a fixed relative humidity value equalling to the initial relative humidity. The relative error is the difference between predicted and measured values divided by the measured values. As it can be seen, the CHM model predicted the vapor pressure more accurate than the TH model. Similar to the relative humidity, the predicted curves by the CHM model were always located below the experimental curves at the depths with moisture uptake and above the experimental curve at the depth with moisture release. It indicates that the actual response is faster than the theoretical response of the wall. From an experimental point of view, it is difficult to stabilize and homogenize the temperature and relative humidity across the thickness of the wall before starting the experiment due to perturbations existed in the compartments. Moreover, in this model, some simplifications are made. For example, the liquid water transport and hysteresis effect of moisture sorption are neglected, probably influencing the estimated variations of relative humidity and vapor pressure, especially for the bio-based materials with high moisture buffering capacity.

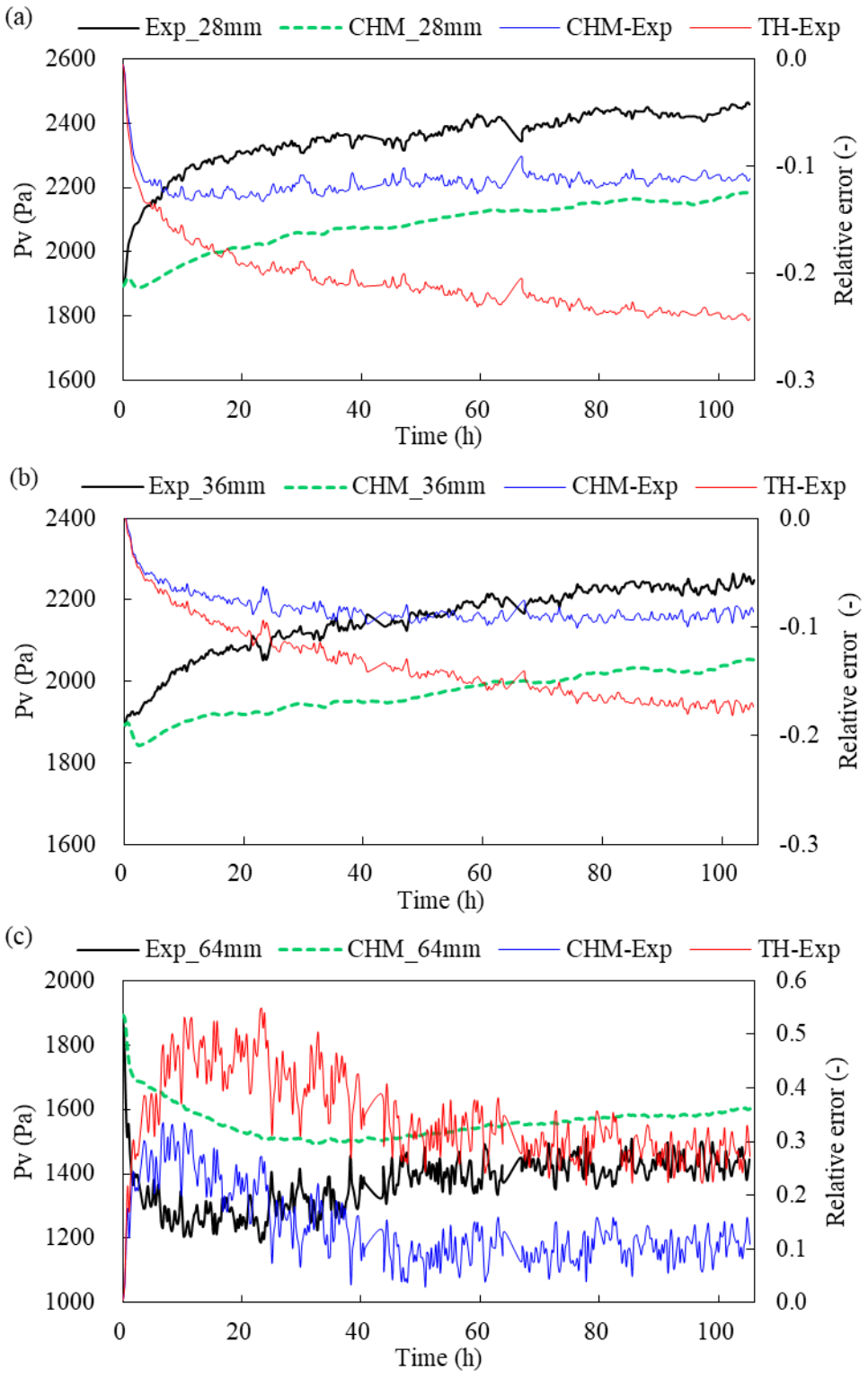

Figure 5.4. Vapor pressure comparison of numerical results with experimental results

Figure 5.5. shows the sensible, latent heat, total heat fluxes of interior surface predicted the CHM models and the sensible heat flux of interior surface predicted by the TH model. The sensible heat flux had no obvious change over time for the TH model, which is due to the isothermal condition with small temperature gradient. Contrary to the TH model, the sensible heat flux had negative values at first and then it was gradually vanished. A negative sign represents the surface releasing heat to the ambient environment. This implies an exothermic phenomenon in the wall as a result of water vapor condensed in the wall. Moreover, the difference in vapor flux between the interior and exterior surfaces predicted by the CHM model shows that the wall adsorbed water from environment (Figure 5.6).

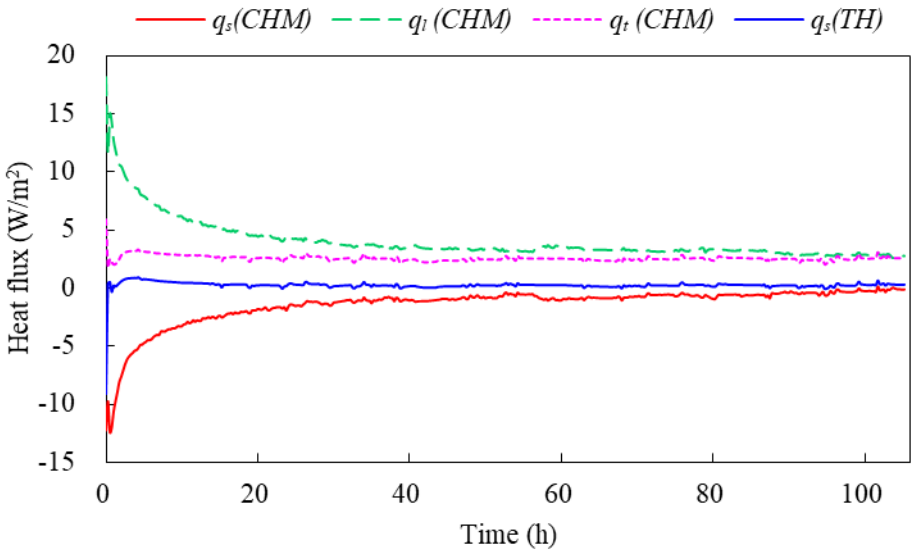

Figure 5.5. The heat fluxes through the interior surface predicted by the TH model and the CHM model

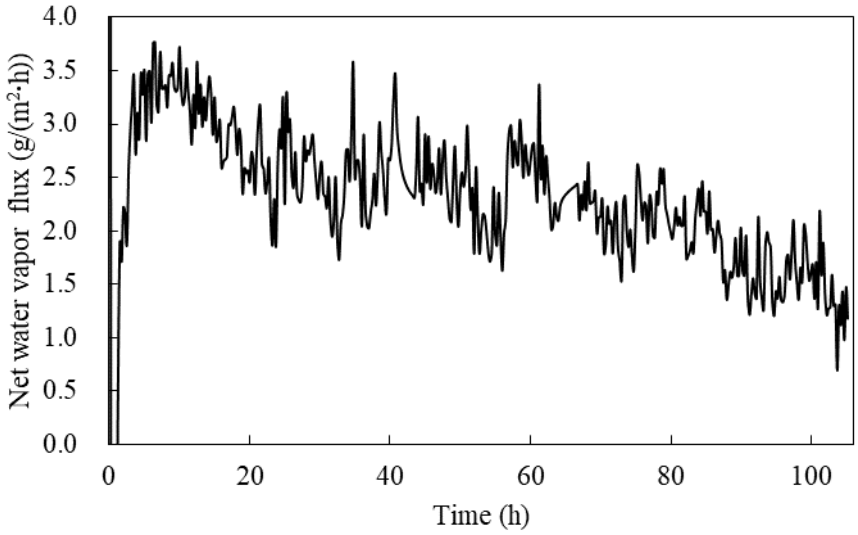

Figure 5.6. The vapor flux difference between the interior and exterior surfaces predicted by the CHM model

5.5.3. Non-isothermal condition

As shown in Figure 5.7, the CHM model had smaller errors compared to the TH model. Specifically, at the depths of 28, 36 and 64 mm, the CHM model had the maximum errors of 4.4 ºC, 3.4 ºC and 1.9 ºC, while the TH model had the maximum errors of 5.2 ºC, 4.1 ºC and 2.2 ºC, respectively. Also, for the three positions, the CHM model had the smaller mean absolute error, i.e., 1.7 ºC, 1.0 ºC and 0.5 ºC compared to the 2.6 ºC, 1.7ºC, 0.7 ºC generated by the TH model. Among the three positions, the difference of errors between the CHM model and the TH model was smallest at the depth of 64 mm. This location is closer to the external environment, where thermal transfer is more pronounced so that the effect of moisture transport on the thermal behaviour is weaken. It can be found from Figure 5.8 that the CHM model had smaller errors of relative humidity at the depth of 64 mm compared to the other two positions. Specifically, the maximum errors are 11%, 12% and 10%, and the mean absolute errors were 8%, 9% and 4% at the depths of 28 mm, 36 mm and 64 mm respectively. One

possible reason for this might be that liquid transfer is more pronounced at the depths of 28 mm and 36 mm, where the actual relative humidity is much higher. And thus, at these two positions, the CHM model is more difficult to track the changes of moisture content, leading to larger errors. Moreover, the CHM model predict the vapor pressure more accurate than the TH model, as shown in Figure 5.9. These results further verify the highly coupling effect of heat transfer and moisture transfer.

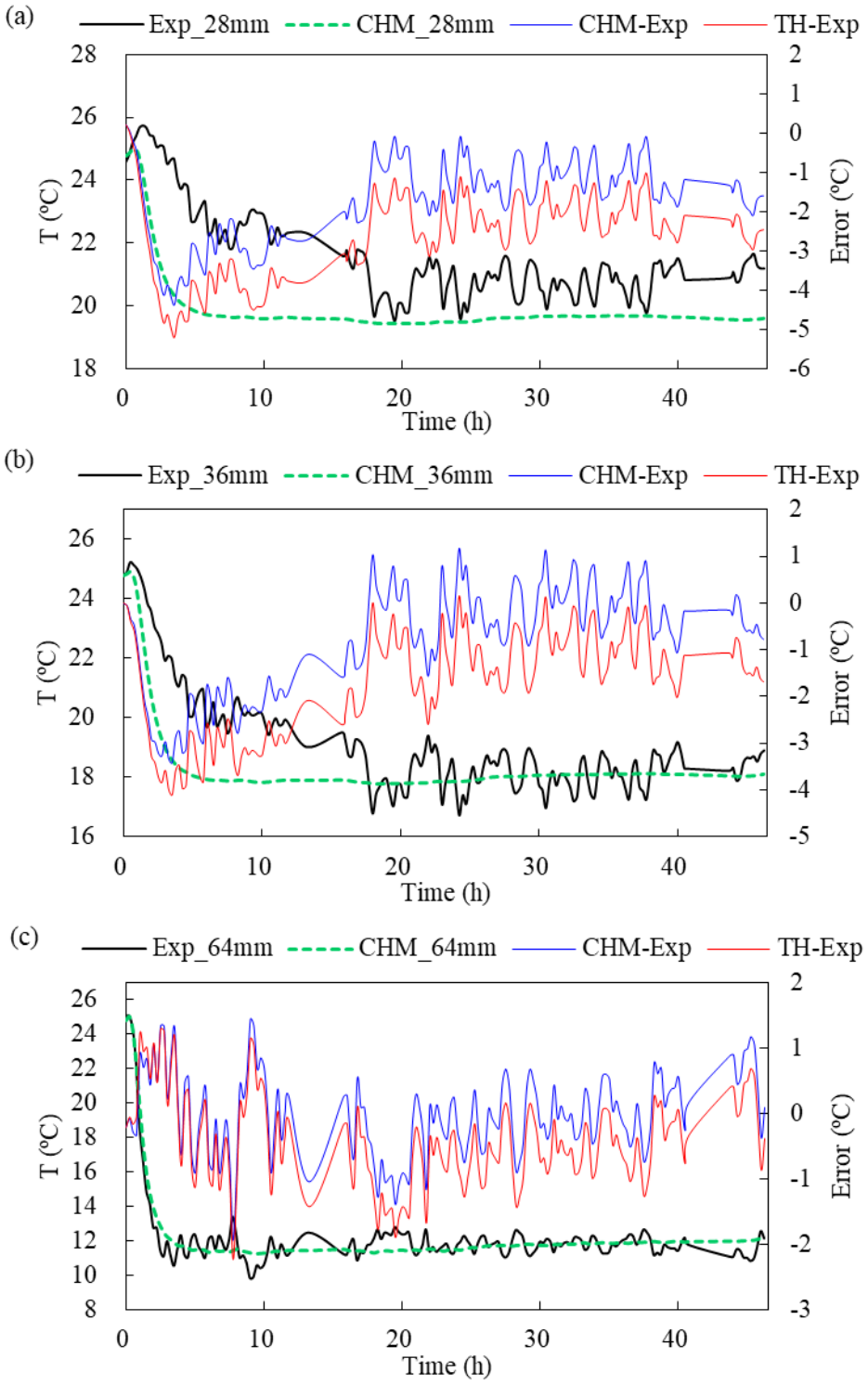

Figure 5.7. Temperature comparison of numerical results with experimental results

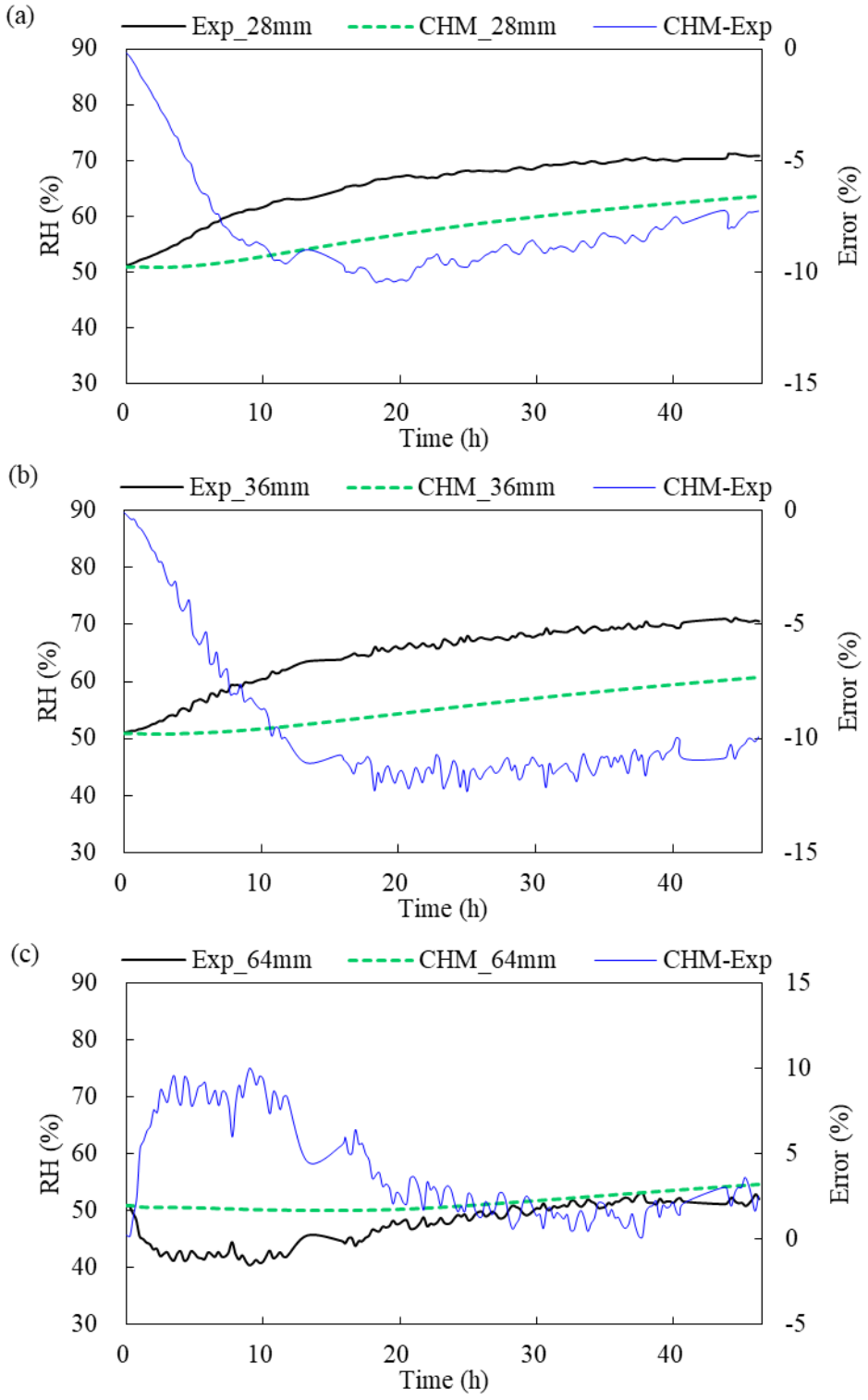

Figure 5.8. Relative humidity comparison of numerical results with experimental results

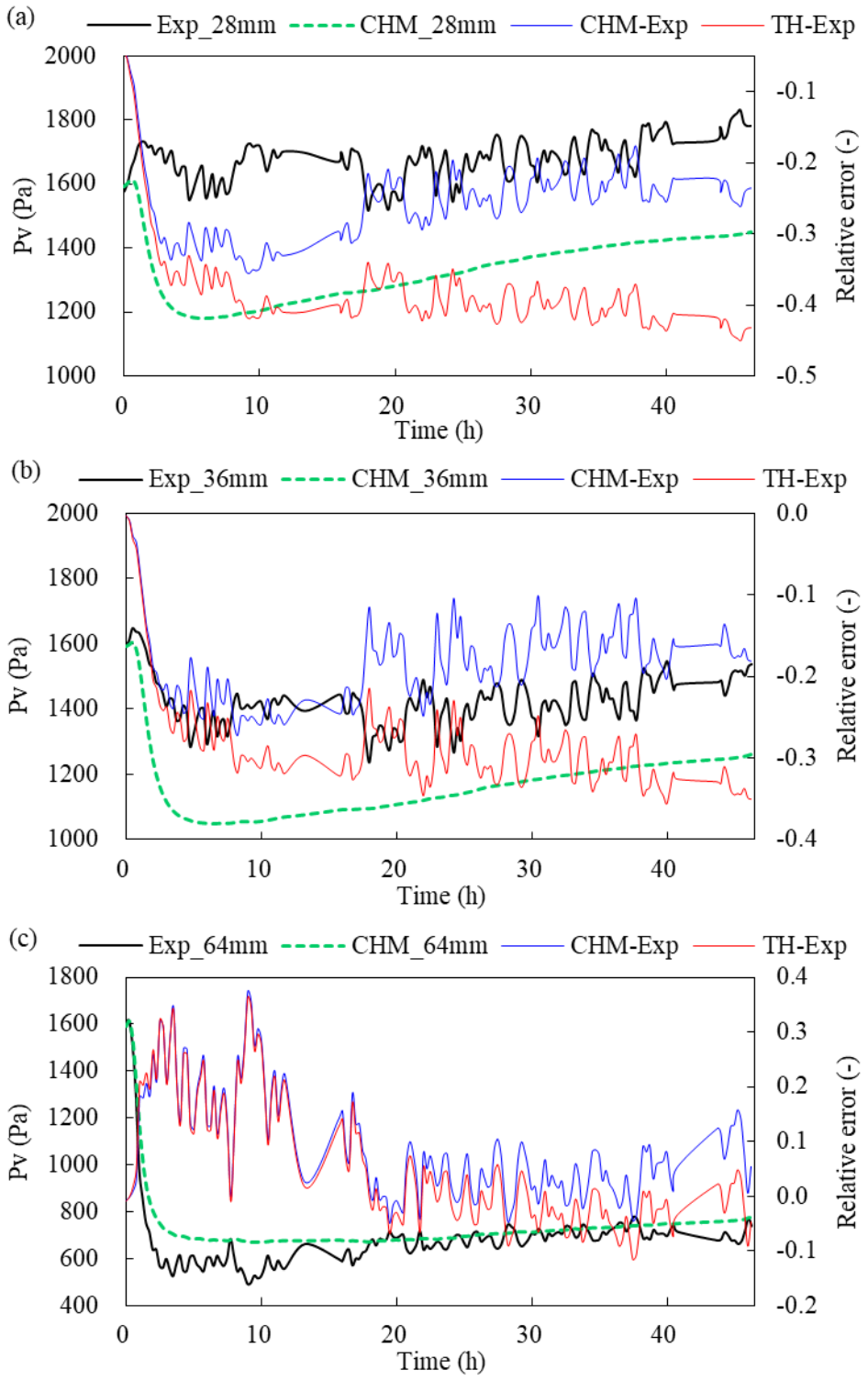

Figure 5.9. Vapor pressure comparison of numerical results with experimental results

Figure 5.10. shows the sensible, latent heat, total heat fluxes of interior surface predicted the CHM models and the sensible heat flux of interior surface predicted by the TH model. With the inter-model comparison, the sensible heat flux was overestimated by 33.2% by the TH model compared to the CHM model. The latent heat flux accounted for 43.6% of the total heat flux predicted by the CHM model. Therefore, the total heat flux was underestimated by 25% by the TH model compared to the CHM model. Figure 5.11 shows the vapor flux difference between the interior and exterior surfaces of the wall predicted by the CHM model, indicating the wall absorbed water from environment.

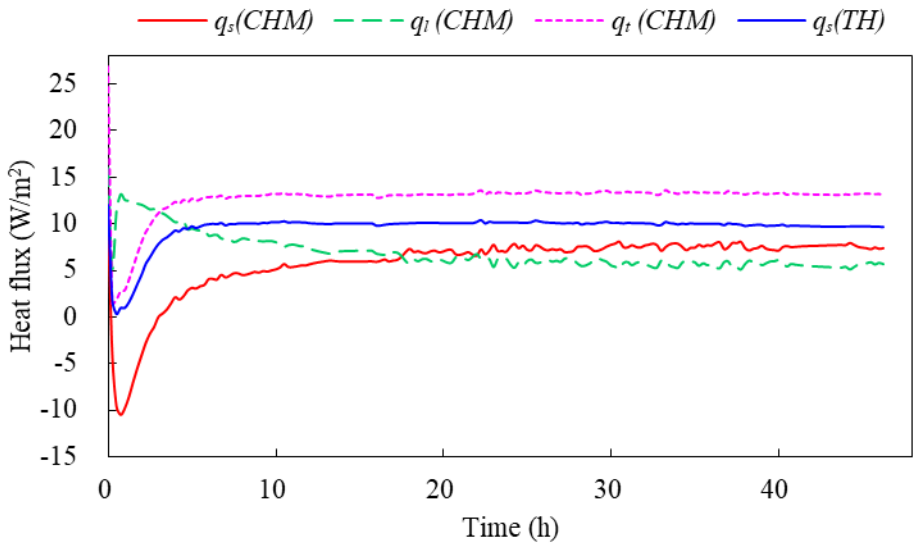

Figure 5.10. The heat fluxes through the interior surface predicted by the TH model and the CHM model

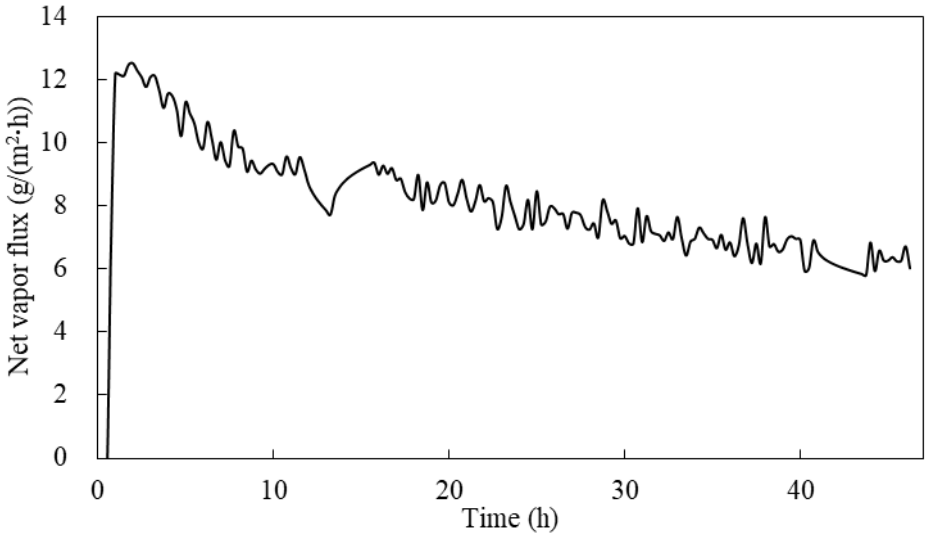

Figure 5.11. The vapor flux difference between the interior and exterior surfaces of the wall predicted by the CHM model

5.5.4. Dynamic condition

As shown in Figure 5.12, the CHM model had smaller errors compared to the TH model. Specifically, the maximum differences for the TH model are 3.5ºC, 3.0 ºC and 1.9 ºC at the depths of 28 mm, 36 mm and 64 mm, respectively. The maximum differences for the CHM model are 2.9 ºC, 1.4 ºC and 1.4 ºC at the depths of 28 mm, 36 mm and 64 mm, respectively. For the three positions, the mean absolute errors were 2.0 ºC, 0.8ºC, 0.5 ºC for TH model and 1.6 ºC, 0.3 ºC and 0.8 ºC for the CHM model. As shown in Figure 5.13, for the CHM model, the maximum errors of relative humidity were 8%, 8% and 14% at the depths of 28 mm, 36 mm and 64 mm, respectively. The mean absolute errors of relative humidity were 4%, 3% and 5% at the depths of 28 mm, 36 mm and 64 mm respectively. Moreover, the CHM model predicted the vapor pressure more accurate than the TH model, as shown in Figure 5.14. These results further verify the highly coupling effect of heat transfer and moisture transfer.

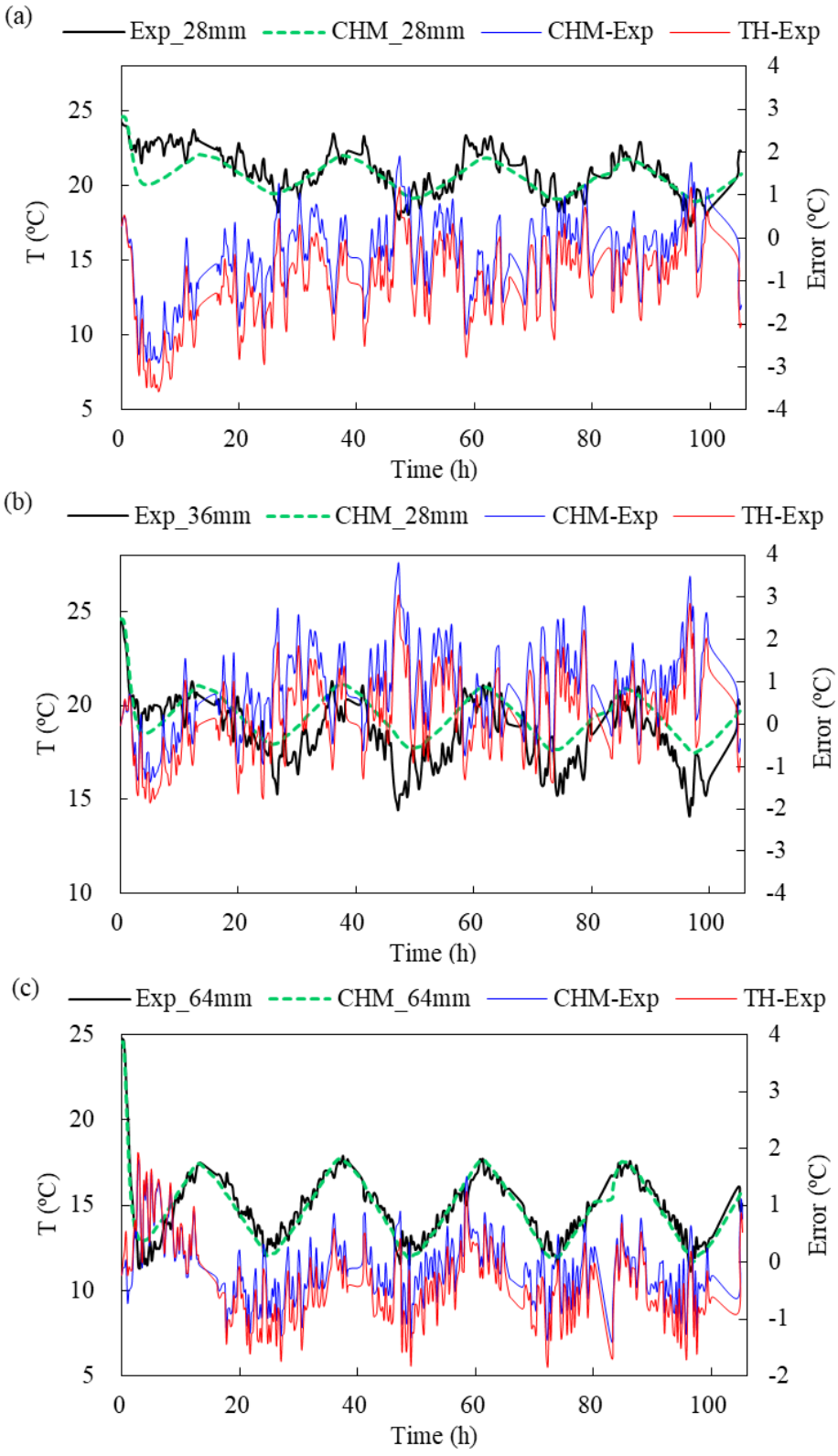

Figure 5.12. Temperature comparison of numerical results with experimental results variations at

different depths

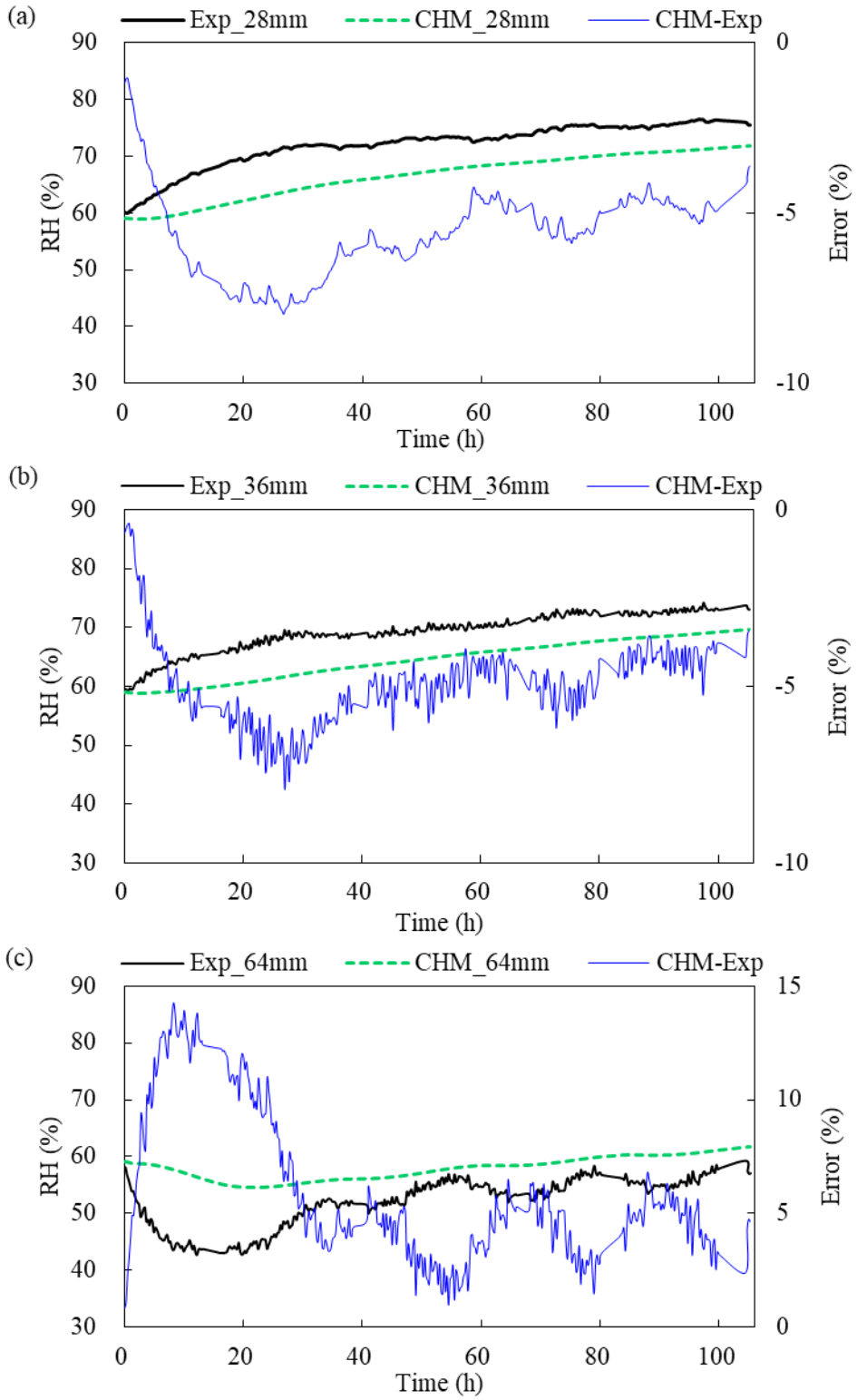

Figure 5.13. Relative humidity comparison of numerical results with experimental results

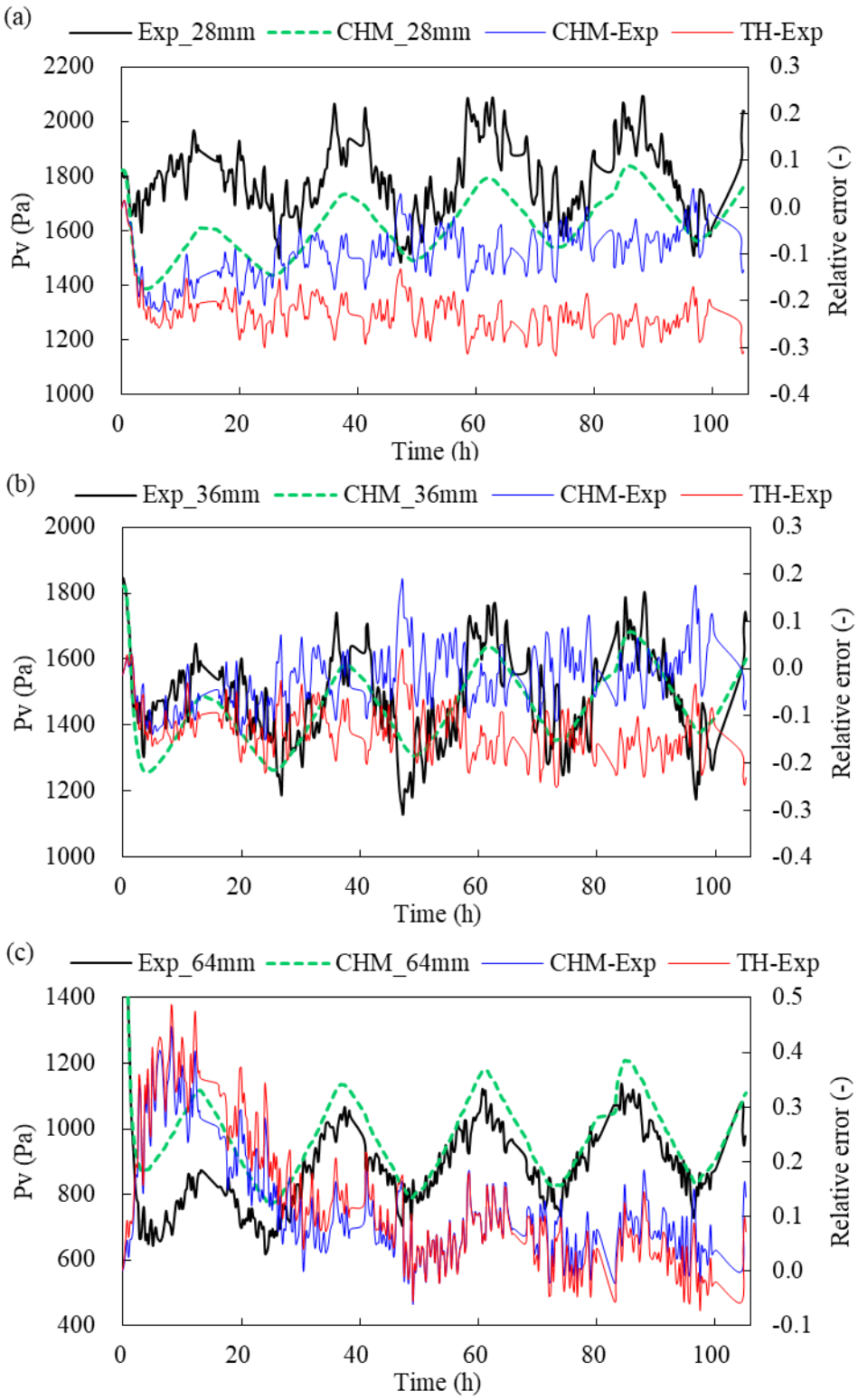

Figure 5.14. Vapor pressure comparison of numerical results with experimental results

Figure 5.15. shows the sensible, latent heat, total heat fluxes of interior surface predicted the CHM models and the sensible heat flux predicted by the TH model. The sensible heat flux was periodically fluctuated with the temperature. With the inter-model comparison, the sensible heat flux was overestimated by 11.3% by the TH model compared to the CHM model. The latent heat flux accounted for 37.7% of the total heat flux predicted by the CHM model. Therefore, the total heat flux was underestimated by 30.6%by the TH model compared to the CHM model. Figure 5.16 shows the vapor flux difference between the interior and exterior surfaces of the wall predicted by the CHM model, indicating its periodic water uptake and release.

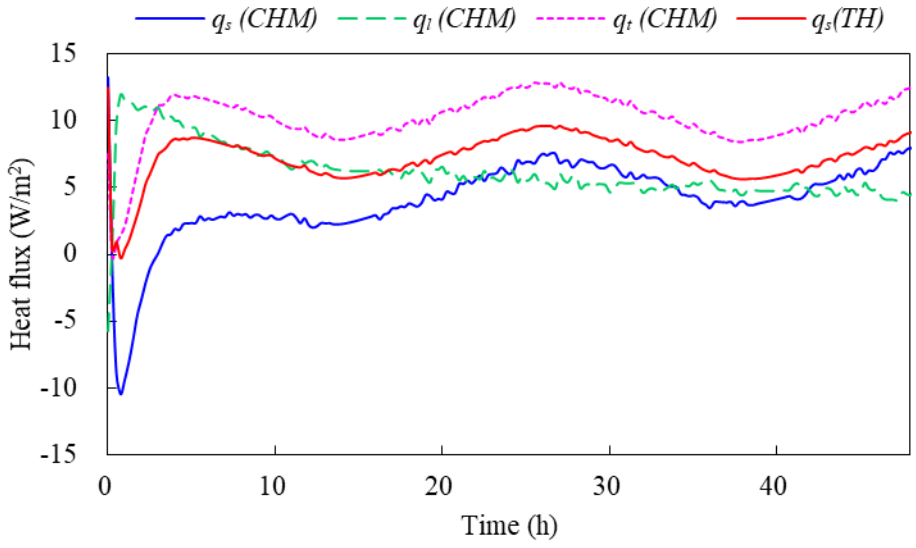

Figure 5.15. The heat fluxes through the interior surface predicted by the TH model and the CHM model

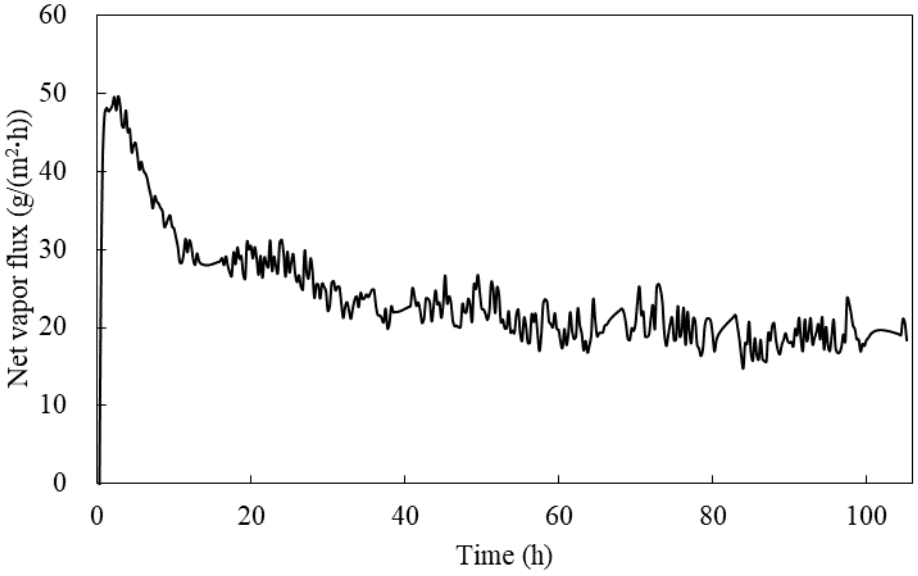

Figure 5.16. The vapor flux difference between the interior and exterior surfaces of the wall predicted by the CHM model

5.6. Conclusions

CHM models are usually used to simulate hygrothermal behaviour across the thickness of a material or an envelope in buildings. In this chapter, a CHM model was validated on a rice straw alginate panel based on the experimental measurements from Chapter 4. This model was solved using the finite element method embedded in the COMSOL Multiphysics software. The CHM model was compared with a transient heat transfer (TH) model to study the influence of moisture transport on the thermal behaviour of the wall. Results showed that the CHM model was more accurate to predict the thermal behaviour compared to the TH model. With inter-model comparison, the sensible heat flux in interior surface can be overestimated and the total heat flux in interior surface can be underestimated by the TH model compared to the CHM model.

6. Inverse liquid water permeability determination based on dynamic measurements and optimizers

6.1. Introduction

Although the better results obtained by the CHM model than the TH model, a gap between the measurements and predicted results by the CHM model can be observed, especially for the relative humidity. There are many reasons that affect the simulation accuracy. Several studies reported that using the material properties measured by standard methods and in steady state cannot completely reproduce the hygrothermal behaviour of the material subjected to dynamic conditions. Also, the uncertainty of material properties and boundary conditions will influence the numerical calculation results. More importantly, water vapor diffusion and liquid water transfer simultaneously exist in porous material. However, for the numerical calculations in

Chapter 5, the CHM model was simplified to a single-phase model, which only take the vapor diffusion into account. However, this simplification might underestimate the amount of moisture transport, especially for the high relative humidity.

Some authors attempt to determine the liquid water transfer coefficient in hygroscopic region from water vapor permeability measured by wet cup [147]. Also, the liquid water transfer coefficient of a material is typically predicted by capillary absorption coefficient, which is measured by a gravimetric method [148, 149]. Considering that the liquid water transfer coefficient was not measured in this thesis, the inverse parameter identification technique is applied for estimation of liquid water permeability K_l. This technique utilizes a hygrothermal model to inversely determine transport coefficients from measurements. Consequently, it is of great interest to monitor the temperature and relative humidity field by conducting dynamic experiment and apply different methods to inversely estimate the liquid water permeability of the rice straw alginate insulation material. Generally, an inverse problem can be regarded as an optimization problem to search the best solution to minimize the errors between the measurements and simulated results. In recent years, different algorithms and strategies have been employed to solve the inverse problem. Local search methods such as Levenberg-Marquart method [150], and global search method such as Particle Swarm Optimization [151] and Genetic Algorithm [151] are regularly used in literature.

This chapter aims to determine the liquid water permeability by the inverse analysis method based on the previous experiment under dynamic condition shown in Chapter 4. Different optimization algorithms including Fmincon, Particle Swarm Optimization and Genetic Algorithm are selected for searching the possible solutions of K_l. Moreover, the CHM model with the estimated K_l is compared with the CHM model with consideration of liquid water transfer. Furthermore, the estimated K_l is validated in

another experiment under non-isothermal condition in order to test its robustness.

6.2. Optimization algorithms

6.2.1. Fmincon

The Fmincon in MatLab optimization toolbox, is a kind of sequential quadratic programming algorithm, solving a quadratic programming subproblem at each iteration. It is a popular local search method which finds the constrained minimum of a scalar nonlinear function. This is in contrast to the commonly used Levenberg-Marquart algorithm which minimizes a sum of squares. Thus, the Fmincon was selected instead of the Levenberg-Marquart algorithm because of its ability to include boundary constraints. In this study, the interior point algorithm is selected in Fmincon, using adjoint sensitivities for evaluating the gradient of target function. In this study, the maximum iteration was set to 10.

6.2.2. Particle swarm optimization algorithm

The Particle Swarm Optimizer (PSO) is a stochastic search method activated by the unique social behaviour of some natural creatures such as collective movements of bird flocks and fish schools [152]. In this algorithm, the particles are described by their positions and velocities. The movement of the particles can be affected by their memory as well as the best particles found by all the particles. In this way, all the particles can share the knowledge of reasonable solutions.

The PSO algorithm has few hyperparameters and fast convergence. The velocity vector and the position vector of each particle i are denoted by $V_i = [v_{i1}, v_{i2}, ..., v_{iN}]$ and $X_i = [X_{i1}, X_{i2}, ..., X_{iN}]$. The particle i will update its velocity and position with the influence of previous best position of particle i, i.e., $pbest_i = [p_{i1}, p_{i2}, ..., p_{i3}]$ and the

best one in the whole population, i.e., *gbest* = [g_1, g_2, ..., g_N]. The V_i and X_i are firstly stochastically initialized and are updated according to equations as follows:

$$V_i^{k+1} = \omega \cdot V_i^k + c_1 \cdot rand_1 \cdot \left(pbest_i - X_i^k\right) + c_2 \cdot rand_2 \cdot \left(gbest - X_i^k\right) \quad (6.1)$$

$$X_i^{k+1} = X_i^k + V_i^{k+1} \quad (6.2)$$

Where ω is the inertia factor; c_1 is personal learning coefficient; and c_2 is global learning coefficient; c_1 and c_2 are set equal generally in this study to balance the effect of random factors; $rand_1$ and $rand_2$ are random numbers between 0 and 1. In this study, the particle size and generation size were set to 10.

6.2.3. Genetic algorithm

The Genetic Algorithm (GA) is a stochastic global search approach activated by evolutionary mechanism [153]. Compared to the other two algorithms, the GA is scarcely falls into the local optima despite of discontinuity, irregularity and noisy of the defined objective function. The GA first initializes a population, i.e., a set of individuals, which is randomly generated. For each generation, the individuals are sorted and selected by evaluating the objective function. Then the new individuals are generated based on the selection, crossover and mutation. In this study, the population size and generation size were set to 10.

6.3. Inverse analysis

The liquid water permeability K_l was regarded as an unknow property to be identified from the temperature and relative humidity variations at the three locations of the wall under dynamic condition, which were introduced in Chapter 4. Figure 6.1 shows the framework of the inverse identification.

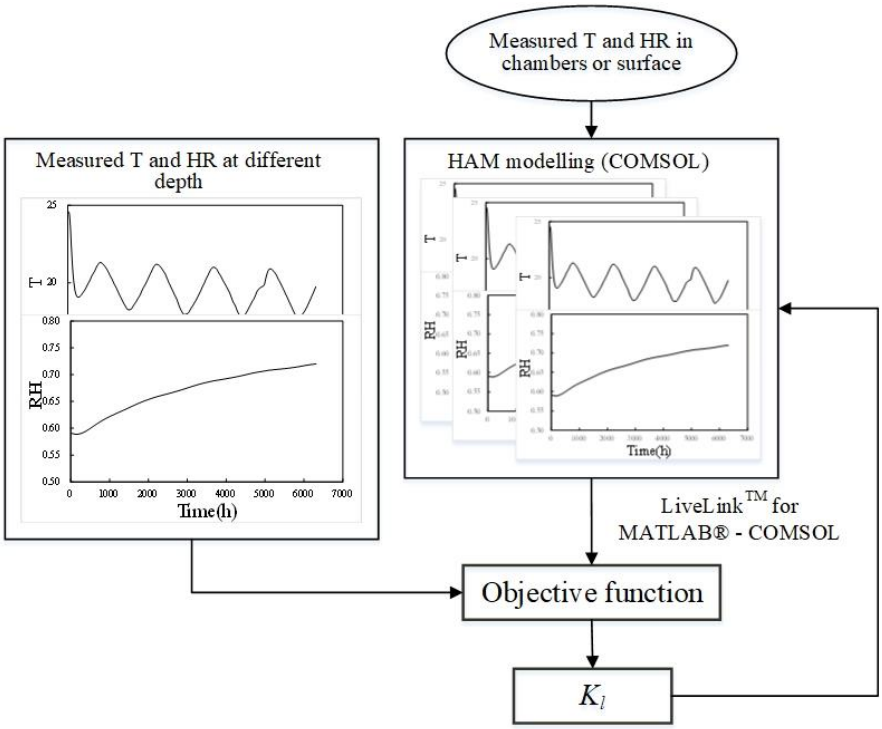

Figure 6.1. Parameter estimation workflow

Note that the K_l has a very wide range. According to the work of [144], the K_l of medium density fibreboard ranges from 0 to 1.17×10^{-16}. For simplicity, the K_l was assumed as a linear function of moisture content, which is as follows:

$$K_l = (a \cdot w) \cdot 10^{-17} \tag{6.3}$$

Where w (kg/m^3) represents the moisture content in the material; a represents the dimensionless parameter to be estimated with the range from 0 to 100;

For evaluating different solution, this study defined a multi-objective function as the sum of the squared error between measurements (including temperature and relative humidity) and simulated results by the CHM model:

$$f(a) = \sum_{n=1}^{N} \sum_{l=1}^{L} \left(\frac{y_{nl} - y_{nl}(a)}{\sigma_n} \right)^2 \tag{6.4}$$

Where y_{nl} represents l data points for each measured variable n (temperature and

relative humidity); $y_{nl}(a)$ represents the variable calculated from the direct CHM model inputting the estimated K_l.

Therefore, the expected parameter for the K_l can be obtained by minimizing the objective function as follows:

$$\min f(a) = \sum_{n=1}^{N} \sum_{l=1}^{L} \left(\frac{y_{nl} - y_{nl}(\theta)}{\sigma_n} \right)^2 \tag{6.5}$$

For convience, only the two cycles of the dynamic test were used for the parameter determination. Figure 6.2 illustrates the temperature and relative humidity at boundaries . Moreover, all the material properties required for the CHM model except for the K_l are shown in Table 5.2 in Chapter 5.

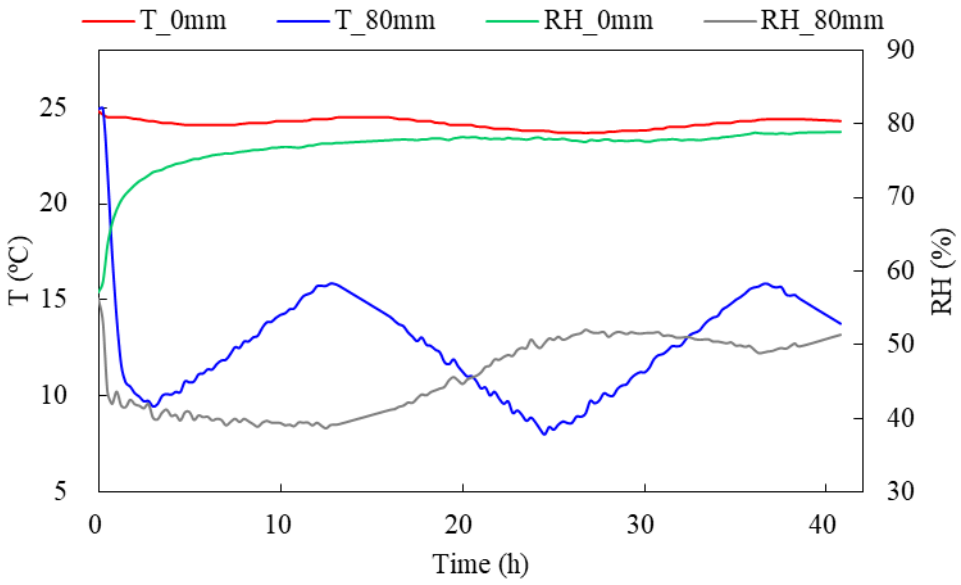

Figure 6.2. Boundary conditions for the dynamic test

6.4. Performance assessment metrics

For evaluating the modelling performance using the estimated K_l found by different optimization algorithms, this study employs two metrics, including the mean absolute error (MAE) and the root mean squared error (RMSE) [154]:

$$MAE = \frac{\sum_{t=1}^{N}|\widetilde{y_t}-y_t|}{N} \tag{6.6}$$

$$RMSE = \sqrt{\frac{\sum_{t=1}^{N}(\widetilde{y_t}-y_t)^2}{N}} \tag{6.7}$$

Where y_t is the measured temperature or relative humidity at different depths; $\widetilde{y_t}$ is the simulated temperature or relative humidity at different depths; t is the timestep; N is the maximum timestep.

6.5. Results of estimated property

Table 6.1 shows the liquid water permeability K_l searched by the different optimization algorithms, i.e., Fmincon, PSO and GA. As it can be seen, similar values of K_l were obtained by the three optimization algorithms. To assess the effectiveness of the estimated K_l, the simulation results using these K_l values were compared with the results of the CHM model ignoring liquid transfer.

Table 6.1 Liquid water permeability determined by different optimization algorithms

Optimization algorithm	Liquid water permeability Kl (kg/(m·s·Pa)
Fmincon	3.4441·10-16
PSO	3.4071·10-16
GA	3.7176·10-16

Table 6.2 summarized the errors of temperature and relative humidity predicted by the models with and without liquid water transfer. Consistent with the previous results,

this table presented a negligible effect of K_l determined by different optimization algorithms on temperature and relative humidity predictions. Also, compared with the CHM model ignoring the liquid water transfer, the three models taking liquid transport into account highly reduced the errors of predicting the relative humdity for all the positions. According to the MAE metric, the CHMWL models decreased the error by 61%, 57% and 8% for the depths of 28 mm, 36 mm and 64 mm, respectively. The minor improvement at the depth of 64 mm is attributed to the low relative humidity. At this position, the moisture transport is mainly driven by the vapor pressure companied with very small capilary pressure. And thus, by applying the linear function as moisture content, the liquid water transfer can be overestimated, leading to errors on prediction of relative humidity. Among the models, the difference in temperature error is actually not significant.

Table 6.2 Performance comparison between the numerical models with and without liquid water transfer under dynamic condition

Position		x = 28 mm		x = 36 mm		x = 64 mm	
Parameter	Model	MAE	RMSE	MAE	RMSE	MAE	RMSE
T (ºC)	CHM	0.79	1.03	1.07	1.31	0.46	0.58
	CHMWL+Fmincon	0.83	1.08	0.99	1.22	0.51	0.66
	CHMWL+PSO	0.83	1.08	0.99	1.22	0.51	0.66
	CHMWL+GA	0.83	1.08	0.99	1.22	0.51	0.66
RH (%)	CHM	5.6	5.8	4.9	5.1	5.9	6.7
	CHMWL+Fmincon	2.3	2.4	2.1	2.4	5.4	5.8
	CHMWL+PSO	2.2	2.4	2.1	2.3	5.4	5.8
	CHMWL+GA	2.2	2.4	2.1	2.3	5.4	5.8

Note: CHM denotes the CHM model ignoring liquid transfer, CHMWL+Fmincon, CHMWL+PSO and CHMWL+GA denotes the CHMmodel taking liquid transfer into account, and the liquid water permeability are searched and detremined by Fmincon, PSO and GA optimization algorithms, respectively

For more intuitive comparison, Figure 6.3 illustrates the relative humidity variations at different depths predicted by the CHM model and the CHMWL+PSO

model together with the measurements. As it can be seen, compared with the CHM model, the relative humidity curve predicted by the CHMWL+PSO was closer to the experimental curve for the depths of 28 mm and 36 mm. Additionally, at the depth of 64 mm, despite of the higher relative humidity predicted by the CHMWL+PSO, this model can track the periodic fluctuations. Therefore, it can be concluded that the inversely determined liquid water permeability contributes to the numerical calculations.

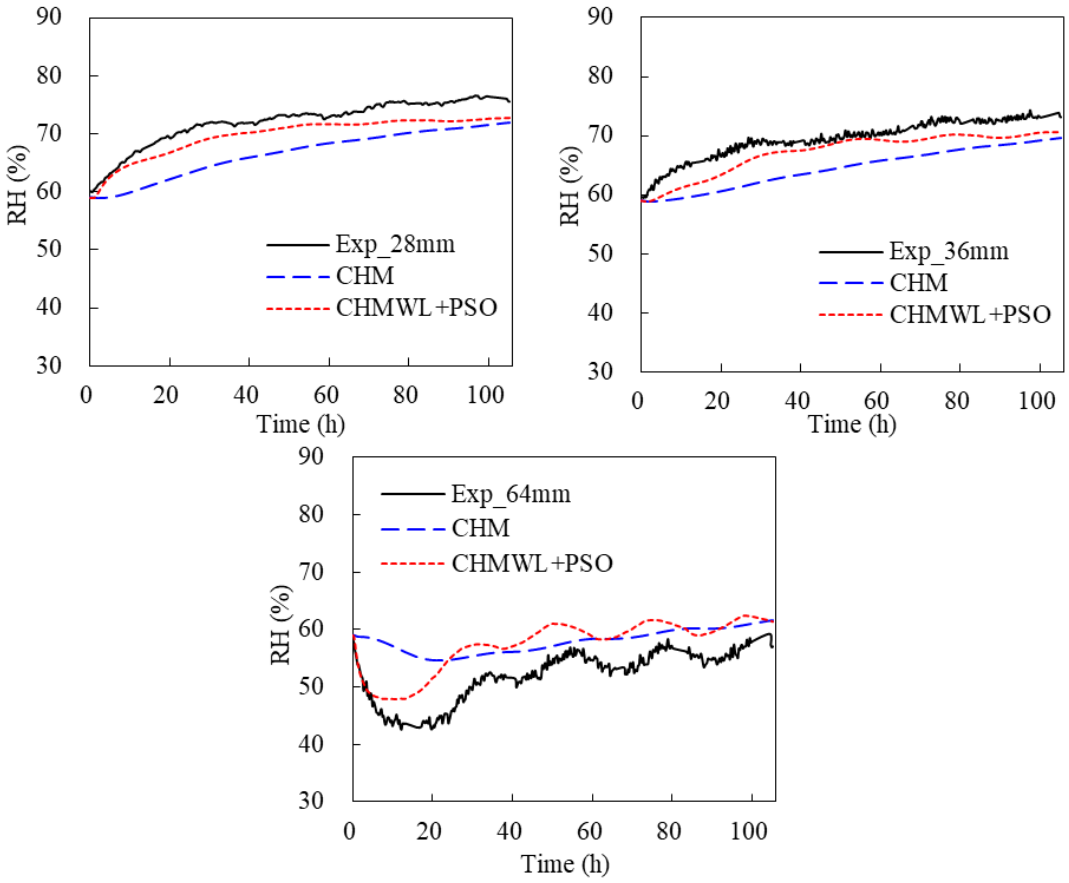

Figure 6.3. Comparison the relative humidity predicted by the CHM and CHMWL+PSO models

Figure 6.4 shows the sensible heat flux (q_s) through the interior surface predicted by the CHM and CHMWL+PSO models. A small discrepancy of the sensible heat flux can be observed between these two models, which is consistent with the results of temperature simulation. Figure 6.5 shows the vapor, liquid water, total moisture fluxes

of interior surface predicted the CHMWL+PSO model and the vapor flux predicted by the CHM model. It is visible that the moisture flux predicted by the CHWL+PSO model was much higher than that predicted by the CHM model.

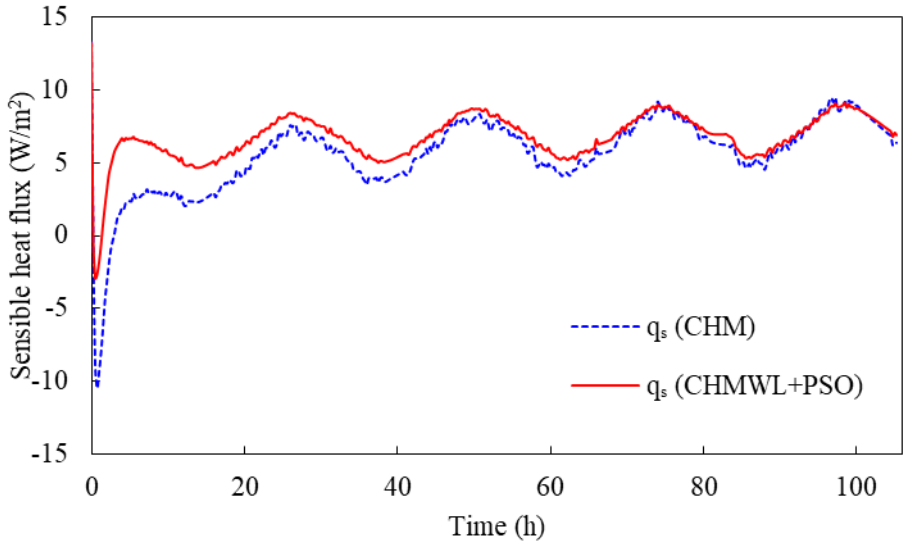

Figure 6.4. The sensible heat flux (q_s) through the interior surface predicted by the CHM model and the CHMWL+PSO model

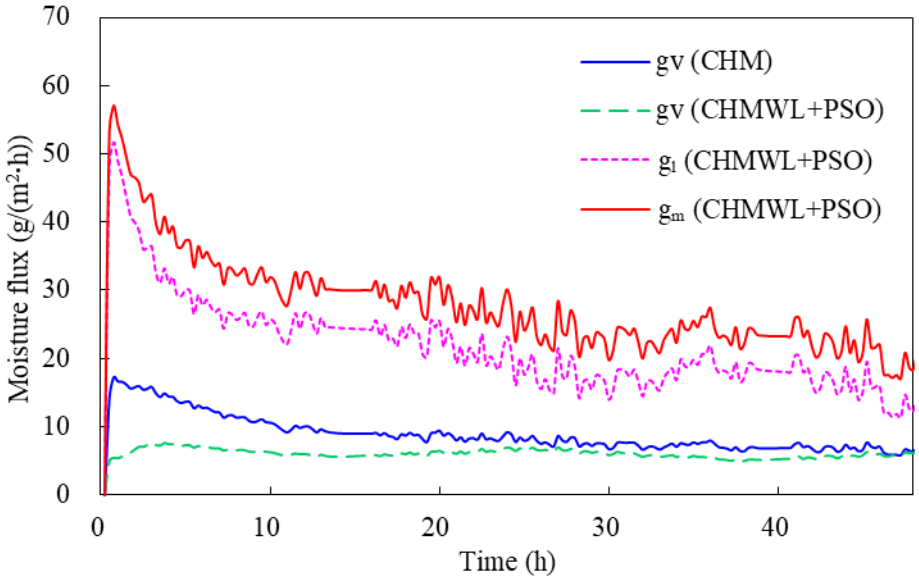

Figure 6.5. The moisture fluxes through the interior surface predicted by the CHM model and the CHMWL+PSO model

6.6. Validation of estimated property

In the previous sections, the K_l has been estimated by the measurements under the dynamic test. In this section, the determined K_l was further validated by another experiment where the wall was subjected to non-isothermal conditions in order to test its robustness. Table 6.3 and Figure 6.6 show the results of temperature and relative humidity simulated by the CHM and CHMWL+PSO models. These results are consistent with the results in Section 6.5. From Figure 6.6, at the depths of 28 mm and 36 mm, the simulated curves of relative humidity by the CHMWL+PSO model were closer to the experimental curves compared to the simulated curved by the CHM model, especially in the transient state. This is a useful information because unsteady process is usually existed as building envelops are normally exposed to fluctuated conditions in real environments. Therefore, the determined K_l by the experiment under the dynamic condition can be used to reproduce the transport of liquid water in the wall when exposed to different boundary conditions. Nevertheless, the assumption of K_l as linear function of moisture content is difficult to completely describe the transport of liquid water across the thickness of the wall when exposed to different boundary conditions. In the future study, appropriate functions for liquid water permeability will be chosen to simulate realistic moisture behaviour of the material.

Table 6.3 Performance comparison between the numerical models with and without liquid water transfer under non-isothermal condition

Position		x =28 mm		x =36 mm		x =64 mm	
Parameter	Model	MAE	RMSE	MAE	RMSE	MAE	RMSE
T (ºC)	CHM	1.69	1.97	1.03	1.38	0.50	0.62
	CHMWL+PSO	1.99	2.21	1.13	1.43	0.52	0.65
RH (%)	CHM	8.1	8.4	9.4	9.9	3.8	4.8
	CHMWL+PSO	0.9	1.0	2.4	2.5	6.6	6.8

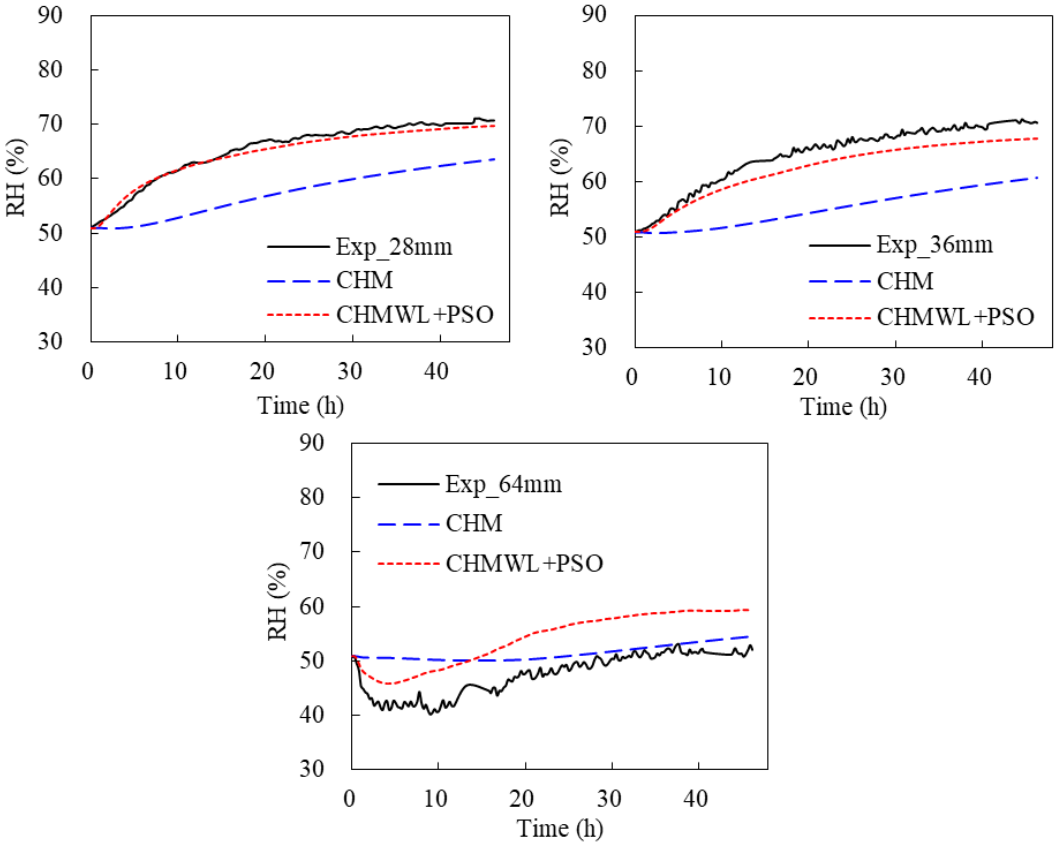

Figure 6.6. Comparison of numerical results on relative humidity simulated by the CHM model and CHMWL+PSO model under non-isothermal condition

6.7. Conclusions

The CHM model is not reliable when the liquid water transport is neglected especially for exposing the wall to the environment at high RH. Considering that the liquid water coefficients are unknown, the K_l was estimated in this chapter by applying inverse identification technique. The temperature and relative humidity variations at the three locations of the wall under dynamic condition (as shown in Chapter 4) was adopted. Different optimization algorithms including Fmincon, PSO and GA were compared. Moreover, the estimated K_l was further validated in the non-isothermal condition. Results showed that different optimization algorithms had a neglible effect

on the values of K_l, and thus exerting neglected impact on temperature and relative humidity predictions. Results also showed that compared with the CHM model ignoring the liquid water transfer, the CHM model with the estimated K_l highly reduced the errors of predicting the relative humdity for all the positions.

7. Conclusions and future work

7.1. Conclusions

Conversion agricultural straw waste to building thermal insulation products is a promising high-valued resource utilization approach with the benefits of energy efficiency and decarbonization. A category of straw insulation attracting attention is straw composite, in which the straw fibres are usually moulded with alternative binders, including polyester fibres, synthetic resins and inorganic cementing materials. These binders, however, leads to an increase in embodied energy use as well as an issue of waste disposal as they are indecomposable. This thesis aims to develop and characterize fully bio-sourced insulation materials from rice straw and natural binders in both the material scale and wall scale.

One of the main objectives of this thesis is to develop a new thermal insulation material from rice straw and natura binders that presents with competitive hygrothermal

properties. Two natural polysaccharides, i.e., sodium alginate and chitosan were chosen as binders as they have the properties such as being nontoxic, adhesive, biocompatible, biodegradable with low cost. Considering that using sodium alginate as the binder may suffer from water solubility issue as sodium alginate is water soluble at ambient condition, a crosslinking method was proposed to prepare water insoluble insulation material from rice straw fibres and sodium alginate. The water solubility test was used to test the solubility of the developed rice straw alginate insulation material. The results showed that the proposed crosslinking method is able to solve the water solubility issue of the insulation materials using sodium alginate as a binder. After the water solubility test, two types of rice straw fibres with different fibre size distribution, two different binders and three different percentages of binder were applied to produce experimental insulation material. A total of twelve different formulations were obtained. The resulting materials were evaluated and compared in terms of their thermal insulation properties, moisture properties and mould growth. All the composites can be considered as insulators with thermal conductivity values ranging from 0.038 to 0.047 W/(m·K) at dry state. A decrease of fibre size and an increase of binder ratio resulted in an increase in the thermal conductivity of the composites. Moreover, the thermal conductivity of these composites showed a lower range of values when compared to existing straw insulating building materials. the water vapor resistance factor of chitosan-based composites showed the higher values than those of alginate-based composites. Smaller fibre size and larger binder ratio also resulted in higher water vapor resistance factors. Binders, even though in small amount, have an influence on the sorption isotherm and water absorption. The alginate-based composites had the higher moisture adsorption capacity than the chitosan-based composites. However, the fibre type and binder ratio seemed to have negligible influence on the materials' adsorption capacity in this study. The binder type and the relative humidity had the impacts on the types, amount and

speed of mould contaminated on the surface of the composites.

On the basis of the above outcomes, the hygrothermal behaviour of the rice straw alginate insulation material was investigated at the wall scale. A bi-climatic setup was used to apply the isothermal, non-isothermal and dynamic boundary conditions. The relative humidity in both sides was always kept steady as it was controlled by a saturated salt solution for internal environment and a desiccant for external environment. For all the configurations, the hygrothermal response of the wall was monitored by temperature/moisture sensors installed at various depths across the wall thickness. The results under the isothermal condition revealed that the moisture transfer has explicit impact on the temperature changes due to moisture sorption. The condensation/evaporation of water vapor related to the moisture storage and moisture diffusion induced the increase/decrease of temperature. The results under the non-isothermal condition indicated that the moisture transport can be affected by temperature gradient. From the dynamic test, the material presented a high thermal phase shift comparable to wood fibre insulation, contributing to a comfortable indoor environment. The material demonstrated a good heat capacity in response to external temperature oscillations. Besides, the obtained results indicated that the material is an interesting bio-sourced material for moisture uptake and release.

Coupled heat and moisture transfer (CHM) models are usually used to simulate hygrothermal behaviour across the thickness of a material or an envelope in buildings. a CHM model was validated on the rice straw alginate insulation wall panel based on experimental measurements from Chapter 4. It was implemented in a commercial Multiphysics software in order to solve the problem numerically with the finite element method. The CHM model was compared with a transient heat transfer (TH) model to study the influence of moisture transport on the thermal behaviour of the wall. The

results showed that the CHM model was more accurate to predict the thermal behaviour compared to the TH model. With inter-model comparison, the sensible heat flux in interior surface can be overestimated and the total heat flux in interior surface can be underestimated when ignoring moisture transfer for numerical calculations. However, a gap was observed between experimental results and simulated results for relative humidity. From the numerical point of view, the gap might be caused by the simplifications in the model, such as the ignoration of liquid water transfer.

The liquid water permeability K_l of the material was inversely estimated by using the previous measurements under dynamic conditions. Different optimization algorithms including Fmincon, PSO and GA were compared. Moreover, the estimated K_l was further validated in the non-isothermal condition. The results showed that different optimization algorithms had a neglible effect on the values of K_l, and thus exerting neglected impact on temperature and relative humidity predictions. The results also showed that compared with the CHM model ignoring the liquid water transfer, the CHM model with the estimated K_l highly reduced the errors of predicting the relative humdity for all the positions.

7.2. Future work

The immersion procedure in the proposed crosslinking method required a further oven-drying process, which lead to the energy consumption. In the future, a modified procedure can be investigated to reduce the drying time and improve the adaptability to industries, such as the application of spray technique. The component and microstructure of the developed composite materials can be investigated by chemical analysis and image analysis to understand the mechanisms of the influence of the different factors on the hygrothermal properties. Moreover, the durability of the

composite materials should be further studied, especially for the bonding strength with the consideration of moisture content and fire resistance. Also, the mould growth of the composite materials should be investigated for a longer period, such as one-year.

The assumption of K_l as linear function of moisture content is difficult to completely describe the transport of liquid water across the thickness of the wall when exposed to different boundary conditions. For example, the moisture content of the material can be overestimated in low RH. In the future study, appropriate functions for liquid water permeability will be chosen to simulate more realistic hygrothermal behaviour of the composite materials. Further work on the identification of multiple parameters, such as water vapor permeability and sorption isotherm, will be conducted. Different optimization algorithms or even hybrid algorithms will be further validated on the more complex inverse problem.

List of papers

[1] Y. Zhou, A. Trabelsi, M. El Mankibi, A review on the properties of straw insulation for buildings, Construction and Building Materials 330 (2022) 127215.

[2] Y. Zhou, A. Trabelsi, M. El Mankibi, Development and characterization of thermal insulation materials based on rice straw and natural binder, CLIMA 2022 conference, 2022.

[3] Y. Zhou, A. Trabelsi, M. El Mankibi, Development and characterization of insulation materials from rice straw and natural binders (submitted)

References

[1] bp Statistical Review of World Energy 71st edition, 2022.

[2] Abu-Jdayil B., Mourad A.-H., Hittini W., et al., Traditional, state-of-the-art and renewable thermal building insulation materials: An overview, Construction and Building Materials 214 (2019) 709-735.

[3] Tettey U.Y.A., Dodoo A., Gustavsson L., Effects of different insulation materials on primary energy and CO2 emission of a multi-storey residential building, Energy and buildings 82 (2014) 369-377.

[4] Hassan S.S., Williams G.A., Jaiswal A.K., Emerging technologies for the pretreatment of lignocellulosic biomass, Bioresource technology 262 (2018) 310-318.

[5] Li L., Wang Y., Zhang Q., et al., Wheat straw burning and its associated impacts on Beijing air quality, Science in China Series D: Earth Sciences 51(3) (2008) 403-414.

[6] Zhao J., Li S., Life cycle cost assessment and multi-criteria decision analysis of environment-friendly building insulation materials-A review, Energy and Buildings (2021) 111582.

[7] Binod P., Sindhu R., Singhania R.R., et al., Bioethanol production from rice straw: an overview, Bioresource technology 101(13) (2010) 4767-4774.

[8] FAOSTAT, Food and Agriculture Organization of the United Nations, 2020. https://www.fao.org/faostat/en/#data/QCL.

[9] Gummert M., Hung N.V., Chivenge P., et al., Sustainable rice straw management, Springer Nature2020.

[10] Gangil S., Bhargav V.K., Influences of binderless briquetting stresses on intrinsic bioconstituents of rice straw based solid biofuel, Renewable Energy 133 (2019) 462-469.

[11] Ai P., Chen M., Ran Y., et al., Digestate recirculation through co-digestion with rice straw: Towards high biogas production and efficient waste recycling, Journal of Cleaner Production 263 (2020) 121441.

[12] Kogo T., Yoshida Y., Koganei K., et al., Production of rice straw hydrolysis enzymes by the fungi Trichoderma reesei and Humicola insolens using rice straw as a carbon source, Bioresource technology 233 (2017) 67-73.

[13] Wei K., Lv C., Chen M., et al., Development and performance evaluation of a new thermal insulation material from rice straw using high frequency hot-pressing, Energy and Buildings 87 (2015) 116-122.

[14] EN12664, Thermal performance of building materials and products-Determination of thermal resistance by means of guarded hot plate and heat flow meter methods-Dry and moist products of medium and low thermal resistance, British Standard, 2001.

[15] EN12667, Thermal performance of building materials and products-Determination of thermal resistance by means of guarded hot plate and heat flow meter methods-Products of high and medium thermal resistance, British Standard, 2001.

[16] EN12939, Thermal performance of building materials and products-Determination of thermal resistance by means of guarded hot plate and heat flow meter methods-Thick products of high and medium thermal resistance, British Standard, 2001.

[17] C518 A., Standard Test Method for Steady-State Thermal Transmission Properties by Means of the Heat Flow Meter Apparatus, ASTM International, West Conshohocken, PA, 2017.

[18] 11357 I., Plastics-Differential scanning calorimetry (DSC)-Part 1: General principles, International Organization for Standadization, 2016.

[19] 22007 I., Plastics-Determination of thermal conductivity and thermal diffusivity,

International Organization for Standadization, 2017.

[20] 16 A.D.-. Standard Test Method for Measurement of Thermal Effusivity of Fabrics Using a Modified Transient Plane Source (MTPS) Instrument, ASTM International, 2016.

[21] 12571 E.I., Hygrothermal performance of building materials and products-Determination of hygroscopic sorption properties, British Standard, 2013.

[22] 12086 E.I., Thermal insulating products for building applications-Determination of water vapour transmission properties, British Standard, 2013.

[23] 12572 E.I., Hygrothermal performance of building materials and products-Determination of water vapour transmission properties-Cup method, British Standard, 2016.

[24] 1470-1 J.A., Determination of water vapour adsorption/desorption properties for building materials-Part 1: Response to humidity variation, Japanese Industrial Standard, 2002.

[25] Rode C., Peuhkuri R., Lone H., et al., Moisture buffering of building materials, Technical University of Denmark DTU2006.

[26] 24353 I., Hygrothermal performance of building materials and products — Determination of moisture adsorption/desorption properties in response to humidity variation, International Organization for Standadization, 2008.

[27] 51-071 N., Determination of burning behaviour by oxygen index, Association Francaise de Normalisation, 1985.

[28] 29767 I., Thermal insulating products for building applications-Determination of short-term water absorption by partial immersion, International Organization for Standadization, 2019.

[29] 12087 E.I., Thermal insulating products for building applications-Determination of long term water absorption by immersion, British Standard, 2013.

[30] Thomson A., Walker P., Durability characteristics of straw bales in building envelopes, Construction and Building Materials 68 (2014) 135-141.

[31] Johansson P., Ekstrand-Tobin A., Svensson T., et al., Laboratory study to determine the critical moisture level for mould growth on building materials, International

Biodeterioration & Biodegradation 73 (2012) 23-32.

[32] E24-16 A., Laboratory Method for Evaluating the Mold Resistance of Wood-based Materials: Mold Chamber Test, American Wood Protection Association, 2016.

[33] D3273 A., Standard Test Method for Resistance to Growth of Mold on the Surface of Interior Coatings in an Environmental Chamber, ASTM International, 2012.

[34] 846 B.E.I., Plastics. Evaluation of the action of microorganisms, British Standards Institute, 1997.

[35] Ghaffar S.H., Fan M., Structural analysis for lignin characteristics in biomass straw, Biomass and bioenergy 57 (2013) 264-279.

[36] Titiloye J.O., Bakar M.S.A., Odetoye T.E., Thermochemical characterisation of agricultural wastes from West Africa, Industrial crops and products 47 (2013) 199-203.

[37] Ghaffar S., Straw fibre-based construction materials, Advanced High Strength Natural Fibre Composites in Construction, Elsevier2017, pp. 257-283.

[38] Stamm A.J., Wood and cellulose science, Wood and cellulose science. (1964).

[39] Yu H., Liu R., Shen D., et al., Arrangement of cellulose microfibrils in the wheat straw cell wall, Carbohydrate polymers 72(1) (2008) 122-127.

[40] Yin X., Lawrence M., Maskell D., et al., Comparative micro-structure and sorption isotherms of rice straw and wheat straw, Energy and Buildings 173 (2018) 11-18.

[41] R.-C S., Tomkinson J., Appendix 1. Essential Guides for Isolation/Purification of polysaccharides, (2000).

[42] Sun R., Cereal straw as a resource for sustainable biomaterials and biofuels: chemistry, extractives, lignins, hemicelluloses and cellulose, Elsevier2010.

[43] Platt S., Maskell D., Walker P., et al., Manufacture and characterisation of prototype straw bale insulation products, Construction and Building Materials 262 (2020) 120035.

[44] Belayachi N., Hoxha D., Slaimia M., Impact of accelerated climatic aging on the behavior of gypsum plaster-straw material for building thermal insulation, Construction and Building Materials 125 (2016) 912-918.

[45] Ali M., Alabdulkarem A., Nuhait A., et al., Thermal and acoustic characteristics of

novel thermal insulating materials made of Eucalyptus Globulus leaves and wheat straw fibers, Journal of Building Engineering 32 (2020) 101452.

[46] Bakatovich A., Davydenko N., Gaspar F., Thermal insulating plates produced on the basis of vegetable agricultural waste, Energy and Buildings 180 (2018) 72-82.

[47] Lacoste C., El Hage R., Bergeret A., et al., Sodium alginate adhesives as binders in wood fibers/textile waste fibers biocomposites for building insulation, Carbohydrate polymers 184 (2018) 1-8.

[48] Evon P., Vandenbossche V., Pontalier P.-Y., et al., New thermal insulation fiberboards from cake generated during biorefinery of sunflower whole plant in a twin-screw extruder, Industrial Crops and Products 52 (2014) 354-362.

[49] Zhou X.-y., Zheng F., Li H.-g., et al., An environment-friendly thermal insulation material from cotton stalk fibers, Energy and Buildings 42(7) (2010) 1070-1074.

[50] Ashour T., The use of renewable agricultural by-products as building materials, Work 2 (2003) 013-2467034.

[51] Costes J.-P., Evrard A., Biot B., et al., Thermal Conductivity of Straw Bales: Full Size Measurements Considering the Direction of the Heat Flow, Buildings 7(4) (2017) 11.

[52] Shea A., Wall K., Walker P., Evaluation of the thermal performance of an innovative prefabricated natural plant fibre building system, Building Services Engineering Research and Technology 34(4) (2012) 369-380.

[53] Conti L., Barbari M., Monti M., Steady-state thermal properties of rectangular straw-bales (RSB) for building, Buildings 6(4) (2016) 44.

[54] Andersen B.M., Munch-Andersen J., Halmballer og muslinger som isoleringsmaterialer, Sampling and testing report, Danish Building Research Institute (2001).

[55] Marques B., Tadeu A., Almeida J., et al., Characterization of sustainable building walls made from rice straw bales, Journal of Building Engineering (2019) 101041.

[56] Reif M., Zach J., Hroudová J., Studying the properties of particulate insulating materials on natural basis, Procedia Engineering 151 (2016) 368-374.

[57] Cascone S., Evola G., Gagliano A., et al., Laboratory and in-situ measurements for

thermal and acoustic performance of straw bales, Sustainability 11(20) (2019) 5592.

[58] VĖJELIENĖ J., Gailius A., VĖJELIS S., et al., Evaluation of structure influence on thermal conductivity of thermal insulating materials from renewable resources, Materials Science 17(2) (2011) 208-212.

[59] Vėjelienė J., Processed Straw as Effective Thermal Insulation for Building Envelope Constructions, Engineering Structures and Technologies 4(3) (2012) 96-103.

[60] Douzane O., Promis G., Roucoult J.-M., et al., Hygrothermal performance of a straw bale building: In situ and laboratory investigations, Journal of Building Engineering 8 (2016) 91-98.

[61] Strohballenbau F., Thermal performance: strawbale building research development 2003 – 2009, Beetzendorf, Germany: FASBA (2009).

[62] Sabapathy K.A., Gedupudi S., Straw bale based constructions: Measurement of effective thermal transport properties, Construction and Building Materials 198 (2019) 182-194.

[63] Mehravar M., Veshkini A., Veiseh S., et al., Physical Properties of Straw Bale and its Effect on Building Energy Conservation and Carbon Emissions in Different Climatic Regions of Iran, Energy and Buildings (2021) 111559.

[64] Cornaro C., Zanella V., Robazza P., et al., An innovative straw bale wall package for sustainable buildings: experimental characterization, energy and environmental performance assessment, Energy and Buildings 208 (2020) 109636.

[65] DIBt D.I.f.B., Thermal insulation made of straw bales, (2017).

[66] Volf M., Diviš J., Havlík F., Thermal, moisture and biological behaviour of natural insulating materials, Energy Procedia 78 (2015) 1599-1604.

[67] Goodhew S., Griffiths R., Sustainable earth walls to meet the building regulations, Energy and Buildings 37(5) (2005) 451-459.

[68] Ashour T., Georg H., Wu W., Performance of straw bale wall: A case of study, Energy and Buildings 43(8) (2011) 1960-1967.

[69] Christian J., Desjarlais O., Stovall P., Straw-bale wall hot box test results and analysis, ASRAE Conf., Florida, 1998.

[70] McCabe J., The thermal resistivity of straw bales for construction, Unpublished

Master’s thesis. Department Nuclear Engineering University of Arizona, Tucson, AZ (1993).

[71] Hedlin C.P., Sorption isotherms of five types of grain straw at 70 F, National Research Council of Canada, Division of Building Research1967.

[72] Perry Robert H., Green Don W., Maloney James O., Perry’s chemical engineers’ handbook, Mc Graw-Hills New York (1997) 56-64.

[73] Lawrence M., Heath A., Walker P., Determining moisture levels in straw bale construction, Construction and Building Materials 23(8) (2009) 2763-2768.

[74] Carfrae J., The moisture performance of straw bale construction in a temperate maritime climate, (2011).

[75] Carfrae J., De Wilde P., Littlewood J., et al., Development of a cost effective probe for the long term monitoring of straw bale buildings, Building and Environment 46(1) (2011) 156-164.

[76] Lebed A., Augaitis N., Research of physical properties of straw for building panels, Int. J. Eng. Sci. Invention 6(5) (2017) 9-14.

[77] Hofbauer W., Breuer K., Krueger N., et al., Toxic mould versus façade-jungle – a comparison of undesirable biological growth on indoor surfaces and outer building coatings, Proceedings of the 10th International Conference on Indoor Air Quality and Climate – Indoor Air 2005, 2005, pp. 2450-2454.

[78] Hofbauer W., Kreuger N., Breuer K., et al., Mould resistance assessment of building materials – Material specific isoplethsystems for practical application, Indoor Air (2008) 17-22.

[79] Summers M.D., Blunk S.L., Jenkins B.M., How straw decomposes: Implications for straw bale construction, Ecological Building Network (2003).

[80] Steen A.S., Steen B., Bainbridge D., The straw bale house, Chelsea Green Publishing1994.

[81] Robinson J., Aoun H.K., Davison M., Determining moisture levels in straw bale construction, Procedia engineering 171 (2017) 1526-1534.

[82] Ashour T., Wieland H., Georg H., et al., The influence of natural reinforcement fibres on insulation values of earth plaster for straw bale buildings, Materials & Design

31(10) (2010) 4676-4685.

[83] Ren J., Zhao Z., Zhang J., et al., Study on the hygrothermal properties of a Chinese solar greenhouse with a straw block north wall, Energy and Buildings 193 (2019) 127-138.

[84] Binici H., Aksogan O., Demirhan C., Mechanical, thermal and acoustical characterizations of an insulation composite made of bio-based materials, Sustainable Cities and Society 20 (2016) 17-26.

[85] Labat M., Magniont C., Oudhof N., et al., From the experimental characterization of the hygrothermal properties of straw-clay mixtures to the numerical assessment of their buffering potential, Building and Environment 97 (2016) 69-81.

[86] Brouard Y., Belayachi N., Hoxha D., et al., Mechanical and hygrothermal behavior of clay – Sunflower (Helianthus annuus) and rape straw (Brassica napus) plaster bio-composites for building insulation, Construction and Building Materials 161 (2018) 196-207.

[87] Ismail B., Belayachi N., Hoxha D., Optimizing performance of insulation materials based on wheat straw, lime and gypsum plaster composites using natural additives, Construction and Building Materials 254 (2020) 118959.

[88] Mariana P., Antonia N., Jaume A., et al., Characterization of thermal insulation materials developed with crop wastes and natural binders, WSB 14 Barcelona Sustainable Building, 2014, pp. 188-1-188-10.

[89] Palumbo M., Formosa J., Lacasta A.M., Thermal degradation and fire behaviour of thermal insulation materials based on food crop by-products, Construction and Building Materials 79 (2015) 34-39.

[90] Tůmová E., Drochytka R., Černý V., et al., Development of organic and biodegradable insulating material for ETICS, Procedia engineering 195 (2017) 81-87.

[91] Rojas C., Cea M., Iriarte A., et al., Thermal insulation materials based on agricultural residual wheat straw and corn husk biomass, for application in sustainable buildings, Sustainable Materials and Technologies 20 (2019) e00102.

[92] Liuzzi S., Rubino C., Martellotta F., et al., Characterization of biomass-based materials for building applications: The case of straw and olive tree waste, Industrial Crops and Products 147 (2020) 112229.

[93] Rahim M., Douzane O., Le A.T., et al., Characterization and comparison of hygric properties of rape straw concrete and hemp concrete, Construction and Building Materials 102 (2016) 679-687.

[94] Belayachi N., Hoxha D., Redikutseva I., Etude Comparative du comportement hygrothermique des matériaux à base de fibres végétales, Rencontres Universitaires de Génie Civil, 2015.

[95] Palumbo M., Lacasta A.M., Holcroft N., et al., Determination of hygrothermal parameters of experimental and commercial bio-based insulation materials, Construction and Building Materials 124 (2016) 269-275.

[96] Liuzzi S., Rigante S., Ruggiero F., et al., Straw based materials for building retrofitting and energy efficiency, Key Engineering Materials, Trans Tech Publ, 2016, pp. 50-63.

[97] Ratiarisoa R.V., Magniont C., Ginestet S., et al., Assessment of distilled lavender stalks as bioaggregate for building materials: Hygrothermal properties, mechanical performance and chemical interactions with mineral pozzolanic binder, Construction and Building Materials 124 (2016) 801-815.

[98] Ahmad M.R., Chen B., Haque M.A., et al., Development of a sustainable and innovant hygrothermal bio-composite featuring the enhanced mechanical properties, Journal of Cleaner Production 229 (2019) 128-143.

[99] Rode C., Peuhkuri R., Time B., et al., Moisture buffer value of building materials. J ASTM Int 4 (5): 100369, 2007.

[100] Rode C., Peuhkuri R.H., Hansen K.K., et al., NORDTEST project on moisture buffer value of materials, AIVC Conference ‘Energy performance regulation': Ventilation in relation to the energy performance of buildings, INIVE eeig, 2005, pp. 47-52.

[101] Ahmad M.R., Chen B., Oderji S.Y., et al., Development of a new bio-composite for building insulation and structural purpose using corn stalk and magnesium phosphate cement, Energy and Buildings 173 (2018) 719-733.

[102] Zuo Y., Xiao J., Wang J., et al., Preparation and characterization of fire retardant straw/magnesium cement composites with an organic-inorganic network structure, Construction and Building Materials 171 (2018) 404-413.

[103] Dušek J., Jerman M., Podlena M., et al., Sustainable composite material based

on surface-modified rape straw and environment-friendly adhesive, Construction and Building Materials 300 (2021) 124036.

[104] Babenko M., Estokova A., Savytskyi M., et al., Study of thermal properties of lightweight Insulation made of flax straw, Slovak Journal of Civil Engineering 26(2) (2018) 9-14.

[105] Laborel-Préneron A., Magniont C., Aubert J.E., Hygrothermal properties of unfired earth bricks: Effect of barley straw, hemp shiv and corn cob addition, Energy and Buildings 178 (2018) 265-278.

[106] Giroudon M., Laborel-Préneron A., Aubert J.-E., et al., Comparison of barley and lavender straws as bioaggregates in earth bricks, Construction and Building Materials 202 (2019) 254-265.

[107] Viel M., Collet F., Lecieux Y., et al., Resistance to mold development assessment of bio-based building materials, Composites Part B: Engineering 158 (2019) 406-418.

[108] Asdrubali F., D'Alessandro F., Schiavoni S., A review of unconventional sustainable building insulation materials, Sustainable Materials and Technologies 4 (2015) 1-17.

[109] D’ Alessandro F., Bianchi F., Baldinelli G., et al., Straw bale constructions: Laboratory, in field and numerical assessment of energy and environmental performance, Journal of Building Engineering 11 (2017) 56-68.

[110] González A.D., Energy and carbon embodied in straw and clay wall blocks produced locally in the Andean Patagonia, Energy and Buildings 70 (2014) 15-22.

[111] Bories C., Vedrenne E., Paulhe-Massol A., et al., Development of porous fired clay bricks with bio-based additives: Study of the environmental impacts by Life Cycle Assessment (LCA), Construction and Building Materials 125 (2016) 1142-1151.

[112] Quintana-Gallardo A., Clausell J.R., Guillén-Guillamón I., et al., Waste valorization of rice straw as a building material in Valencia and its implications for local and global ecosystems, Journal of Cleaner Production 318 (2021) 128507.

[113] Cascone S., Catania F., Gagliano A., et al., Energy performance and environmental and economic assessment of the platform frame system with compressed straw, Energy and Buildings 166 (2018) 83-92.

[114] Zieger V., Lecompte T., de Menibus A.H., Impact of GHGs temporal dynamics

on the GWP assessment of building materials: A case study on bio-based and non-bio-based walls, Building and Environment 185 (2020) 107210.

[115] Rhim J.-W., Physical and mechanical properties of water resistant sodium alginate films, LWT-Food science and technology 37(3) (2004) 323-330.

[116] Viel M., Collet F., Lanos C., Chemical and multi-physical characterization of agro-resources' by-product as a possible raw building material, Industrial Crops and Products 120 (2018) 214-237.

[117] Amziane S., Collet F., Lawrence M., et al., Recommendation of the RILEM TC 236-BBM: characterisation testing of hemp shiv to determine the initial water content, water absorption, dry density, particle size distribution and thermal conductivity, Materials and Structures 50(3) (2017) 1-11.

[118] Hasnain M.S., Jameel E., Mohanta B., et al., Alginates: sources, structure, and properties, Alginates in Drug Delivery, Elsevier2020, pp. 1-17.

[119] Draget K.I., Skjåk-Bræk G., Smidsrød O., Alginate based new materials, International journal of biological macromolecules 21(1-2) (1997) 47-55.

[120] Kumari S., Kishor R., Chitin and chitosan: origin, properties, and applications, Handbook of chitin and chitosan, Elsevier2020, pp. 1-33.

[121] Laborel-Préneron A., Ampe C., Labonne L., et al., Thermal Insulation Blocks Made of Sunflower Pith Particles and Polysaccharide-Based Binders: Influence of Binder Type and Content on Their Characteristics, Construction Technologies and Architecture, Trans Tech Publ, 2022, pp. 43-50.

[122] 1609 E., Thermal insulating products for building applications - Determination of short term water absorption by partial immersion, British Standard, 2013.

[123] Jelle B.P., Traditional, state-of-the-art and future thermal building insulation materials and solutions – Properties, requirements and possibilities, Energy and buildings 43(10) (2011) 2549-2563.

[124] Rahim M., Douzane O., Le A.T., et al., Effect of moisture and temperature on thermal properties of three bio-based materials, Construction and Building Materials 111 (2016) 119-127.

[125] Viel M., Collet F., Lanos C., Development and characterization of thermal insulation materials from renewable resources, Construction and Building Materials

214 (2019) 685-697.

[126] Latif E., Tucker S., Ciupala M.A., et al., Hygric properties of hemp bio-insulations with differing compositions, Construction and Building Materials 66 (2014) 702-711.

[127] Ducoulombier L., Lafhaj Z., Comparative study of hygrothermal properties of five thermal insulation materials, Case studies in thermal engineering 10 (2017) 628-640.

[128] Sing K.S., Reporting physisorption data for gas/solid systems with special reference to the determination of surface area and porosity (Recommendations 1984), Pure and applied chemistry 57(4) (1985) 603-619.

[129] Timmermann E.O., Multilayer sorption parameters: BET or GAB values?, Colloids and Surfaces A: Physicochemical and Engineering Aspects 220(1-3) (2003) 235-260.

[130] Slimani Z., Analyse expérimentale et numérique du comportement hygrothermique de parois fortement hygroscopiques, Lyon 1, 2015.

[131] Slimani Z., Trabelsi A., Virgone J., et al., Study of the hygrothermal behavior of wood fiber insulation subjected to non-isothermal loading, Applied Sciences 9(11) (2019) 2359.

[132] Sarfraz J., Fogde A., Ihalainen P., et al., The performance of inkjet-printed copper acetate based hydrogen sulfide gas sensor on a flexible plastic substrate-varying ink composition and print density, Applied Surface Science 445 (2018) 89-96.

[133] Hamami L., Nassereddine B., Application of wireless sensor networks in the field of irrigation: A review, Computers and Electronics in Agriculture 179 (2020) 105782.

[134] Asan H., Numerical computation of time lags and decrement factors for different building materials, building and environment 41(5) (2006) 615-620.

[135] Rafidiarison H., Mougel E., Nicolas A., Laboratory experiments on hygrothermal behaviour of real-scale timber walls, Maderas. Ciencia y tecnología 14(3) (2012) 389-401.

[136] Xue Y., Fan Y., Wang Z., et al., Facilitator of moisture accumulation in building envelopes and its influences on condensation and mould growth, Energy and Buildings (2022) 112528.

[137] Hou S., Liu F., Wang S., et al., Coupled heat and moisture transfer in hollow concrete block wall filled with compressed straw bricks, Energy and Buildings 135 (2017) 74-84.

[138] Liu X., Chen Y., Ge H., et al., Determination of optimum insulation thickness for building walls with moisture transfer in hot summer and cold winter zone of China, Energy and Buildings 109 (2015) 361-368.

[139] Philip J., De Vries D., Moisture movement in porous materials under temperature gradients, Eos, Transactions American Geophysical Union 38(2) (1957) 222-232.

[140] Luikov A., Application of irreversible thermodynamics methods to investigation of heat and mass transfer, International Journal of Heat and Mass Transfer 9(2) (1966) 139-152.

[141] Whitaker S., Simultaneous Heat, Mass, and Momentum Transfer in Porous Media: A Theory of Drying, 13 (1977) 119-203.

[142] Künzel H.M., Simultaneous heat and moisture transport in building components, One-and two-dimensional calculation using simple parameters. IRB-Verlag Stuttgart 65 (1995).

[143] Mendes N., Ridley I., Lamberts R., et al., UMIDUS: a PC program for the prediction of heat and moisture transfer in porous building elements, Building Simulation Conference‐IBPSA, 1999, pp. 277-283.

[144] Trabelsi A., Slimani Z., Virgone J., Response surface analysis of the dimensionless heat and mass transfer parameters of medium density fiberboard, International Journal of Heat and Mass Transfer 127 (2018) 623-630.

[145] Promis G., Freitas Dutra L., Douzane O., et al., Temperature-dependent sorption models for mass transfer throughout bio-based building materials, Construction and Building Materials 197 (2019) 513-525.

[146] 15026 E.I., Hygrothermal performance of building components and building elements - Assessment of moisture transfer by numerical simulation, British Standard, 2007.

[147] Abbas M.S., McGregor F., Fabbri A., et al., Effect of moisture content on hygrothermal properties: Comparison between pith and hemp shiv composites and other construction materials, Construction and Building Materials 340 (2022) 127731.

[148] Lu J., Wang K., Qu M.-L., Experimental determination on the capillary water absorption coefficient of porous building materials: A comparison between the intermittent and continuous absorption tests, Journal of Building Engineering 28 (2020) 101091.

[149] Trabelsi A., Hamami A., Belarbi R., et al., Assessment of the variability of moisture transfer properties of High Performance Concrete from a multi-stage drying experiment, European journal of environmental and civil engineering 16(3-4) (2012) 352-361.

[150] Prithiviraajan R., Somasundharam S., Reddy K., Development of experimental methodology for estimation of thermo-physical properties of engineering materials using inverse method, Thermal Science and Engineering Progress 22 (2021) 100832.

[151] Vereecken E., Roels S., Janssen H., Inverse hygric property determination based on dynamic measurements and swarm-intelligence optimisers, Building and Environment 131 (2018) 184-196.

[152] Eberhart R., Kennedy J., A new optimizer using particle swarm theory, Micro Mach, Hum. Sci (1995).

[153] Whitley D., A genetic algorithm tutorial, Statistics and computing 4(2) (1994) 65-85.

[154] Chai T., Draxler R.R., Root mean square error (RMSE) or mean absolute error (MAE), Geoscientific Model Development Discussions 7(1) (2014) 1525-1534.